THE EFFECT OF STRAIN RATE ON THE DEFORMATION BEHAVIOR OF ADDITIVELY MANUFACTURED SHORT CARBON FIBER REINFORCED POLYAMIDE COMPOSITES

A Thesis Submitted to
the Graduate School of Engineering and Sciences of
İzmir Institute of Technology
in Partial Fulfillment of the Requirements for the Degree of

MASTER OF SCIENCE

in Mechanical Engineering

by
Mehmet Kaan ZEYBEK

July 2022

İZMİR

ACKNOWLEDGMENTS

I would like to express my gratitude to my thesis advisor Prof. Dr. Mustafa GÜDEN for his guidance, inspiration, patience and encouragement during my thesis study.

I would like to state my thankfulness to Roketsan for allowing me to use the 3D printer to produce test samples.

Additionally, I am grateful to Mesut BAYHAN, Mustafa Kemal SARIKAYA and Samed ENSER for their support and assistance during the experimental study in Dynamic Testing and Modeling Laboratory.

Furthermore, I want to express my gratitude to my father Volkan ZEYBEK, and my mother Nihal ZEYBEK for their emotional support and encouragement during the completion of my thesis.

ABSTRACT

THE EFFECT OF STRAIN RATE ON THE DEFORMATION BEHAVIOR OF ADDITIVELY MANUFACTURED SHORT CARBON FIBER REINFORCED POLYAMIDE COMPOSITES

The compression behavior of Polyamide 6 (PA6- nylon 6) and short carbon fiber reinforced polyamide 6 (Onyx) produced by the Fused Deposition Modelling (FDM) method was investigated at both quasi-static and dynamic strain rates. The effects of layer height, specimen shape and dimensions, build direction and the orientation of the layers on the compression behavior were also determined. The results showed that the addition of short carbon fibers to the PA6 matrix increased the compression strength by 3-4 times and the determined flow stress has a strong correlation with the porosity amount in the specimens. The compression test results showed that cylindrical specimens had slightly higher flow stress than the cubic specimens. The compression tests on the specimens produced with different lengths showed almost no difference regarding stress-strain behavior. Furthermore, the specimens produced with 90 degrees showed the highest elastic modulus and yield strength and the specimens produced with 30 and 60 degrees the lowest modulus and yield strength. The Concentric infill specimens exhibited higher elastic modulus values and flow stresses than Cross raster infill specimens at all strain rates. In the layers of concentric rings, the outer rings prevented the lateral expansion of inner rings, leading to higher flow stresses than the cross raster [0/90] lay-up. The flow stress of both PA6 and Onyx specimens increased with increasing strain rate. The rate sensitivities of PA6 and Onyx specimens were shown to be similar to each other.

ÖZET

GERİNME HIZININ EKLEMELİ İMALAT YÖNTEMİ İLE ÜRETİLEN KISA KARBON FİBER TAKVİYELİ POLYAMİD KOMPOZİTLERİN DEFORMASYON DAVRANIŞINA ETKİSİ

Eklemeli imalat yöntemlerinden biri olan Eriyik Biriktirmeli Modelleme yöntemi ile üretilen Poliamit 6 (PA6 – naylon 6) ve kısa karbon fiber takviyeli poliamit 6' nın (Onyx) basma davranışı hem yarı statik hem de dinamik gerinim hızlarında incelenmiştir. Katman yüksekliği, numunenin şekli ve boyutları, basım yönü ve katmanların basım yapısının basma davranışı üzerindeki etkileri de incelenmiştir. Sonuçlar, PA6 matrisine kısa karbon fiberlerin eklenmesinin basma mukavemetini 3-4 kat arttırdığını ve belirlenen akma gerilmesinin numunelerdeki boşluk miktarı ile güçlü bir korelasyona sahip olduğunu göstermiştir. Basma testi sonuçları, silindirik numunelerin küp numunelere göre biraz daha yüksek akış gerilmelerine sahip olduğunu göstermiştir. Farklı uzunluklarda üretilen numuneler üzerinde yapılan basma testleri, gerilme-şekil değiştirme davranışında nerdeyse hiçbir farklılık göstermemiştir. Ayrıca 90 derece basım açısına sahip numuneler en yüksek elastik modülü ve akma mukavemetini, 30 ve 60 derece basım açısına sahip numuneler ise en düşük modül ve akma mukavemetini göstermiştir. İç yapısının konsantrik olduğu numuneler tüm gerinim hızlarında iç yapısı çapraz [0/90] örülmüş numunelere göre daha yüksek elastik modül değerleri ve akış gerilmeleri sergilemiştir. Her bir katmandaki eş merkezli halkalar, dış halkaların iç halkaların yanal genişlemesini önlemesinden dolayı çapraz [0/90] örülmüşe göre daha yüksek mukavemetli olmasına yol açmıştır. Hem PA6 hem de Onyx numunelerin akış gerilmesi değerleri artan gerinim hızı ile artmıştır. PA6 ve Onyx numunelerinin gerinim hızı duyarlılıklarının birbirine yakın olduğu görülmüştür.

TABLE OF CONTENTS

LIST OF FIGURES

Figure **Page**

Figure **Page**

Figure **Page**

Figure **Page**

Figure **Page**

LIST OF TABLES

Table **Page**

CHAPTER 1

INTRODUCTION

Composites are simply obtained by combining two or more different materials. The combination usually ends up with an overall property better than the individual properties of the components. In a composite, a continuous phase, called the matrix, holds the strong reinforcing phase, and the reinforcement is usually a strong material in the form of long or short fiber. Composite manufacturing creates strong and durable products with high strength-to-weight and stiffness-to-weight ratios. The 3D printing technology that was originally developed for prototyping and later adapted as a production method has also been used in composite manufacturing over the last several years. Broadly, 3D printing is defined as a method of building three-dimensional physical parts layer by layer by means of a digital file of the structure. 3D printing or additive manufacturing (AM) is becoming increasingly popular nowadays; its use is extended to a wide range of sectors including architectural design, aerospace and automotive engineering, biomedical, dentistry, and jewelry creation. Note that AM eliminates the constraints imposed by the traditional production methods such as machining, extrusion, rolling, forging and casting. Its fast-prototyping ability can be used to produce parts that are not cost-effective or practical by the use of conventional methods. Furthermore, AM reduces significantly the waste material as compared with the production by machining.

It is easier to produce composite parts using AM than conventional methods, for example, hand lay-up, RTM and filament winding. AM is adjustable; that is only the critical regions can be reinforced selectively. Furthermore, it eliminates the problems of conventional composite processing such as low matrix area. The easier production, repeatability, and recyclable properties ensure the application of the additively manufactured composites which mostly consist of a thermoplastic matrix and a short fiber reinforcement. The use of thermoplastics especially with short fiber reinforcements has increased mostly in the automotive industry. The plastic parts in the past were mostly used in the non-load carrying applications, while the application has been extended to the structural components with the recent developments in the area of short fiber reinforcements. There are however challenges to be overcome with the short fiber

composite manufacturing by AM. Manufacturing a thermoplastic material by AM results in anisotropy in the mechanical properties because of the deposition nature of layer by layer. Inclusions of short fibers as reinforcement further increase the anisotropy depending on the fiber volume fraction and fiber orientation.

The subject of the present thesis study is the determination of the mechanical properties of an FDM short carbon fiber reinforced Polyamide 6 (Nylon 6) composite at different strain rates. Through quasi-static and high strain rates, the strain rate sensitivity of the additively manufactured carbon fiber reinforced nylon was determined at varying layer thicknesses and layer orientations.

CHAPTER 2

LITERATURE REVIEW

2.1. Additive Manufacturing

Additive manufacturing is considered a novel technology that has the potential to make a significant impact on the world. The applications of additive manufacturing range from dentistry to construction, shipbuilding or aerospace industry (Ziółkowski and Dyl 2020),(R. Kumar, Kumar, and Chohan 2021),(Javaid and Haleem 2019),(Tuomi et al. 2014),(Horn and Harrysson 2012),(Camacho et al. 2017),(Attaran 2017). The procedure involves printing several layers of materials on top of one another, opposite to the conventional manufacturing which is based on formative or subtractive methods, as depicted in Figure 2.1 (Lang et al. 2019). The first additive manufacturing machine was developed by Charles "Chuck" Hull in 1986 using the Stereolithography and the so-called fused deposition modeling (FDM) method which uses a thermoplastic filament was developed later in 1988 by Scott Crump (Matias and Rao 2015). AM methods such as powder bed fusion, inkjet printing, and contour crafting (CC) (Ngo et al. 2018) were also developed sequentially.

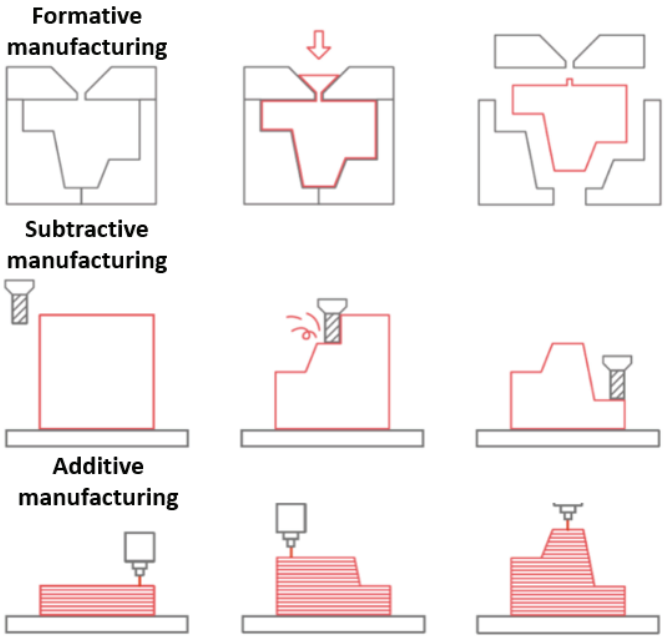

Figure 2.1. Manufacturing methods
(Source: Lang et al., 2019)

In the manufacturing industry, AM is frequently compared with the Computer Numerical Control (CNC) technique. The CNC produces desired geometries by subtracting a bulk starting material by using special tools and cutters until the desired geometry is obtained. This machining process causes the production of a high amount of waste material. On the other side, AM generates substantially less waste material as it builds the parts by deposition rather than subtracting. Another important advantage of AM is the opportunity to simplify the supply chain and to solve the current problems of supply chain management. AM will allow production lines in small batches, which allow companies to adapt quickly to changes in demand and offer custom products much more easily. AM has also a smaller environmental footprint due to less waste material generation and reduced logistic needs and hence lower fuel consumption. AM has also the capability of adjusting the infill percentage by using different sizes and geometries of cell or lattice structures (Figure 2.2). Changing the infill percentage and using cellular structures inside the geometry led to the production of lighter parts. This ability is a big advantage over traditional manufacturing methods because it is nearly impossible or very time-consuming and costly for obtaining such products by using traditional methods. Such ability ensures the parts produced by AM methods have better performance with a high strength-to-weight ratio, excellent energy absorption and also with minimum material requirements (Nazir et al. 2019).

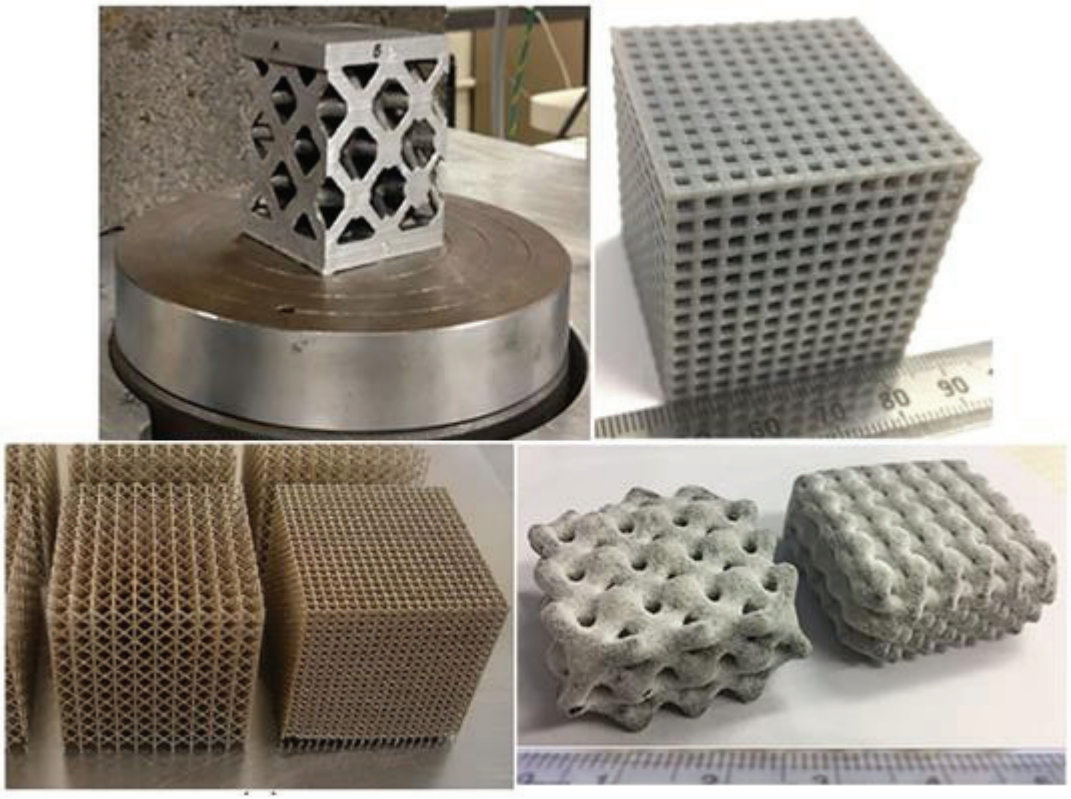

Figure 2.2. Examples of cellular lattice structures produced by AM
(Source: Nazir et al., 2019)

Although, AM has some superior advantages over traditional manufacturing, the size restriction, production time and cost are disadvantages with present technology. The AM machines are not big compared to traditional methods so the produced part sizes are limited. Therefore, AM is considered currently not a suitable method for mass production (Attaran 2017). Considering cost analysis for big production quantities the traditional methods are more suitable than additive manufacturing but additive manufacturing is more suited to higher levels of complexity or customization (Pereira, Kennedy, and Potgieter 2019).

AM processes can be categorized in several ways. One way is to summarize AM by the used method of layer forming as shown in Table 2.1 (Bikas, Stavropoulos, and Chryssolouris 2016). Laser based methods use a laser source to shape AM part. These methods include for example the selective laser sintering (SLS) and selective laser melting (SLM) as seen in Table 2.1 SLS and SLM are further grouped as a powder bed method as the powders are melted under laser spot. AM based on extrusion include FDM and robocasting. Jetting methods include ceramic and polymer (3DP) jetting. Finally, electron beam melting (EBM) uses an electron beam to melt a powder bed (Bikas, Stavropoulos, and Chryssolouris 2016).

Table 2.1. Categorization of additive manufacturing processes
(Source: Bikas et al., 2016)

Additive Manufacturing (AM) Processes													
Process	Laser Based AM Processes						Extrusion Thermal		Material Jetting		Material Adhesion		Electron Beam	
	Laser Melting				*Laser Polymerization*									
Process Schematic	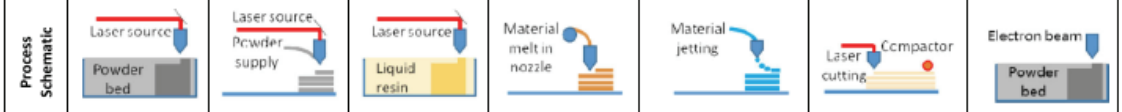													
Name / Material	SLS		DMD		SLA		FDM		3DP		LOM		EBM	
	SLM		LENS		SGC		Robocasting		IJP		SFP			
	DMLS		SLC		LTP				MJM					
			LPD		BIS				BPM					
					HIS				Thermojet					
Bulk Material Type	Powder				Liquid		Solid							

2.2. Fused Deposition Modelling (FDM)

The FDM is the most common form of 3D printing and one of the oldest methods of 3D printing. Main steps of manufacturing parts by using the FDM technique from design to product are shown in Figure 2.3 (Shanmugam et al. 2021). After the product is designed in the computer by using CAD software, it is converted to STL file format. Later, the 3D printer's production steps are adjusted by slicing a geometry into layers with slicing software. Then, the printer starts to build the desired part.

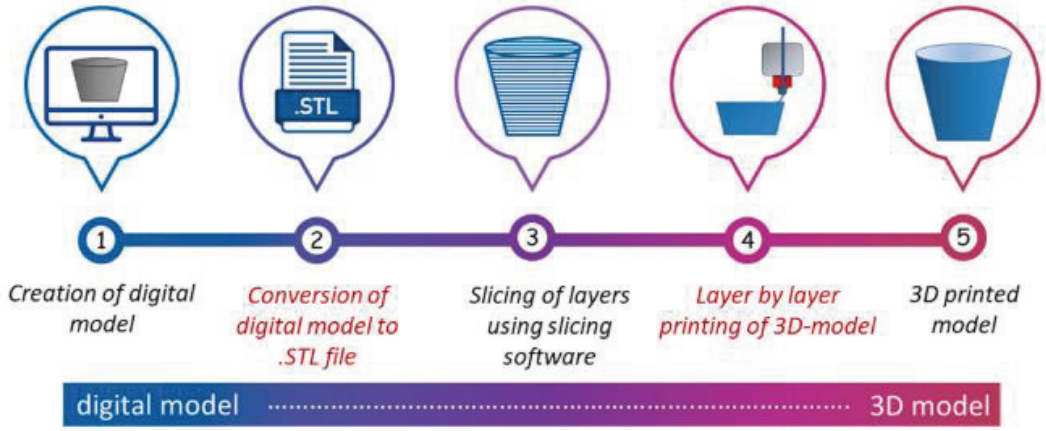

Figure 2.3. Main steps of FDM 3D printing
(Source: Shanmugam et al., 2020)

In FDM, a computer-controlled extrusion head moves along 1 (X), 2 (Y), and 3 (Z) axes while laying down thin layers of material on top of each other in order to build up a model or part as shown schematically in Figure 2.4 (DePaul, Ghebretinsae, and DerKlift 2017). The temperature and the rate of the flow of filament are controlled. This allows the creation of complex shapes with smoother surfaces. The raw material is called filament which is wounded on spools. The filament enters a guiding tube and the exit of the tube is connected to a nozzle. Before entering the nozzle, there is a small electric motor element that pushes the filament at a constant speed through the nozzle. When the filament is pushed through the nozzle, the nozzle temperature increases to melt the filament and allow the filament to flow through the nozzle's desired diameter. After the melted filament flows from the nozzle it bonds on the printing bed. The nozzle movement is provided by small electric motors that move only in the X and Y direction. After the first layer of desired geometry is produced, the print bed moves downward which is the Z direction and the second layer starts production. This operation follows the same consecutive steps.

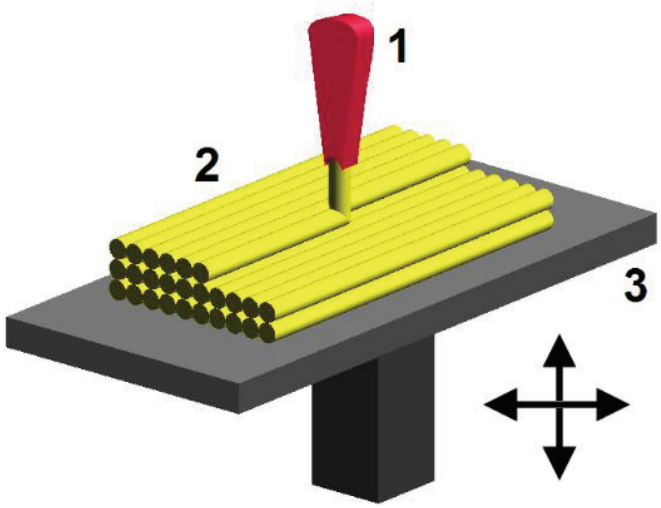

Figure 2.4. Schematic of FDM 3D printing
(Source: DePaul et al., 2017)

Table 2.2 summarizes the type of materials used, applications, advantages and drawbacks of widely used AM methods of FDM, powder bed fusion (SLS, SLM) and ceramic and polymers (3DP)), inkjet printing and contour crafting, stereolithography, direct energy deposition and laminated object manufacturing (Ngo et al. 2018). The main advantages of FDM over other AM methods include the low cost, high speed and simplicity, while weak mechanical properties obtained and limitation with the use of

thermoplastics materials are the main disadvantages. Note that the parts produced by FDM method have anisotropic properties. As the part is produced by stacking consecutive layers, the tensile strength in the Z direction, which is the construction direction, is the lowest (Ahn et al. 2002). Both neat and short fiber contained thermoplastic filaments are in FDM process, including acrylonitrile butadiene styrene (ABS), polylactic acid (PLA), polypropylene (PP), polyether-ether-ketone (PEEK) and polyamides (PA) (Wu et al. 2020a).

Table 2.2. The comparison of different additive manufacturing methods (Source: Ngo et al., 2018)

Methods	Materials	Applications	Benefits	Drawbacks
Fused Deposition Modelling (FDM)	Continues filaments of thermoplastic polymers and fiber reinforcements	Rapid prototyping, Toys, Composite parts	Low cost, High speed, Simplicity	Weak mechanical properties, Limited material, Layer by layer
Powder Bed Fushion (SLS, SLM, 3DP)	Compacted fine powders metals, alloys and limited polymers (SLS, SLM), Ceramic, concrete and soil	Biomedical, Electronics, Aerospace, Lightweight structures (lattice), Heat exchangers	Fine resolution, High quality	Slow printing, Expensive, High porosity in the binder method (3DP)
Inkjet printing and contour crafting	A concentrated dispersion of particles in a liquid, Ceramic, concrete and soil	Biomedical, Large structures, Building	Ability to print large structures, Quick printing	Lack of adhesion between layers, Layer by layer finish
Stereolithography	A resin with photo-active monomers, Hybrid polymer-ceramics	Biomedical, Prototyping	Fine resolution, High quality	Very limited materials, Slow printing, Expensive
Direct Energy Deposition	Metals and alloys in the form of powder or wire, Ceramics and polymers	Aerospace, Retrofitting, Repair, Cladding, Biomedical	Reduced manufacturing time and cost, Excellent mechanical properties, Controlled microstructure	Low accuracy, Low surface quality

2.3. Properties of Polymers

Polymers consist of large C-based molecular chains made up of repeating structural units called monomers. In a composite, a polymer as a matrix surrounds the reinforcement and protects it from the environment. There are two types of polymers: thermoplastic and thermoset (Figure 2.5). The thermoset polymers (e.g. Polyester, Phenolic resins, Epoxy, etc.) have chemically bonded molecular chains which cannot be

reshaped and recycled (Nik Hanyn et al. 2017). These chemically bonded polymer chains are formed as a result of the monomers bonding each other as a cross-link during the curing process (Karuppiah 2016). Due to the cross-linked molecular structure, thermosets are generally stiffer and stronger than thermoplastics (Bazzi and Angelou 2018). On the other hand, thermoplastic polymers (e.g. Polypropylene, Polyvinylchloride, Polyethylene, etc.) have chained or branched-chain molecules which are not cross-linked. The intermolecular bonding between the chains in a thermoplastic is therefore only weak intermolecular interactions, such as Van der Waals or hydrogen bonds. This enables thermoplastics to be recyclable and reshaped by heat. These distinctions between thermoplastics and thermosets have an impact on specific application areas. For example, thermoplastics are ideal for high-volume applications and consumer products due to their low melting point, ease of manufacture, and recyclability, whereas thermosets are resistant to high temperatures without losing their shape and are stronger and stiffer, making them ideal for high-temperature applications and structural components.

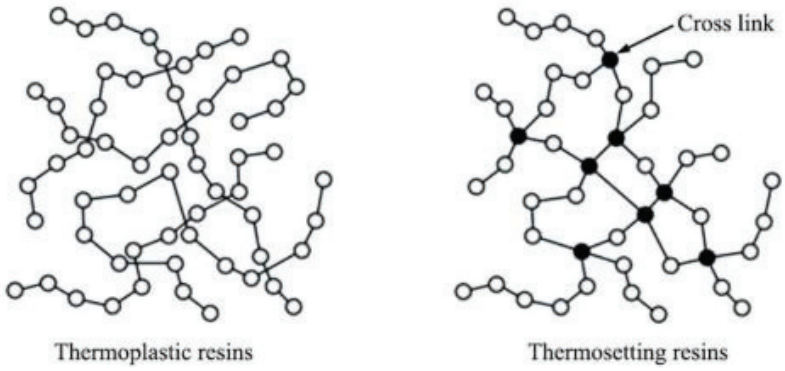

Figure 2.5. Molecular structure of thermoplastics and thermosets
(Source: Karuppiah et al., 2016)

On the basis of their degree of organized microstructure, thermoplastics are classified as amorphous or semi-crystalline (Figure 2.6). In an amorphous polymer, the molecular chains are randomly distributed. Semi-crystalline thermoplastics have a microstructure composed of tiny areas with an ordered structure. In these polymers, the molecular chains are partially randomly distributed and partially oriented in one direction. Semi-crystalline polymers are more prone to heat shrinkage and warpage than amorphous polymers. This is because the arrangement of long polymer chains causes microstructural changes in a semi-crystalline polymer during crystallization. Amorphous thermoplastics are however more brittle and stiffer than semi-crystalline thermoplastics (Appelsved

2012). Therefore, manufacturing a product by using FDM with amorphous thermoplastic, the dimensions of the product are more stable. Although semi-crystalline thermoplastics are more prone to shrinkage and warpage, their mechanical properties in a high-temperature environment and better chemical and wear-resistant properties attract interest and make them preferable (Antony Samy et al. 2021). In Figure 2.7 the most popular thermoplastics in AM are represented as a thermoplastic pyramid (Auerbach n.d.). Thermoplastics are especially advantageous for structural aerospace applications since they are lightweight, strong, have a long service life, able to be reinforced with fibers, and are frequently more mechanically robust than alternatives (Kreider et al. 2021).

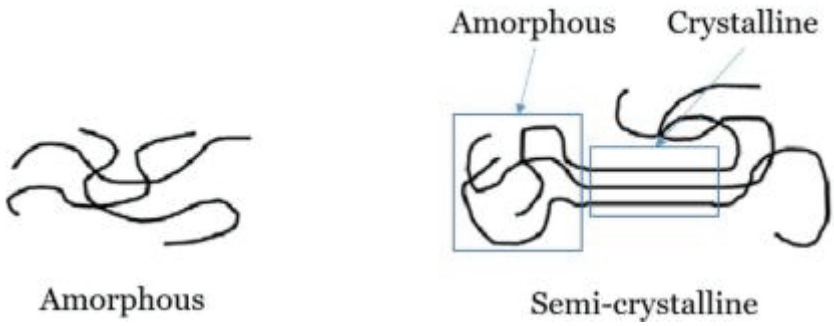

Figure 2.6. Amorphous and Semi-crystalline structures of thermoplastics (Source: Bazzi et al., 2018)

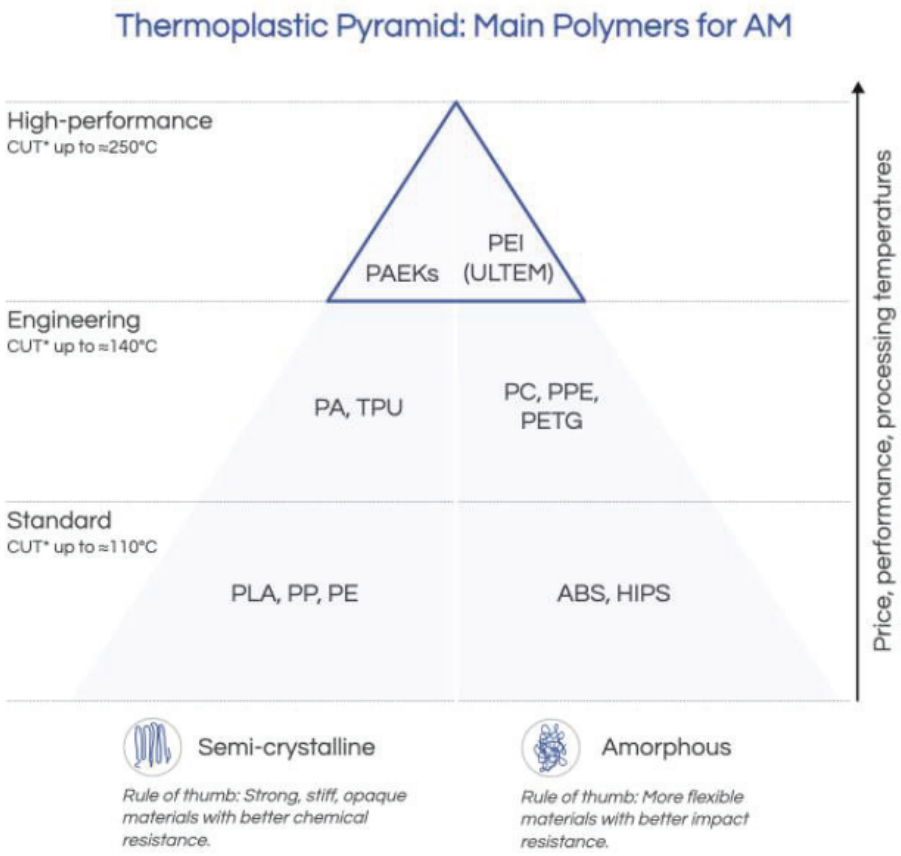

Figure 2.7. The thermoplastic materials pyramid representation categorising with print temperature (Source: https://www.aniwaa.com/insight/am-materials/am-thermoplastics-semi-crystalline-vs-amorphous/)

2.4. Processing of Polymer Materials Using FDM

Typically, the Fused Filament Fabrication (FFF) method involves pressurizing and melting a thermoplastic filament into a liquid and then depositing it on a construction platform using a nozzle. The mechanical properties of FDM printed parts are usually lower than those of the conventionally manufactured polymers. The main reasons for the lower mechanical performances are the existence of the pores and weak interlayer bonding between the deposited layers and rough surface finishing (Krajangsawasdi et al. 2021). The most popular polymers used in FDM manufacturing are listed in Figure 2.8 (Fico et al. 2022). Blok et. al. classified the common thermoplastic polymers used in the FDM and compared them in different scopes such as mechanical properties, density, thermal properties, shrinkage, etc. and showed that the ABS has the highest score among

other thermoplastics (Figure 2.9) (Blok, Longana, and Woods 2020). Table 2.3 further shows a comparison of common thermoplastics and their properties for suitability in the FDM to obtain optimum products. In the same table, green, orange and red colors refer to good, medium and poor properties, respectively. The suitable parameters for 3D printing include low processing temperature, high specific heat capacity, high thermal conductivity, low coefficient of thermal expansion, being in the amorphous state, low processing temperature, low shrinkage and they have categorized and scored the materials to find which one is more suitable for carbon fiber reinforced FFF (Blok, Longana, and Woods 2020). Polyamide is classified as a medium level among the other well-known 3D printing materials, according to the results of the evaluation based on these factors, as shown in Figure 2.9.

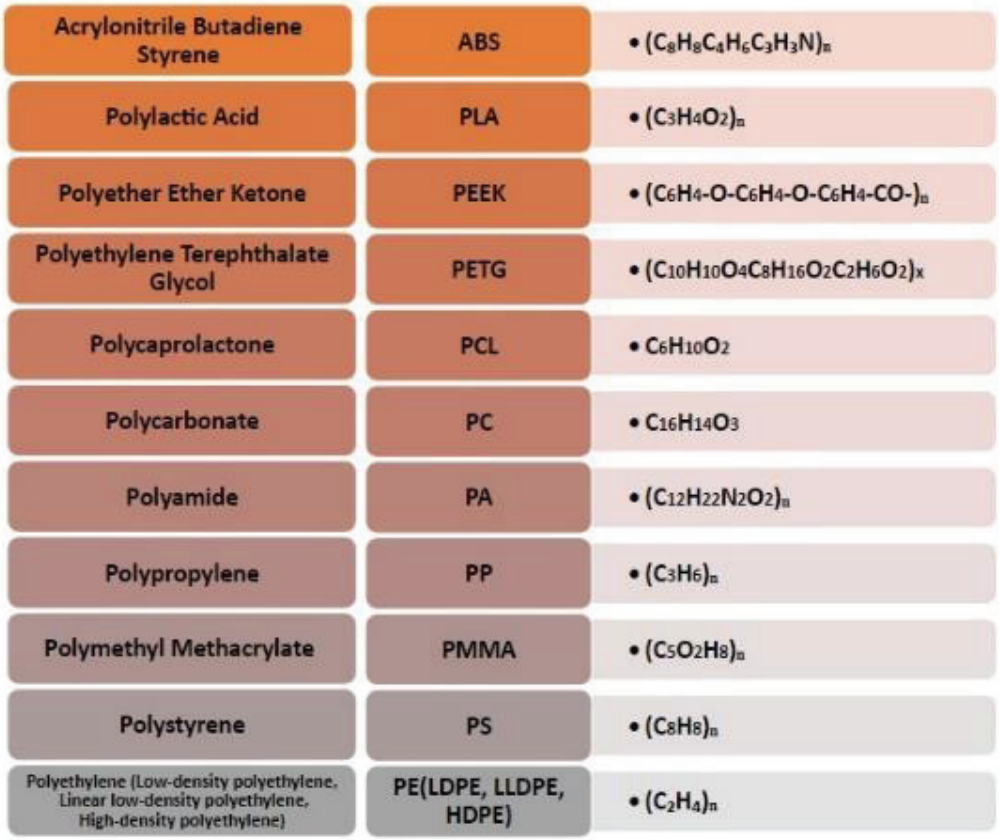

Figure 2.8. The most popular polymers used in FDM industry
(Source: Fico et al., 2022)

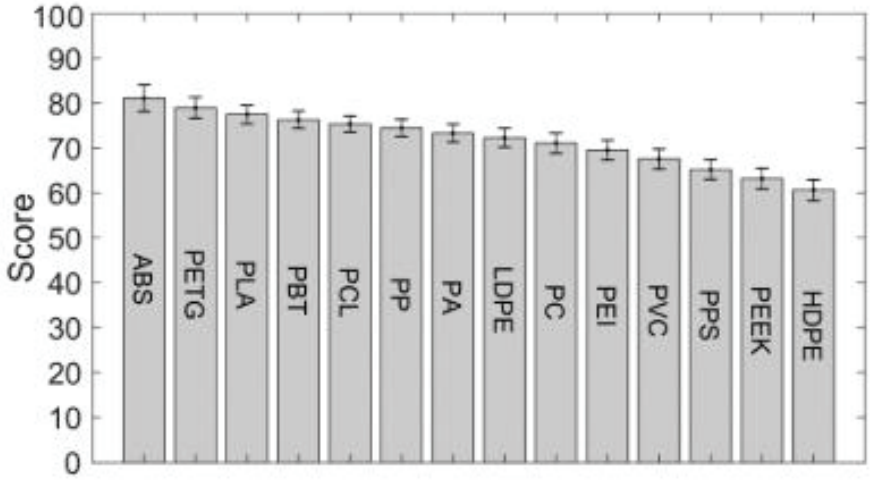

Figure 2.9. The average ranking of common polymers with respect to printing capabilities (Source: Blok et al., 2020)

Table 2.3. Comparison of common thermoplastics and properties for suitability on FDM (Source: Blok et al., 2020)

	PA	PLA	ABS	PETG	HDPE	PEEK
	Polyamide (Nylon)	*Poly Lactic Acid*	*Acrylonitrile Butadiene Styrene*	*Polyethylene Terephthalate Glycol*	*High Density Poly Ethylene*	*Poly Ether Ether Ketone*
Strenght (GPa)	0.94-1.18	2.3-2.6	2-2.9	2.01-2.11	1.07-1.09	3.79-3.95
Stiffness (MPa)	38.6-48.2	38-68	29.6-44.1	47.9-52.9	26.2-31	87-95
Density (kg/m^3)	1060-1080	1110-1210	1020-1080	1260-1280	952-965	1300-1320
Glass Transition Temperature (°C)	60	52-82.6	88-120	81-91	-125, -90	143-157
Processing Temperature (°C)	220-327	170-210	177-260	249-288	177-274	349-399
Coefficient of Thermal Expansion (CTE) (µstrain/°C)	141-147	126-145	128-234	120-123	106-198	50-60
Thermal Conductivity (W/m°C)	0.24-0.32	0.13-0.16	0.266-0.235	0.257-0.267	0.461-0.502	0.24-0.26
Specific Heat Capacity (J/kg°C)	1.65e3-1.71e3	1.18e3-1.21e3	1.39e3-1.41e3	1.47e3-1.53e3	1.75e3-1.81e3	1.34e3
Crystallinity	Semi-crystalline	Semi-crystalline	Amorphous	Amorphous	High Level Of Crystallinity	Semi-crystalline
Shrinkage (%)	1.2-1.8	0.3-0.4	0.4-0.7	0.2-0.5	1.5-4	1-1.21
Interfacial Properties w Carbon Fibre	IFSS of 19.3 MPa	IFSS of 11-19 Mpa	Less than PA	Less than PA	*	IFFS around 80 MPa

Manufacturing parts using the FDM technique results in a product with quite different mechanical characteristics. The differences arise from the manufacturing method itself and printing parameters. Shanmugam et. al. (Shanmugam et al. 2021) investigated the FDM process parameters, Figure 2.10 (a), and the parameters affecting the quality of the parts, Figure 2.10(b). In order to achieve optimum layer bonding adhesion between the layers, these parameters should be adjusted carefully. The bonding between adjacent layers via intermolecular polymer chain entanglement must be created for high strength. The voids inside the parts form between the layers because of the low contact area of the layers. Increasing the bonding of layers decreases the voids inside the parts and leads to more uniform and less anisotropic structure. The representative images of voids between layers are shown in Figure 2.11. The viscosity, thermal conductivity, heat capacity and cooling rate affect the bonding between layers (Wu et al. 2020b). The interlayer bonding mechanism as neck formation between adjacent layers is shown in Figure 2.11 (Li et al. 2022). Improved bonding between layers can be achieved by increasing the temperature up to a limit and increasing the temperature above this limit leads to the degradation of polymer, resulting in poor surface quality and dimensional inaccuracy (Shanmugam et al. 2021)(Ding et al. 2020)(N. Kumar et al. 2018). According to Peng et. al. increasing the build plate temperature ensures the better bonding between adjacent layers as shown in Figure 2.12 and the interlayer strength increases 2 times as the build plate temperature increases (X. Peng et al. 2020).

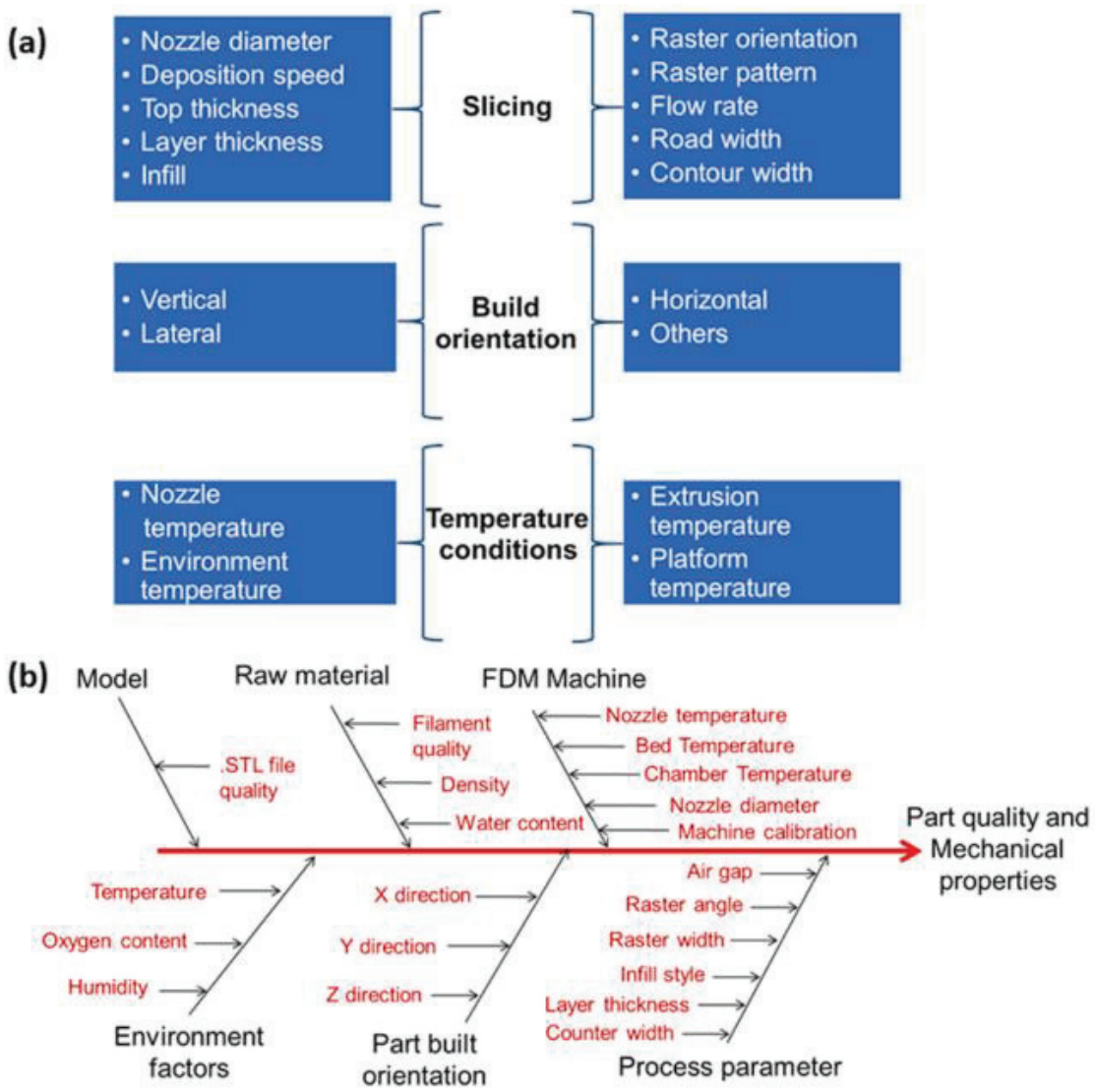

Figure 2.10. (a) The process parameters of FDM technique (b) Effecting parameters of part performance and quality (Source: Shanmugam et al., 2020)

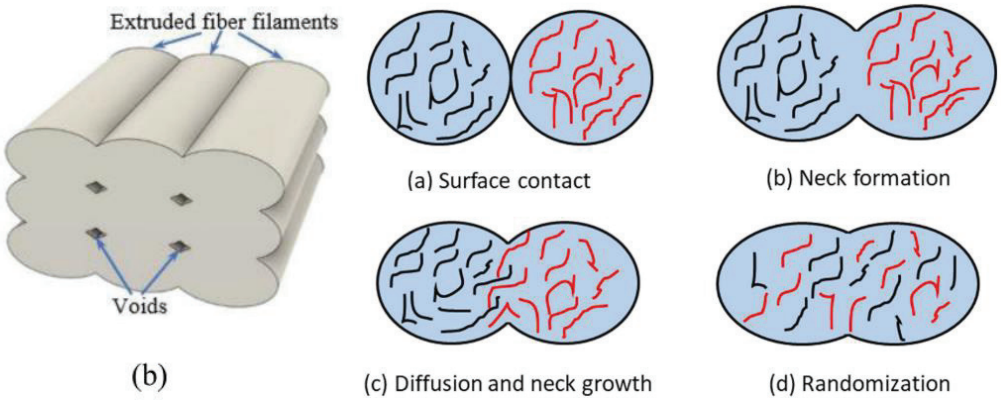

Figure 2.11. Voids inside the FDM-printed part (Source: Li et al., 2022) and bonding formation of layers (Source: Shanmugam et al., 2020)

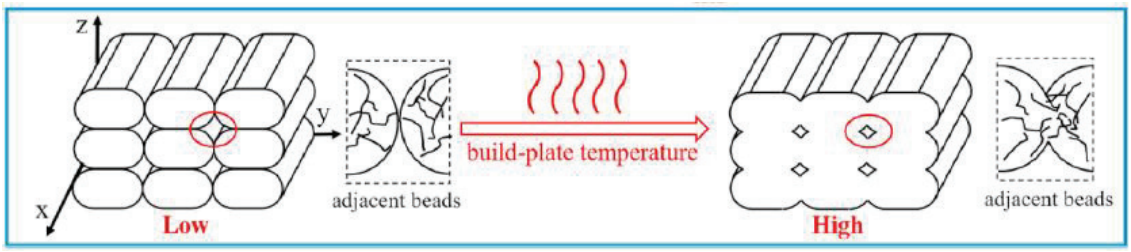

Figure 2.12. Temperature effect on interlayer bonding
(Source: Peng et al., 2020)

2.5. Processing Polyamide (Nylon) Material with FDM

FDM technique mostly uses thermoplastics as raw materials for part production. Despite the availability of various types of thermoplastic, their low mechanical performances and costs limit their use in the FDM. The research is still continuing on obtaining high performance and stable thermoplastics for the FDM applications. Polyamide (PA) is known as Nylon and is classified as engineering thermoplastic. The interest in using PA in the FDM is due to its mechanical properties, improved workability, and low cost (Kreider et al. 2021),(Krajangsawasdi et al. 2021). The most widely used Polyamides are Polycaprolactam (Nylon 6) and poly(hexamethylene adipamide) (Nylon 6,6). Both have high ductility, tensile strength and toughness, moderate resilience and high creep resistance. Additionally, they are capable of working at elevated temperatures as they have high glass transition and melting temperatures (Nik Hanyn et al. 2017). However, there are also significant drawbacks of using PA in FDM applications. Polyamides absorb the moisture from the environment and the moisture causes a decrease in the mechanical properties of more than 50% (Nik Hanyn et al. 2017). Because the intermolecular hydrogen bonds between amide chains are disrupted and replaced by water bridges, the entanglement and bonding between the molecule chains are reduced, resulting in lower stiffness and strength (Appelsved 2012). Another drawback of PA is warpage and shrinkage. The crystallization generates shrinkage stress and after each layer is printed on the previous one, the shrinkage increases. The parts manufactured from PA by using FDM have therefore improper and unstable dimensions due to warpage (Zhang, Fan, and Liu 2020).

There are several sources on the internet about the performances of 3D printing materials in the FDM process. One of them summarizes and categorizes the thermoplastic polymers based on printability, visual quality, strength, elongation at break, impact resistance, layer adhesion, and heat resistance (3d Matter n.d.). The comparison was made between six distinct 3D printing materials: PLA, ABS, poly(ethylene terephthalate) (PET), nylon 6, thermoplastic polyurethane TPU, (rubber-like substance), and PC. The main purpose was to help the FDM users in selecting the best material for their needs. The results are shown in Figure 2.13(a) and (b). According to this comparison, Nylon 6 has moderate properties regarding printability and mechanical performance but has a lower performance regarding layer adhesion and heat resistance than other materials. Krajangsawasdi et. al. reviewed the mechanical properties of the FDM printed thermoplastic polymers. Again, the results showed that Nylon has a moderate tensile strength (Figure 2.14(a)) and tensile stiffness (Figure 2.14 (b)) (Krajangsawasdi et al. 2021).

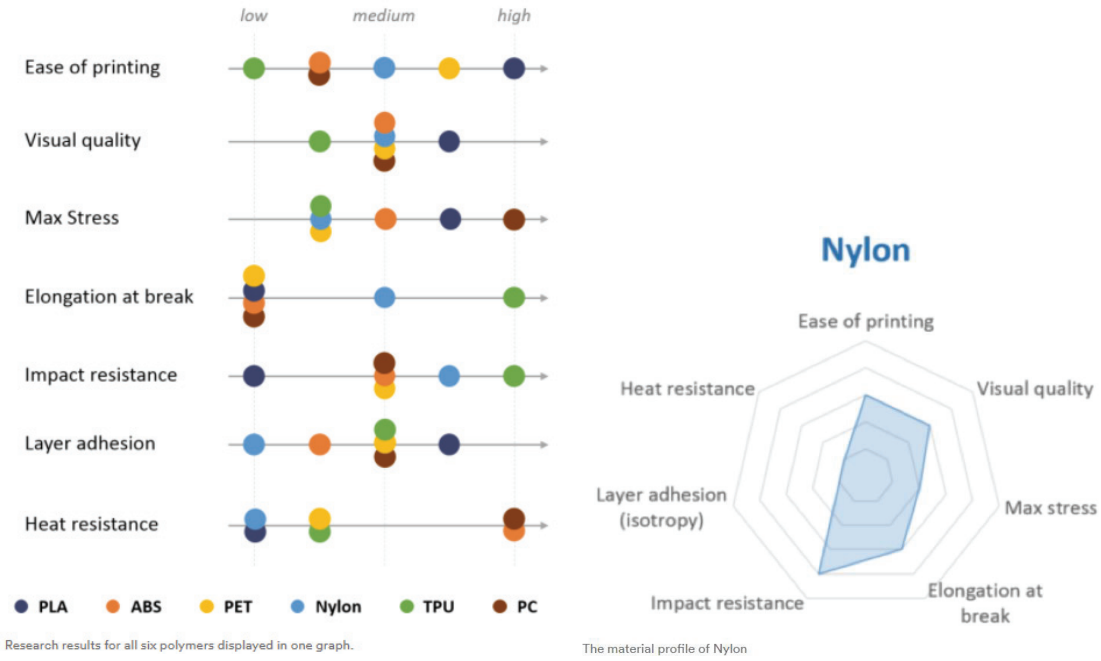

Figure 2.13. (a) The place of Nylon among common thermoplastics, (b) The spider-web graph of Nylon (Source:https://www.hubs.com/knowledge-base/fdm-3d-printing-materials-compared)

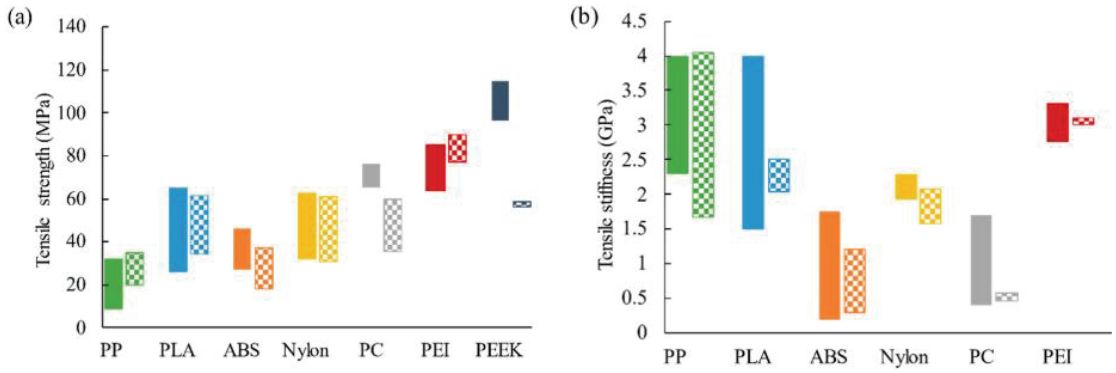

Figure 2.14. The comparison of common thermoplastics considering tensile properties (Source: Krajangsawasdi et al., 2021)

2.6. Reinforcement of Thermoplastics in FDM

The majority of 3D printed polymer parts are still prototypes as the layer by layer production reduces the mechanical properties and the pure polymer products are lacking the strength and functionality required for fully functional and load-bearing components (Araya-Calvo et al. 2018a). By implementing reinforcements such as particles, fibers, or nanomaterials into thermoplastic polymers, the mechanical properties of 3D printing of polymers may be enhanced and make it possible to fabricate parts with high performance and functionality (Caminero et al. 2018)(Jiang and Smith 2017). The tensile properties of different thermoplastics with carbon fiber reinforcement were investigated by Jiang et. al. and it was shown that the addition of carbon fiber increased the strength and stiffness but decreased the ductility (Jiang and Smith 2017). In order to reinforce the thermoplastic 3D printed material, the reinforcement material processability and performance should be considered. When the fiber size increases, from whiskers to continuous fibers, the performance increases but the processability decreases as shown in Figure 2.15. A trade-off between performance and processability is therefore needed. A 6.3 fold improvement in the tensile strength and a 5 fold improvement in the flexural strength was reported for the continuous carbon, glass and kevlar fiber reinforcements in the Nylon matrix (Dickson et al. 2017). The FDM continuous fiber reinforced polymers had also higher tensile strength than aerospace-grade aluminum (Dickson et al. 2017). Figure 2.16 shows the effect of different types of fiber reinforcements on the tensile strength of different thermoplastic matrices. In each thermoplastic, the continuous carbon fiber reinforcement

increases the tensile strength. The short carbon fiber reinforced Nylon showed an almost 2-fold increase in the tensile strength (Krajangsawasdi et al. 2021). The strength versus density graphs of the conventionally produced metals and the additively manufactured polymer composites are shown in Figure 2.17 (Nawafleh and Celik 2020). By increasing the carbon fiber volume content up to 28%, a 45% weight reduction is possible compared to Aluminum at the same strength and by increasing the carbon fiber volume up to 46%, an 80% weight reduction is achieved as compared to Steel 4140.

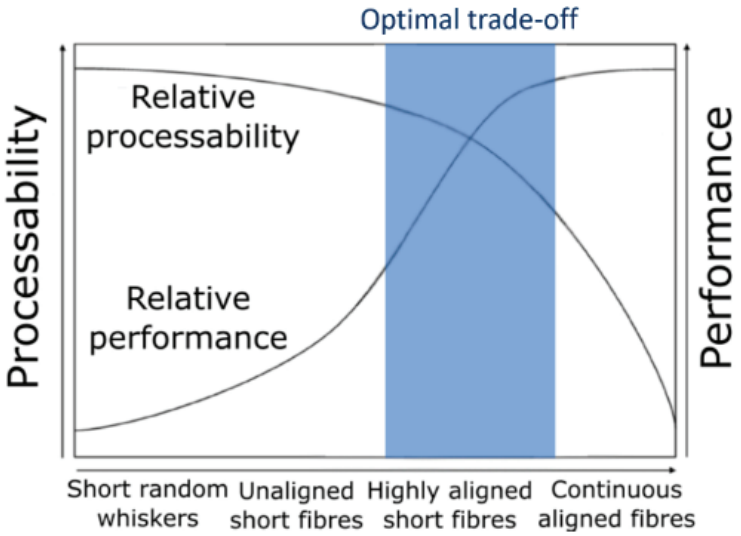

Figure 2.15. The balance between performance and processability of various types of fibers (Source: Blok et al., 2020)

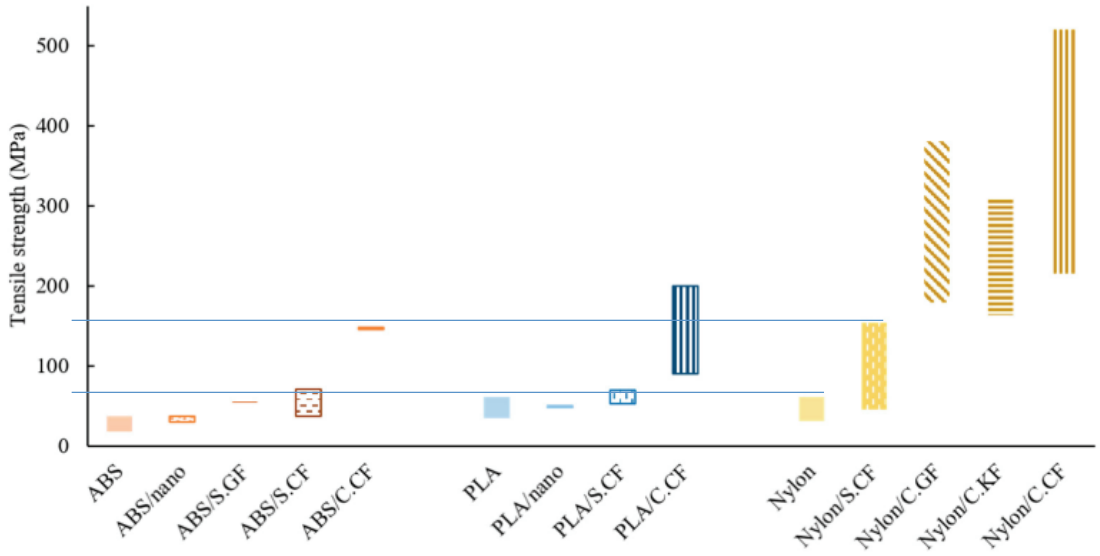

Figure 2.16. The tensile strength comparison of various types and materials reinforced ABS, PLA and Nylon (Source: Krajangsawasdi et al., 2021)

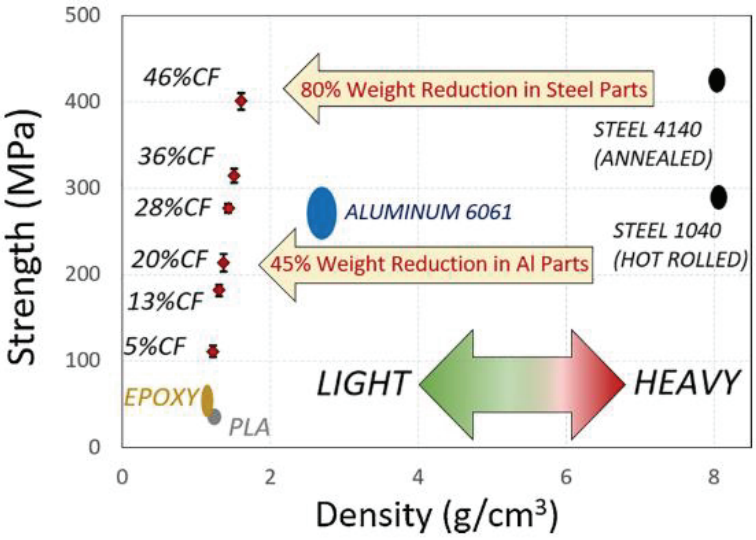

Figure 2.17. Density versus strenght comparison of additively manufactured composites and metals (Source: Nawafleh et al., 2020)

In additively manufactured composites, thermoset matrices are stronger and have higher service temperatures than thermoplastic matrices and long fiber reinforcement is more effective than short fiber reinforcement (Figure 2.18) (Monticeli et al. 2021). The fiber material, form and fiber content are important as they affect the tensile strength as depicted in Figure 2.19 (Li et al. 2022). It is seen in the same figure that the composites manufactured by FDM have higher tensile strength than the composites manufactured by conventional compression molding. Additionally, carbon fiber reinforcement is more effective than glass and Kevlar fiber reinforcement (Figure 2.20) (Li et al. 2022).

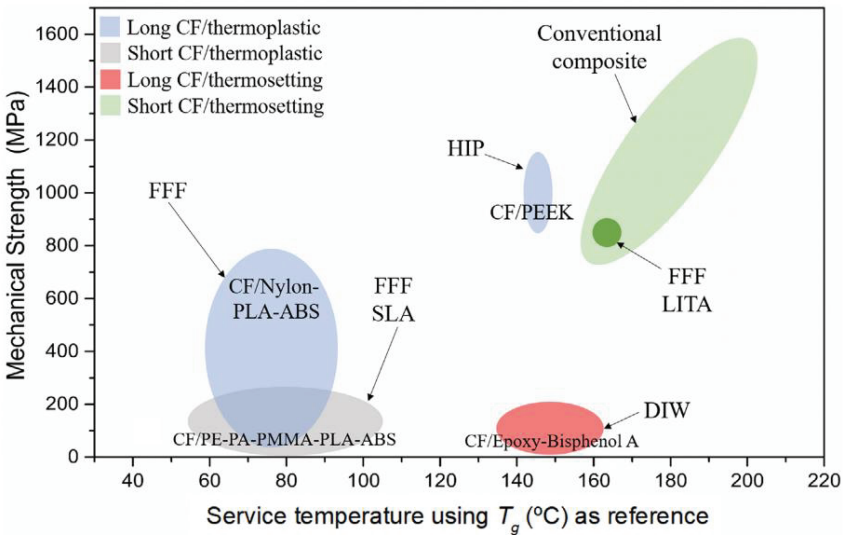

Figure 2.18. The classification of processing methods with different additively manufactured composites with respect to glass transition temperature and strength (Source: Monticeli et al., 2021)

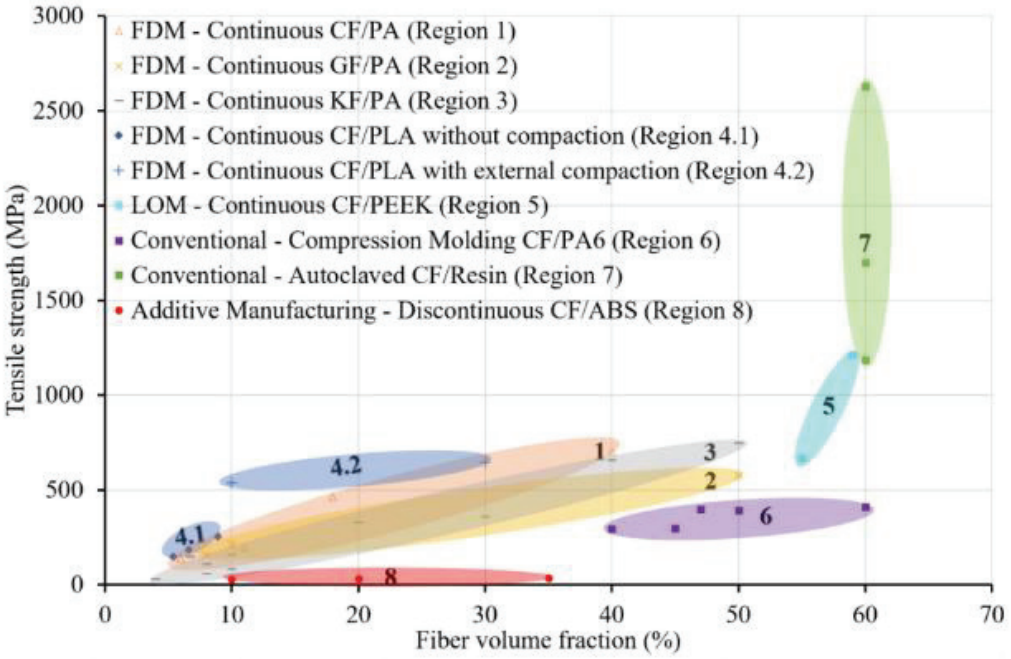

Figure 2.19. The comparison of additively manufactured composites versus conventional composite processes considering fiber volume fraction and tensile strength (Source: Li et al., 2022)

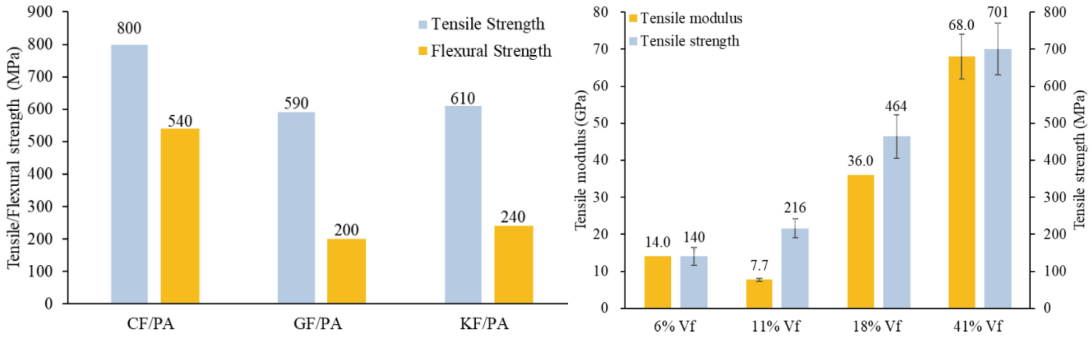

Figure 2.20. (a) CF, GF and KF reinforcement in PA matrix tensile and flexural results, (b) Effect of Carbon fiber volume fraction in PA matrix (Source: Li et al., 2022)

Adding reinforcements into a matrix not only increases the mechanical performance but also enhances the heat conductivity. When the heat conductivity increases, more heat is transferred to the newly deposited layers, therefore it enhances the inter-layer bonding and part's strength. The heat transmission increases due to the fibers inside the matrix, leading to reduced thermal residual stress and localized high temperature points. Furthermore, the inclusion of fibers reduces the coefficient of thermal expansion (CTE), minimizing warping and ensuring the dimensional accuracy during manufacturing (Krajangsawasdi et al. 2021)(Love et al. 2014).

2.7. The Effecting Parameters

The layer by layer deposition strategy leads to anisotropy in mechanical and thermal conditions. The process parameters affecting the anisotropy include temperature, build plate temperature, feed rate, head velocity, build direction, contour number, build angle, raster angle, length and diameter, etc. Additional anisotropy occurs due to the reinforcement in the composite and the factors affected that this additional anisotropy include the fiber percentage, fiber material, fiber distribution, fiber orientation, etc. Therefore, these parameters should be adjusted in order to produce desired parts effectively. For example, the heat conduction gets higher with increasing fiber content in the fiber direction in the FDM as depicted in Figure 2.21(Liao et al. 2018).

2.7.1. The Effect of Layers' Orientation

One of the studies about the comparison of thermal properties of pure PA12 and short carbon fiber reinforced PA12 with different percentages depends on reinforcement carbon fiber content and building direction of the 3D printed specimen also it is illustrated in Figure 2.21. This study resulted in that increase of short carbon fiber increases the maximum degradation temperature which exhibits an improvement in thermal stability. The addition of carbon fibers increases the tensile modulus and thermal conductivity (Figure 2.21) and when the orientation of fibers becomes more parallel to heat flow, its conductivity increases(Liao et al. 2018).

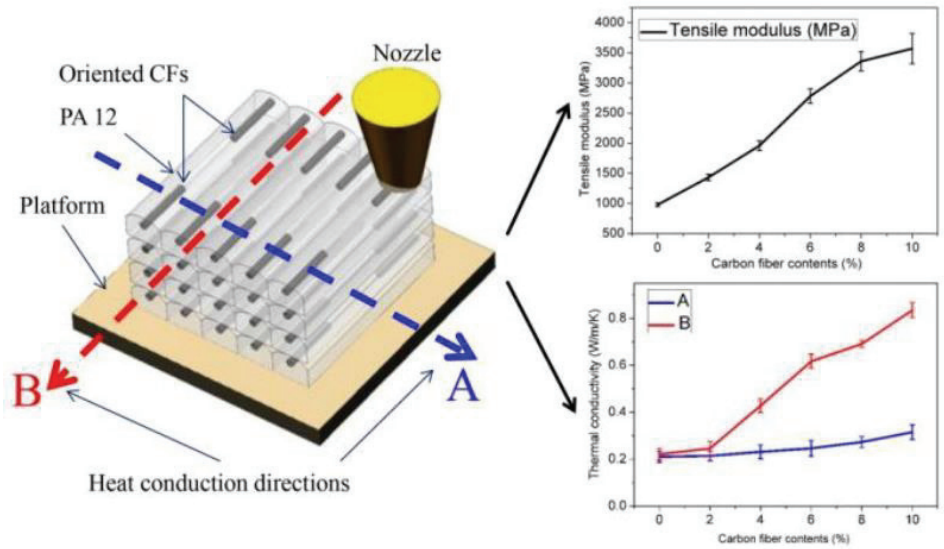

Figure 2.21. Effect of printing and fiber direction on thermal conductivity (Source: Liao et al., 2018)

2.7.2. The Effect of Fiber Reinforcement

Pascual-González et. al. (Pascual-González et al. 2020) determined the fiber volume content of an FDM-Onyx composite printed using +-45 raster angle through three different methods; digestion, pyrolysis and thermogravimetric analysis (TGA). The average diameter and length of the used Onyx filament were 8.4±0.5 μm and 35±5 μm, respectively. The fiber volume percentages were determined sequentially 10.9, 11 and 9.6% for digestion, pyrolysis and TGA. The tensile tests were performed on the neat polymer (Nylon 6) and Onyx composite test specimens for comparison. Nylon was shown to have a lower elastic modulus, 0.8 GPa and a yield stress, 25 MPa (Figure 2.22). Onyx showed a nearly bilinear elasto-plastic behavior, with an elastic modulus of 1.2 GPa and yield stress of 39 MPa as seen in Figure 2.22. In another study (Mulholland et al. 2018), the fiber orientation and fiber volume content of an additively manufactured short carbon fiber reinforced polyamide composite heat exchanger. The fiber orientation was determined by using micro computed tomography (μCT) and fiber content with a burn-off test at 450^{o}C under a nitrogen atmosphere. The results showed that 81% of the fibers in the extruded Onyx filament were aligned in the printing direction(a_{11}) (Figure 2.23). The fiber weight and volume percentages of the filament were determined 14.1 and 12%,

respectively. The length and diameter of the fibers in the Onyx manufactured parts were also determined using optical microscopy (Sauer 2018). The average length of the fibers was found 108.2 μm after 19 measurements and the average diameter was 7.36 μm after 13 measurements. The fiber volume fraction and fiber direction were determined in the same study using the ImageJ tool image processor. The fiber volume content by these methods was determined 9.129%. The average directional distribution of short carbon fibers was measured as 0.226 degrees with an 85.5 percent goodness (Figure 2.24). In FDM production method the alignment of fiber materials was provided by shear force field. The angle in nozzle geometry ensures the fibers inside the filament orient through the extruding orifice (Wu et al. 2020b), (Niendorf and Raeymaekers 2021), (Yang et al. 2021). The shear force field and μCT images of filament were shown in Figure 2.25 and exhibit how fibers align in the extruding direction. Peng et. al. investigated the synergistic reinforcement of polyamide-based composites by the combination of short and continuous carbon fibers via FDM (Y. Peng et al. 2019). The weight percentage of short carbon fiber reinforced polyamide (SCFRPA) was determined 15% using TGA (Figure 2.26). The graph of TGA test results and SEM images of SCFRPA tow shown in Figure 2.26 (b). Benfriha et. al. determined the short carbon fibers mass content of an Onyx (PA6+SCF) filament through pyrolysis at 500ºC (Benfriha et al. 2021). The fiber content was determined 6.5%. The microscope images of the fibers after pyrolysis and in the composite are shown in Figure 2.27(a) and (b), respectively. The size range of short carbon fibers was determined 10-312 μm and the fibers were oriented along the length of the filament due to the applied extrusion during filament processing. As a summary, the methods used to determine the fiber content, length and diameter and the measured values of them are tabulated in Table 2.4.

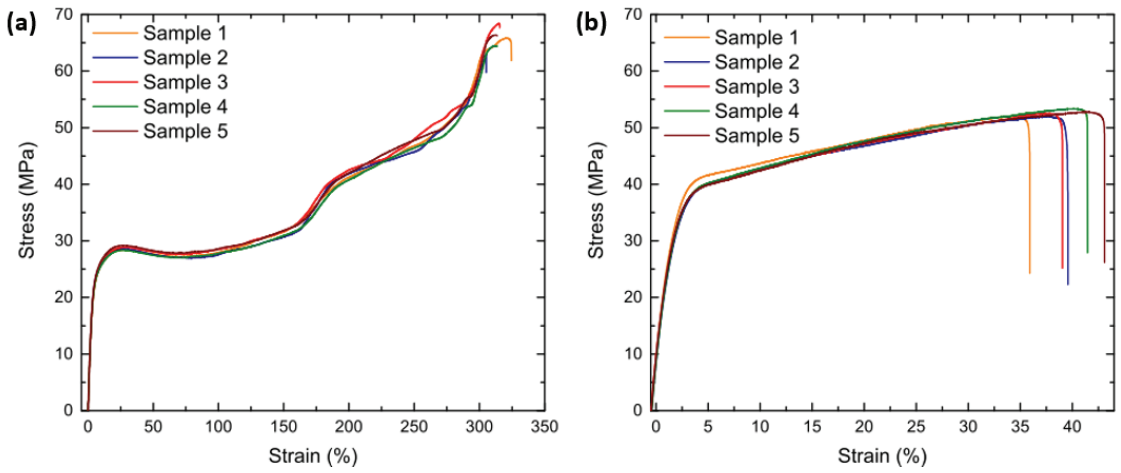

Figure 2.22. Tensile test results of (a) Nylon 6 and (b) Onyx
(Source: Pascual-Gonzalez et al., 2020)

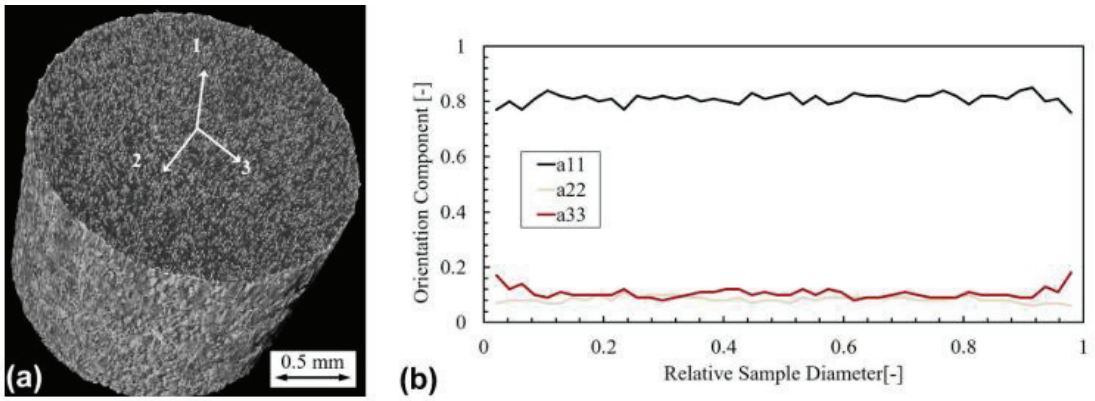

Figure 2.23. (a) µCT analysis of Onyx filament, (b) Fiber distribution in Onyx filament
(Source: Mulholland et al., 2018)

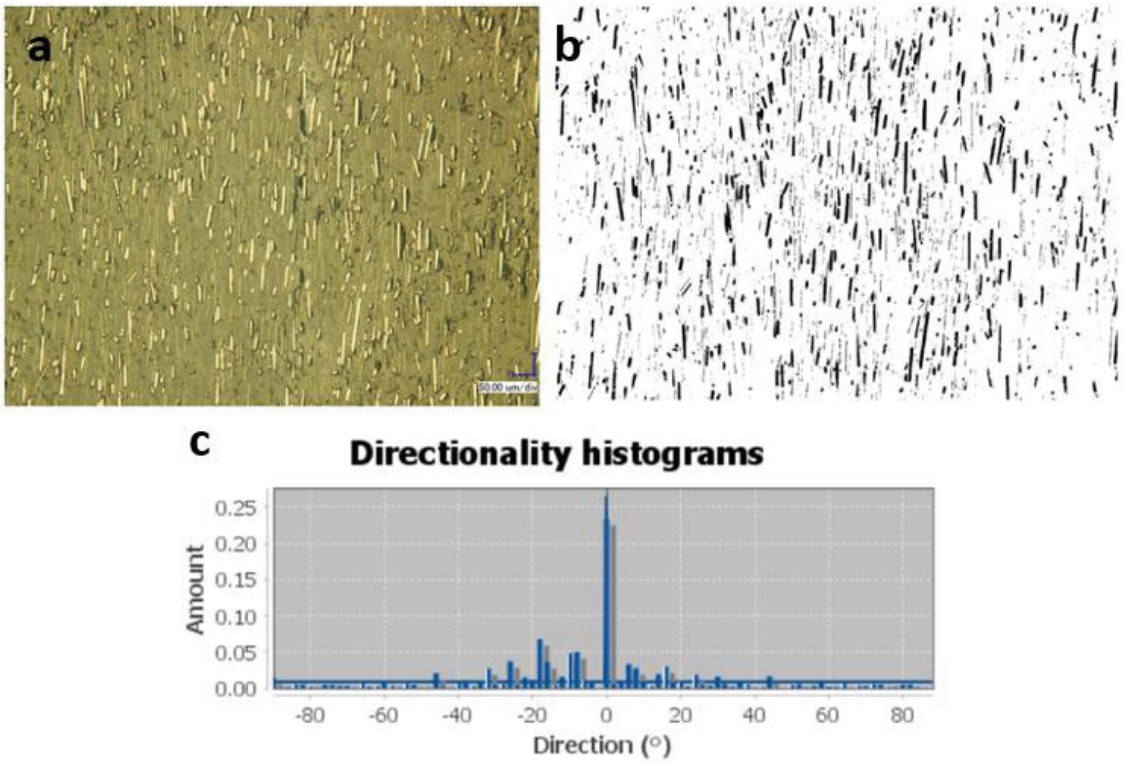

Figure 2.24. (a) Optical microscopy image of Onyx, (b) Image processing with ImageJ tool, (c) Short carbon fibers orientation (Source: Sauer et al., 2018)

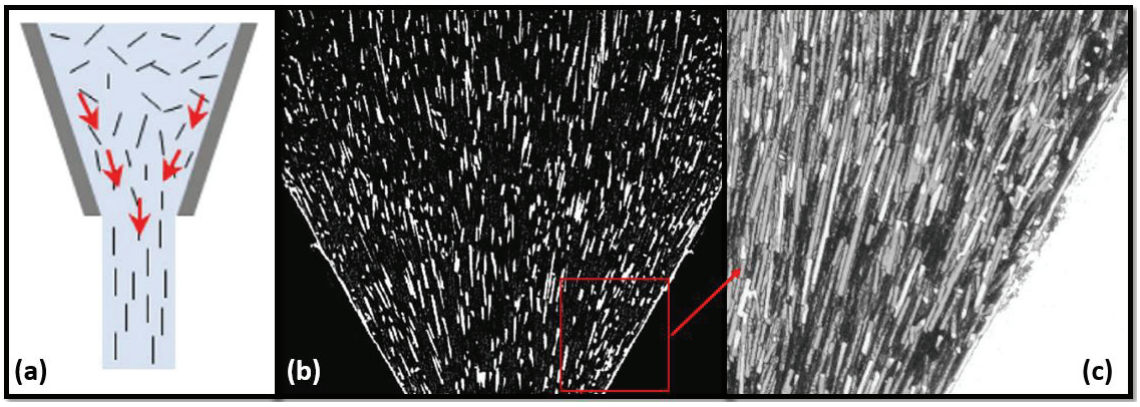

Figure 2.25. The effect of shear force field on fibers' alignment (a) representative image of shear force field (Source: Niendorf et al., 2021), (b)-(c) μCT images of filament inside the extruding nozzle (Source: Yang et al., 2020)

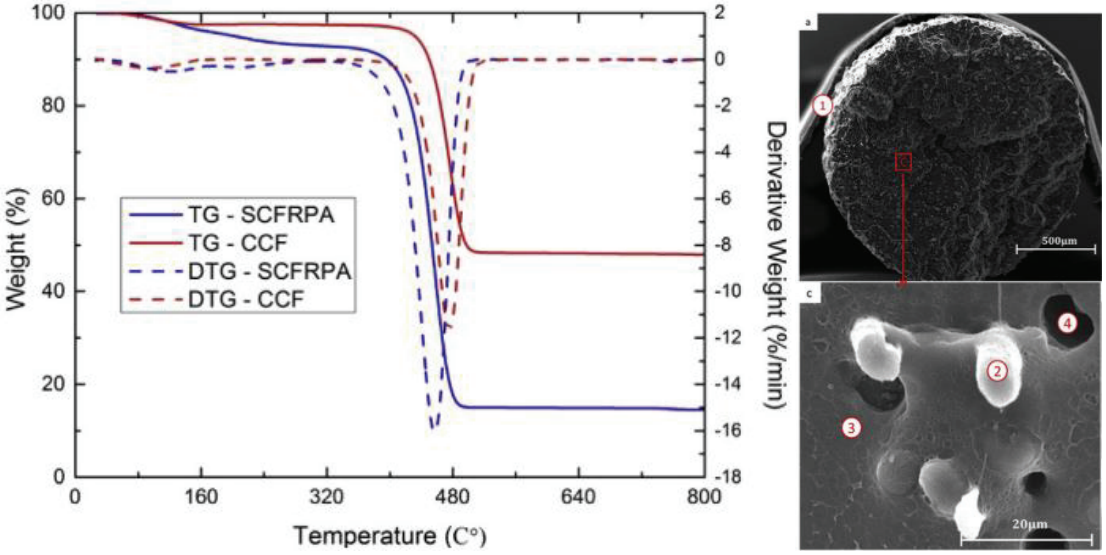

Figure 2.26. (a) TGA test results of continuous and short carbon fiber reinforced polyamide, (b) SEM images of Onyx filament (Source: Peng et al., 2019)

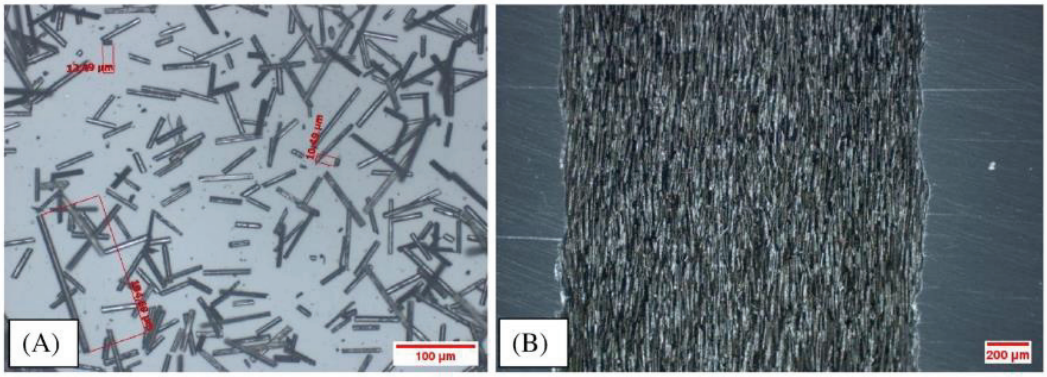

Figure 2.27. (a) Short carbon fibers after pyrolysis test, (b) Short carbon fibers distribution of Onyx filament (Source: Benfriha et al., 2021)

Table 2.4. The summary of the fiber percentage calculation studies

Sequence	Material	Method	Results	Average diameter and length	References
1	Onyx	Digestion, Pyrolysis, TGA	Volume Fraction 10.9% 11% 9.6%	8.4±0.5 µm in diameter 35±5 µm in length	(Pascual-González et al. 2020)
2	Onyx	Mikro Computed Tomography (µCT), Burn-off test at 450°C	Volume Fraction 12%, Weight Fraction 14.1%	Fiber Orientation 81% in printing direction	(Mulholland et al. 2018)
3	Onyx	Optical Microscopy	Volume Fraction 9.129%	7.36 µm in diameter 108.2 µm in length and Fiber Orientation 85.5% in printing direction	(Sauer et al. 2018)
4	Onyx	TGA	Weight Fraction 15%	-	(Y. Peng et al. 2019)
5	Onyx	Pyrolysis	Weigth Fraction 6.5%	10-312 µm in size	(Benfriha et al. 2021)

2.7.3. The Fiber Ratio and Orientation Effect

Short fiber reinforced polymers are mostly produced by injection molding in the industry. Anisotropic tensile behavior of injection molded short glass fiber reinforced polyamide6 with varying fiber contents was previously investigated (Holmström, Hopperstad, and Clausen 2020). The distribution and orientation of polyamide6 reinforced with 0 wt.%, 15 wt.%, 30 wt.% short glass fibers were measured using X-ray computed tomography in the same study. The composite specimen was produced as a plate geometry with the x-axis was the mold flow direction and the z-axis was the thickness direction (Figure 2.28(a)). The specimen was divided into 9 sections and the fiber orientations in each section were determined (Figure 2.28 (b)). The fibers in the near-surface areas were shown highly oriented in the mold flow direction, and the fibers in the core region were oriented perpendicular to the mold flow direction (Figure 2.28 (c)). The composite tensile test specimens were extracted by rotating 15-degree increments from the produced plate (Figure 2.29). The tensile tests showed that the highest strength was seen in the mold flow direction and the strength increased with increasing the fiber content (Figure 2.30). While increasing the fiber lowered the ductility.

Also, it was concluded that when the amount of fiber increases, the material behaves more anisotropic.

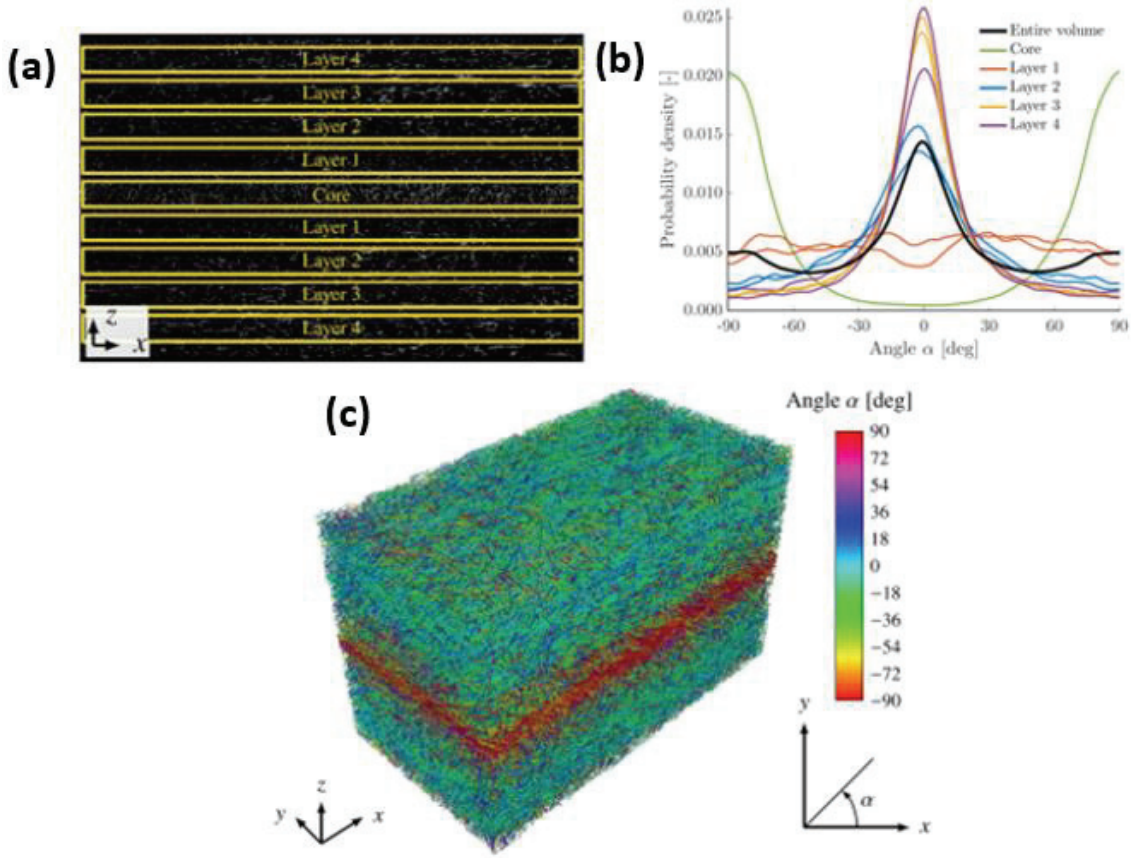

Figure 2.28. (a) Sections of specimen, (b) Fiber orientations in different sections, (c) µCT analysis of specimen with colorized fiber orientation angles (Source: Holmström et al., 2020)

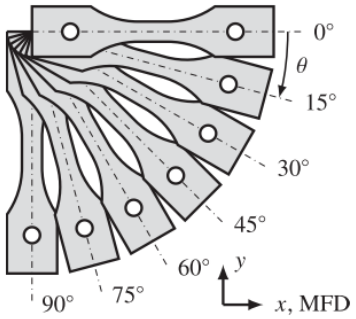

Figure 2.29. Tensile test specimens and angle between mold flow direction (Source: Holmström et al., 2020)

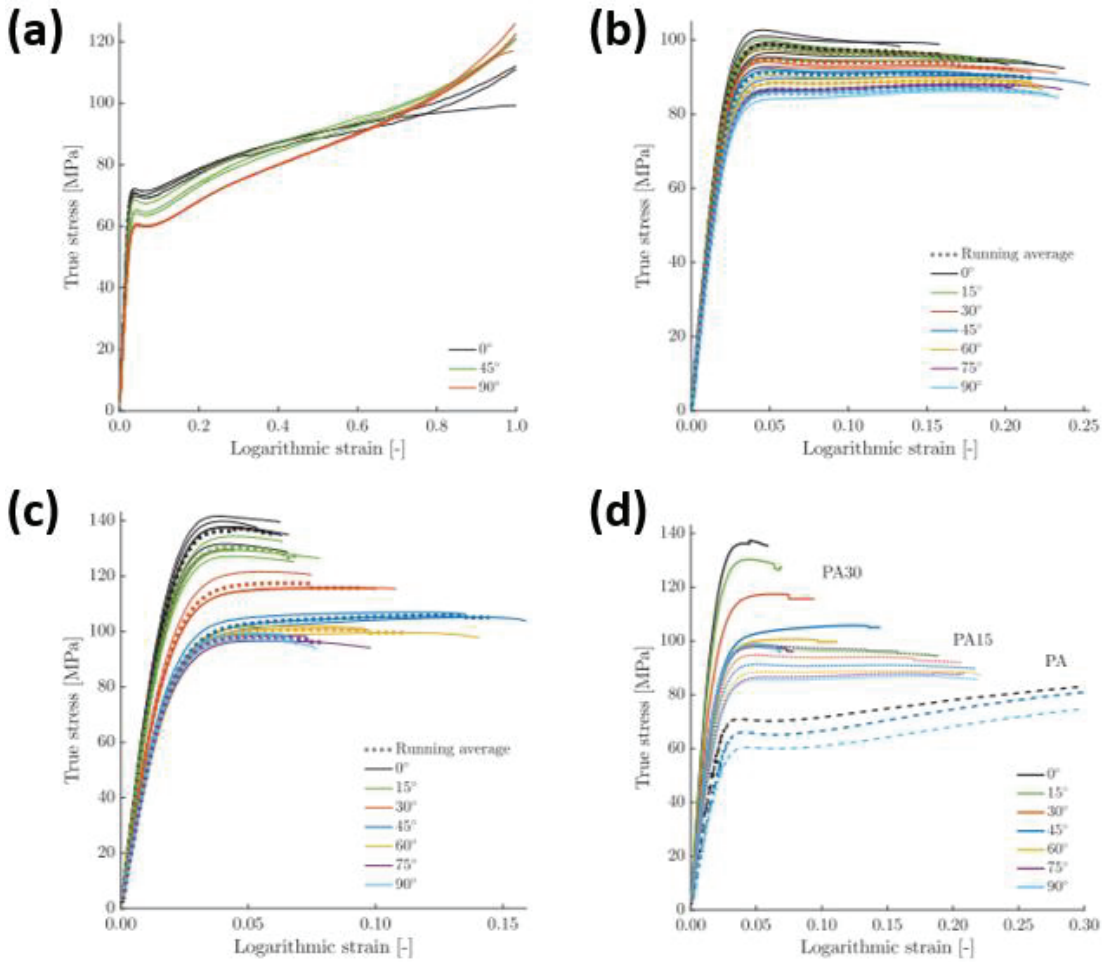

Figure 2.30. Tensile test results of (a) Pristine PA with three different angle, (b) 15% short glass fiber reinforced PA with different angles, (c) 30% short glass fiber reinforced PA with different angles, (d) comparison of fiber reinforment amount and fiber orientation angles (Source: Holmström et al., 2020)

2.7.4. The Effect of Layer Thickness

The FDM manufactured parts consist of layers; therefore, it is important to identify the effects of layer thickness and orientation (raster angle) and the build orientation on the mechanical properties. The previously tensile tests (Benfriha et al. 2021) were performed on 0.1, 0.2 and 0.3 mm layer height Onyx (PA6+SCF) specimens. The specimen with 0.1 mm thickness was shown to have higher strength than the specimen with 0.2 mm thickness (Figure 2.31(a)). The increase of the layer height decreased the liquidity of printed layers and this induced a low adhesion and bonding in the printed layers (Figure 2.31(b)). In-situ temperature measurements (Figure 2.31(c))

further showed that printing with 0.1 mm layer height cooled slower and more homogenously than higher-layer height prints. The slow cooling enhanced the crystallinity of the structure, leading to an increase in the mechanical properties. Durga Prasada Rao el. al. investigated the layer height effect on a short carbon fiber reinforced PLA produced by the FDM technique and showed lower layer height yielded higher tensile and compression strength than higher-layer heights (Durga Prasada Rao, Rajiv, and Navya Geethika 2019). Additionally, Nomani et al. investigated the effect of layer height on the tensile and compression behavior of 3D printed ABS and observed that the strength of material increases with reduced layer height under the both tension and compression loads (Figure 2.32 (a) and (b)) (Nomani et al. 2020). The low layer height caused an increase in the bonding area between the layers.

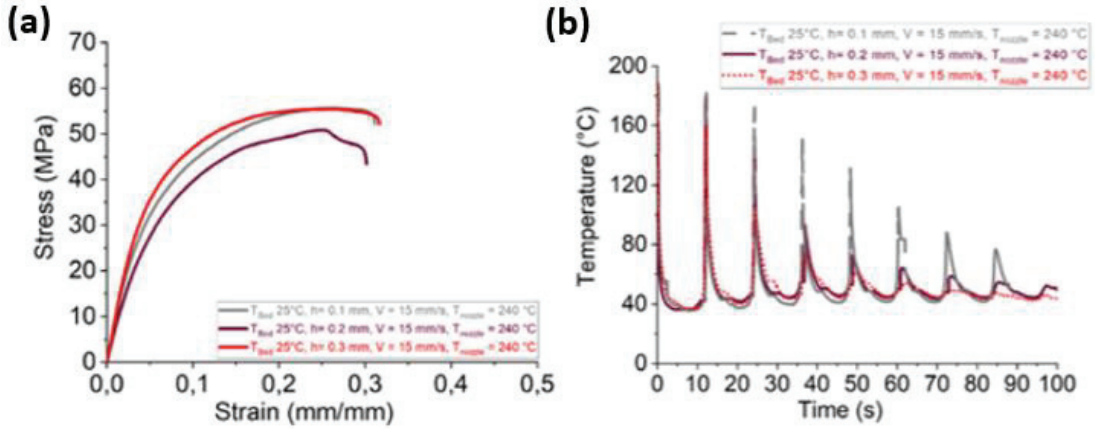

(c)

Conditions		T_c (°C)	T_m (°C)	%crystallinity
No. 3	h = 0.1 mm	162.82°C	198.72°C	20.51%
	h = 0.2 mm	161.50°C	197.79°C	19.27%
	h = 0.3 mm	161.68°C	197.48°C	21.22%

Figure 2.31. (a) The effect of layer thickness on tensile properties, (b) Temperature measurements while printing with different layer thicknesses, (c) DSC analysis results of different layer thicknesses (Source: Benfriha et al., 2021)

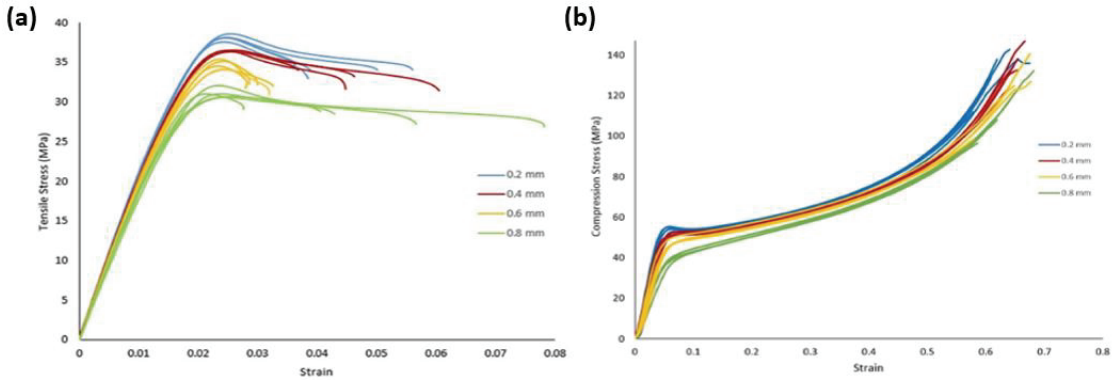

Figure 2.32. The effect of layer thickness on (a) Tensile behaviour, (b) Compressive behavior of FDM-printed PLA (Source: Nomani et al., 2020)

The impact strength of a nylon produced by using the fused deposition modeling technique in Markforged Mark Two 3D Printer was investigated using the Charpy impact test (Caminero et al. 2018). The results showed that the layer thickness variation affected the impact performance of flat and on edge specimens differently in an unreinforced nylon matrix. The impact strength increased when layer thickness increased in flat printed specimens and vice-verse in on edge specimens (Figure 2.33). In flat samples, as the impact loading is parallel to the neighboring layers, most of the applied load was taken by the layers. This effect was explained by the fact that as layer thickness increased, fewer layers were required for a given overall thickness, reducing the number of layer bonds (bonding failure) and increasing impact strength. But in the on-edge samples, the load was applied perpendicular to individual layers and by increasing the layer thickness, the number of individual layers decreased so impact strength decreased. The SEM images of Charpy impact tested samples are illustrated in Figure 2.34, and failure in flat printed samples exhibited a more ductile fracture and in on-edge printed samples showed a more brittle fracture due to lower bonding between layers because of porosity. Barnik et. al. investigated the effect of layer thickness on the tensile behavior of an Onyx material produced by Markforged Mark Two printer with different number of layers (Bárnik et al. 2019). Increasing the number of layers increased the tensile strength, while 0.2 mm layer height specimen showed a higher strength than 0.1 mm height layer specimen when the thickness of 0.2 mm layer height specimen increased (Figure 2.35). Zhao et. al. investigated the effect of printing angle and layer thickness on the tensile strength and elastic modulus of FDM printed PLA. The tensile strength and elastic modulus increased with increasing printing angle, while both decreased with increasing layer thickness

(Figure 2.36). When the printing angle was more close to the loading axis, the tensile strength and Young's Modulus increased (Zhao, Chen, and Zhou 2019).

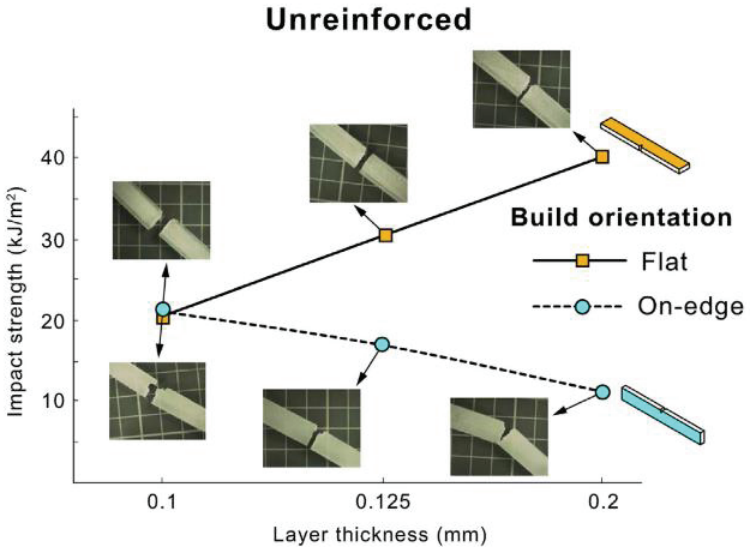

Figure 2.33. Effect of layer thickness and build orientation on impact strength of Nylon 6 (Source: Caminero et al., 2018)

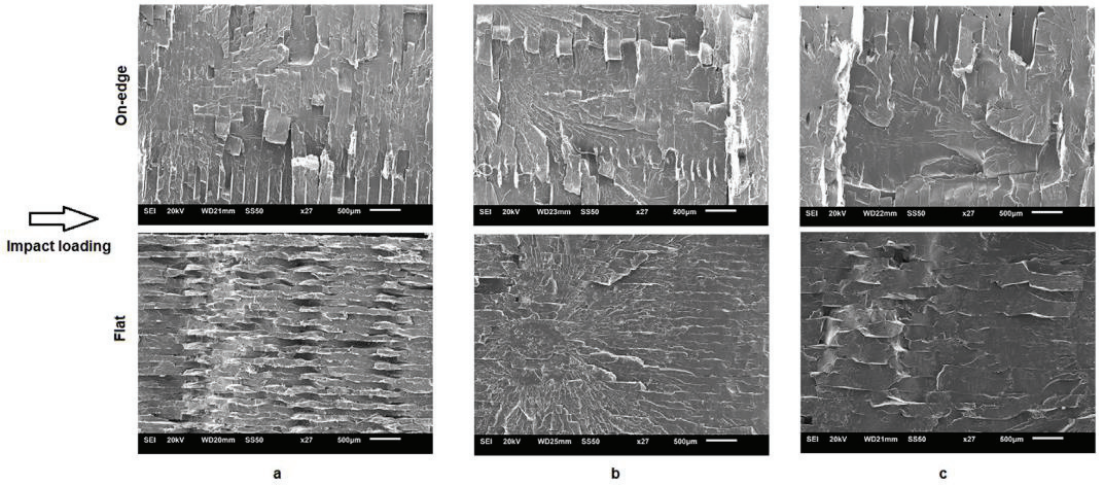

Figure 2.34. SEM images of different layer thickness nylon specimen's fracture surfaces (a) 0.1 mm layer height, (b) 0.125 mm layer height, (c) 0.2 mm layer height (Source: Caminero et al., 2018)

Ultimate stress [MPa]	Layer thickness [mm]	Number of layers	Specimens dimensions [mm]
22.8	0.2	5	15×1×250
27	0.1	10	15×1×250
33.4	0.2	10	25×2×250

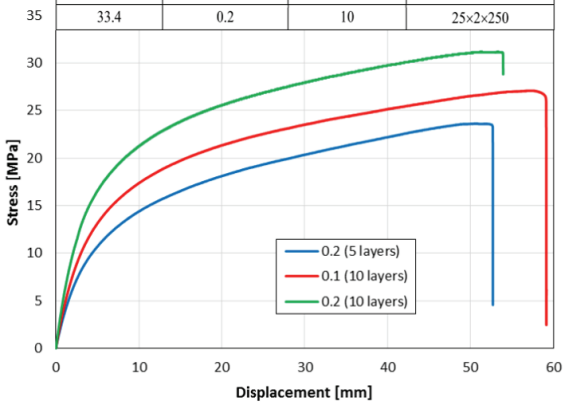

Figure 2.35. Tensile test results of different layer thicknesses and numbers of layers specimens (Source: Barnik et al., 2019)

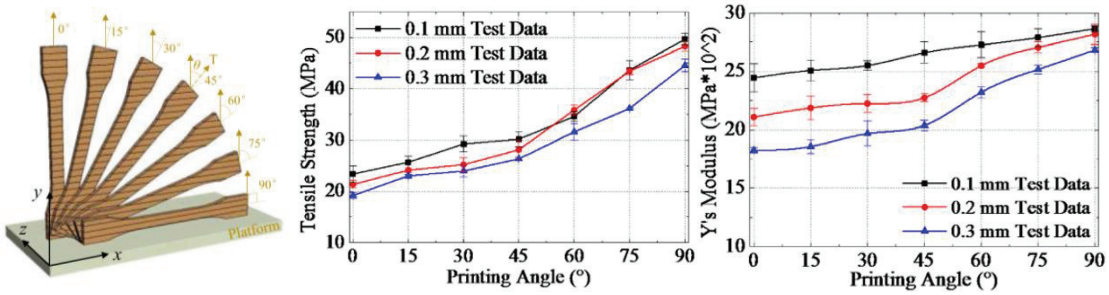

Figure 2.36. (a) Printing angle of tensile test specimens, (b) Tensile strength and (c) Young modulus results different layer thickness and printing angle specimens (Source: Zhao et al., 2019)

2.7.5. The Effect of Contour Numbers

In the FDM process, parts consist of infill patterns and outer shells. Infill patterns can be adjusted in different geometries such as triangular, rectangular, hexagonal and gyroid. Outer shells wrap the infill geometry's perimeter. Thus they bond the infill pattern's endpoints, protect infill patterns from the environment and provide better surface quality. By wrapping the infill pattern, the stress concentration at the infill pattern's and raster's end is prevented. Lanzotti et. al. investigated the effect of perimeter number on tensile mechanical properties of FDM-produced PLA. It was shown that

increasing the perimeter number increased both tensile strength and failure strains (Figure 2.37) (Lanzotti et al. 2015).

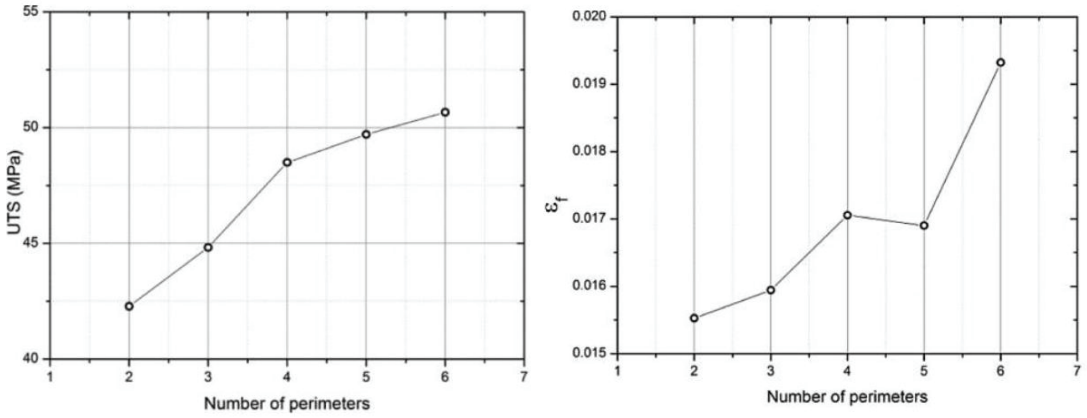

Figure 2.37. Effect of perimeters number on (a) Ultimate tensile stregth, (b) Strain at failure (Source: Lanzotti et al., 2015)

2.7.6. The Effect of Build Direction

The effect of raster orientation and build direction on the flexure behavior of ABS reinforced with different fibers was previously investigated (Wang et al. 2019). The raster orientation ([0/90] and [-45/+45]) and build direction (Horizontal and Side build) affected the crack formation, and propagation (Figure 2.38) and the stress-strain behavior and energy absorption (Figure 2.39). It was reported that [-45/+45] side-built specimens had better flexural performance and energy absorption. The three different building orientations shown in Figure 2.40, named “flat”, “on edge” and “upright” were investigated for their effect on the tensile strength of ABS and PC (Krajangsawasdi et al. 2021). The tensile strengths of “flat” and “on-edge” were similar and higher than those of the “upright” building direction (Figure 2.41).

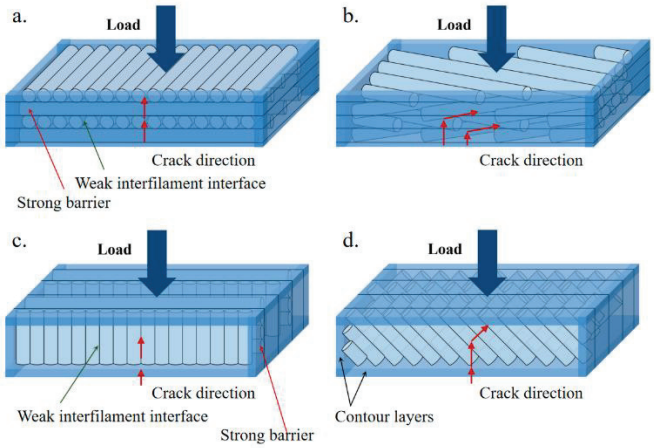

Figure 2.38. Crack formation considering build direction
(Source: Wang et al., 2019)

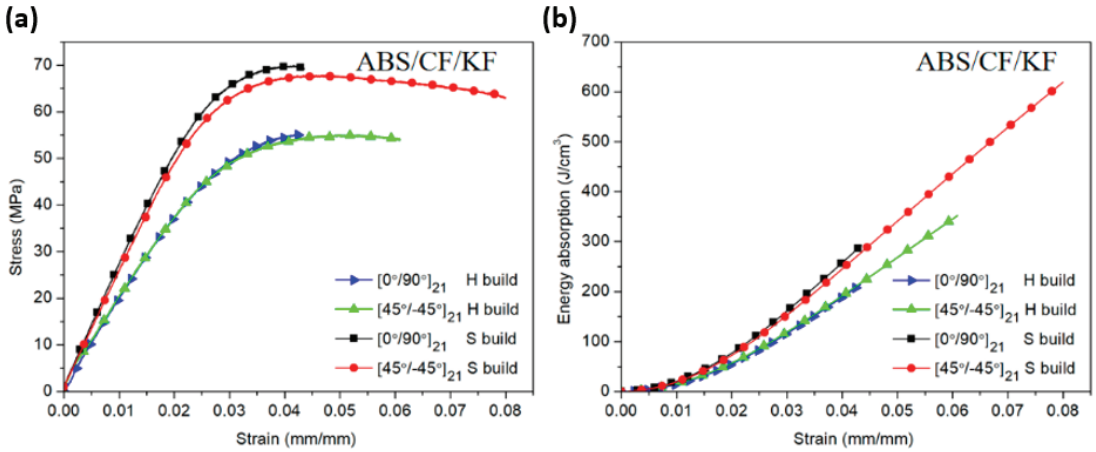

Figure 2.39. (a) Stress-strain graph of different raster angle and build direction printed ABS composites, (b) energy absorption performance of different raster angle and build direction printed ABS composites (Source: Wang et al., 2019)

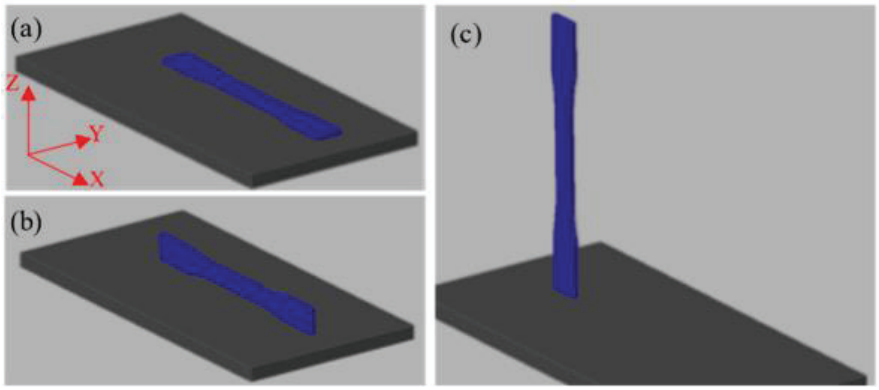

Figure 2.40. Build orientations (a) Flat, (b) On-edge, (c) Upright
(Source: Krajangsawasdi et al., 2021)

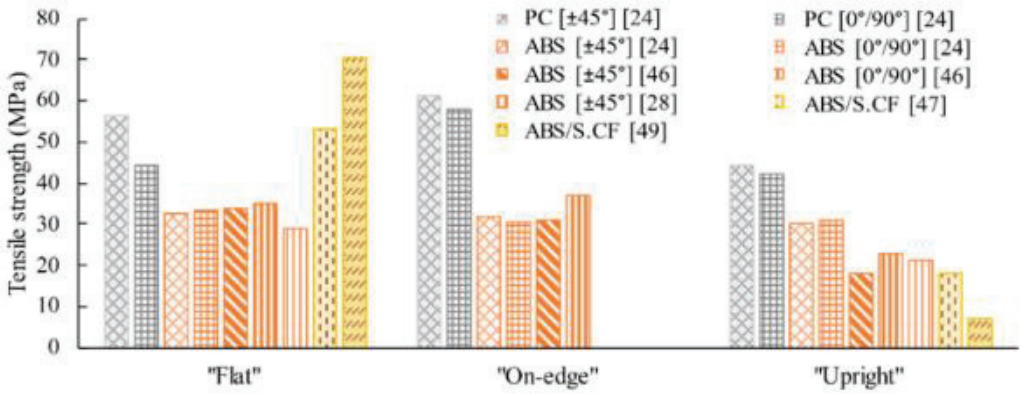

Figure 2.41. The tensile strength comparison of different build orientations, raster angles and materials (Source: Krajangsawasdi et al., 2021)

Boghozian et. al. investigated the compression behavior of FDM printed ABS in different deposition directions (Figure 2.42 (a-d)). The specimens were produced from 0-degree to 90-degree build angle in 10 degree increments with respect to the build plate. It was shown that 90-degree specimens exhibited higher yield strength due to the load expressed along the direction of beads so it prevented the material from shearing. Also, maximum stress before failure was observed on the 0-degree specimen because its layers were horizontally on top of each other which leads to withstand more compression load (Boghozian, n.d.).

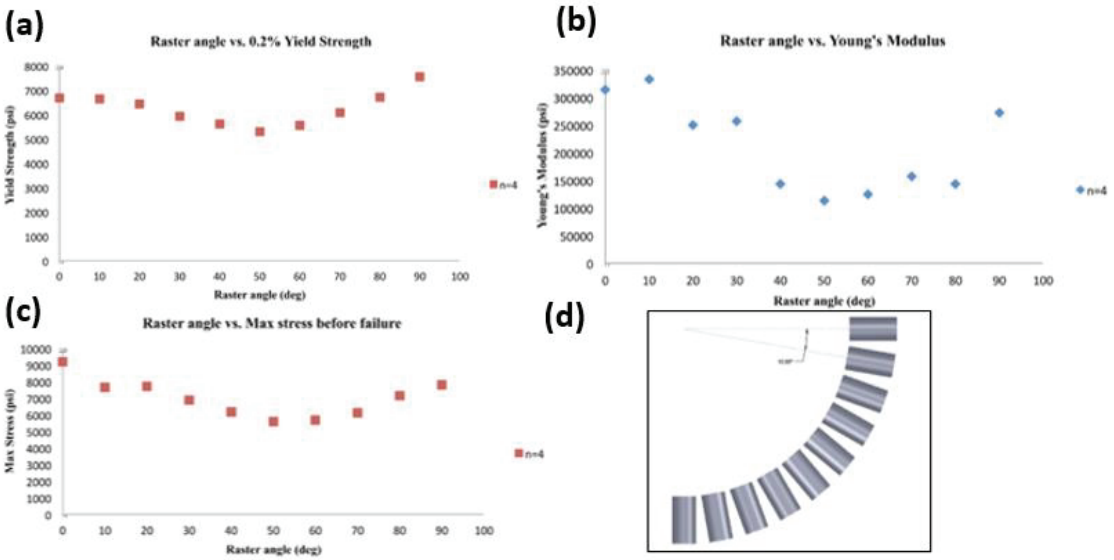

Figure 2.42. The compression behavior comparison of raster angle versus (a) Yield strength, (b) Young's modulus, (c) Maximum stress, (d) The compression test samples with 10 degree increments (Source: Boghozian et al., 2014)

2.7.7. The Strain Rate Sensitivity and Temperature Effect

Utzeri et. al. investigated the effect of strain rate on the compression behavior of an FDM short carbon fiber reinforced polyamide 6.6 matrix composite fabricated with three different build directions: vertical, longitudinal and transverse (Figure 2.44) (Utzeri et al. 2021). Both quasi-static and dynamic compression tests were performed. Dynamic compression tests were conducted using a Split Hopkinson Pressure Bar (SHPB) test apparatus. In these three different specimens, the strength increased as the strain rate increased, while the specimens became more brittle at increasing strain rates as depicted in Figure 2.44 (a-e). The tomography analysis (Figure 2.45) also showed the void distribution between layers in the z-direction was more heterogeneous.

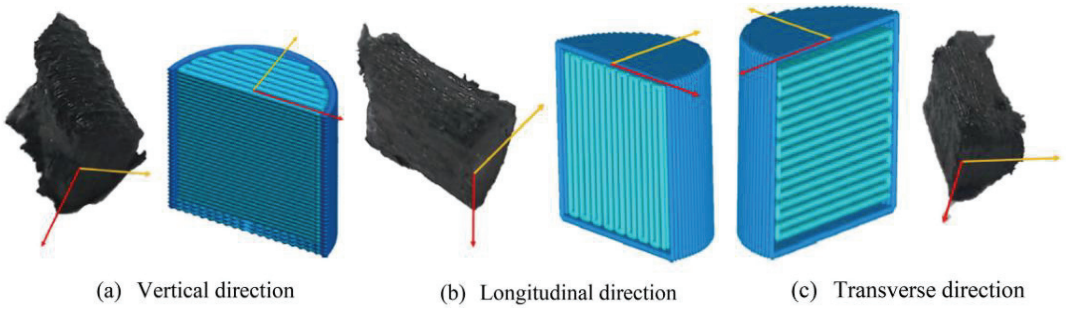

Figure 2.43. Three different build directions of short carbon fiber reinforced polyamide 6.6 (Source: Utzeri et al., 2021)

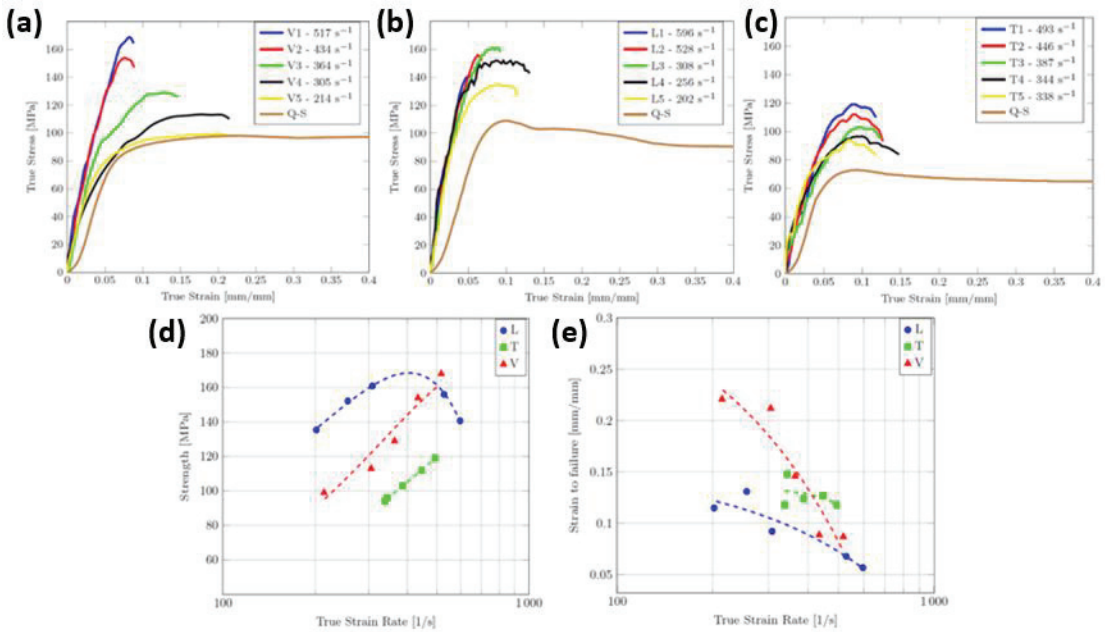

Figure 2.44. Tensile test results with different strain rates of (a) Vertical, (b) Longitudinal, (c) Transverse directions. Also the effect of strain rate on (d) Strenght, (e) Strain to failure (Source: Utzeri et al., 2021)

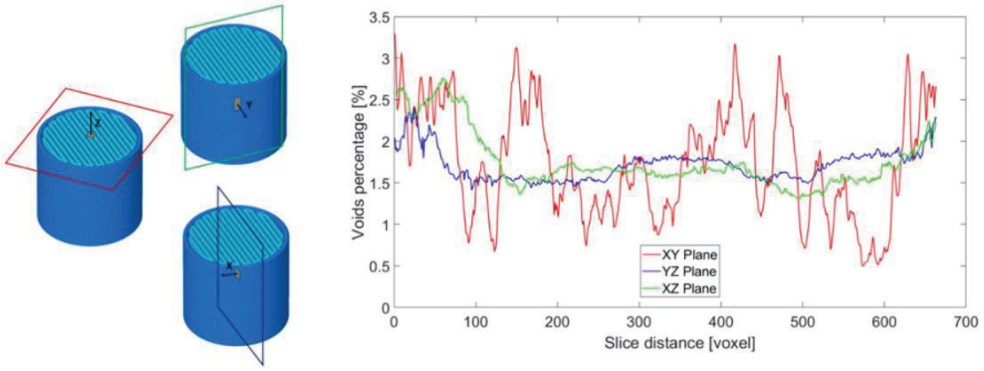

Figure 2.45. The tomography results considerin three different cross-section planes (Source: Utzeri et al., 2021)

Mortazavian et. al. studied the effect of strain rate and temperature on the tensile behavior of an injection molded short glass fiber reinforced polyamide 6 composites. The tensile tests were performed 0º, 90º and 45º to the mold flow direction between $5x10^{-5}$ and 1/s at -40, 85 and 125 ºC. For each direction of loading, the stress increased as the strain rate increased, while the failure strain decreased (Figure 2.46) (Mortazavian and Fatemi 2017). Both yield strength and elastic modulus were shown to be higher in the test parallel to the mold flow direction than 90º and 45º as seen in Figure 2.47. The rate sensitivities of tensile strength and elastic modulus were also shown to be direction

dependent, being higher in the tests parallel to the melt flow direction. An increase in the test temperature generally causes a decrease in the mechanical properties of thermoplastics. The increase in the temperature from -40ºC to 125ºC also decreased flow stresses (Figure 2.48 (a)) and the yield strength was shown to increase as the tensile strength increased at different temperatures (Figure 2.48 (b)). As the polymers show viscoelastic behavior, the strain rate sensitivity plays a key role in mechanical properties. According to Vidakis et. al., tested a Polyamide 6 (PA6) produced in -45/+45 orientation at 5 different strain rates (10, 25, 50, 75 and 100 mm/min). Within the study's strain rate regime, the strain rate sensitivity index (m) was found around 0 (Figure 2.49) (Vidakis et al. 2020).

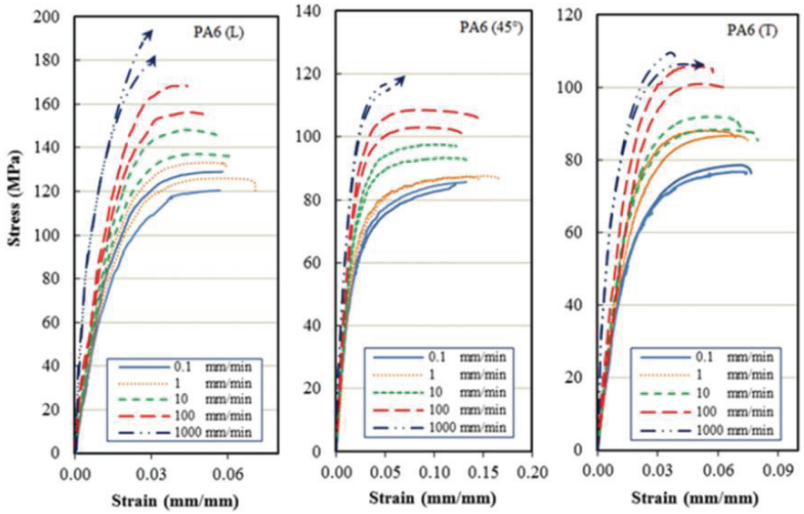

Figure 2.46. Tensile test results of PA6 with three different mold flow directions (Source: Mortazavian et al., 2017)

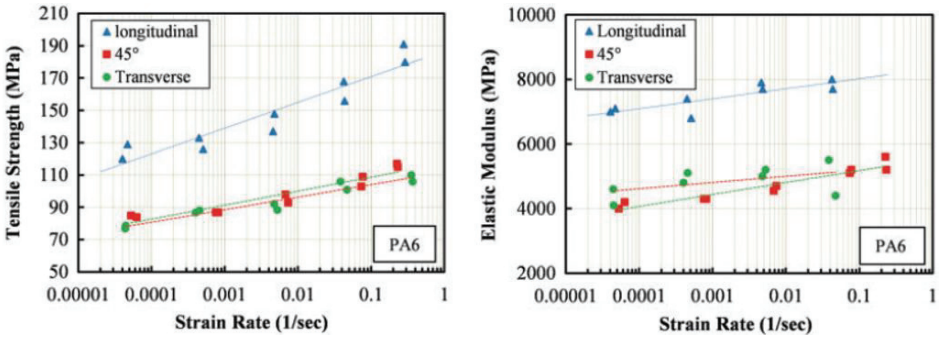

Figure 2.47. Variation of tensile strenght and elastic modulus considering different strain rates (Source: Mortazavian et al., 2017)

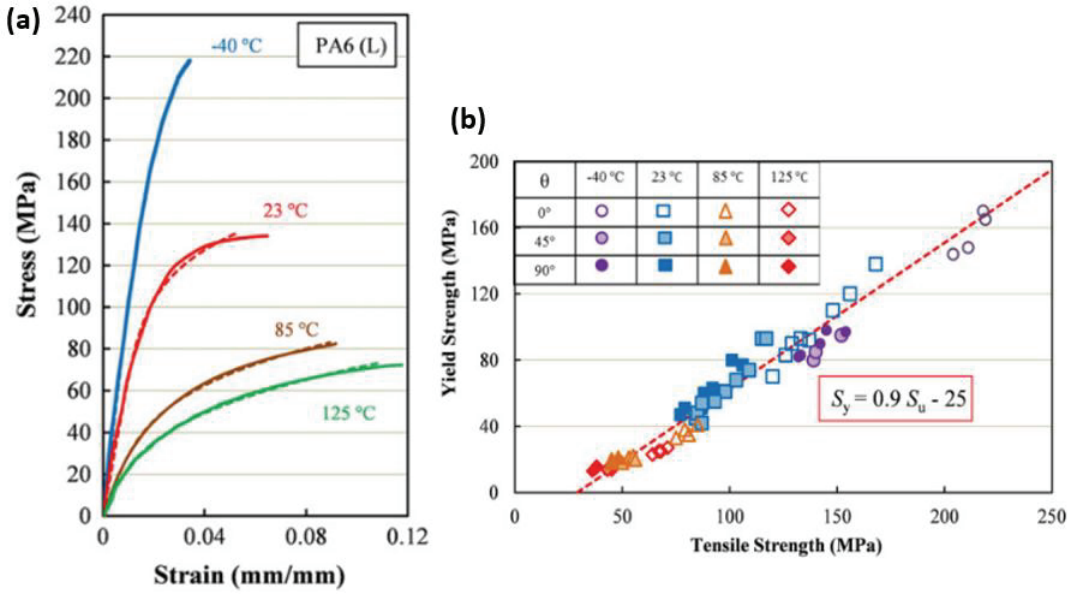

Figure 2.48. (a) The effect of temperature on tensile test results of longitudinal directional printed PA6, (b) The summary of the temperature and strain rate effect on tensile behavior (Source: Mortazavian et al., 2017)

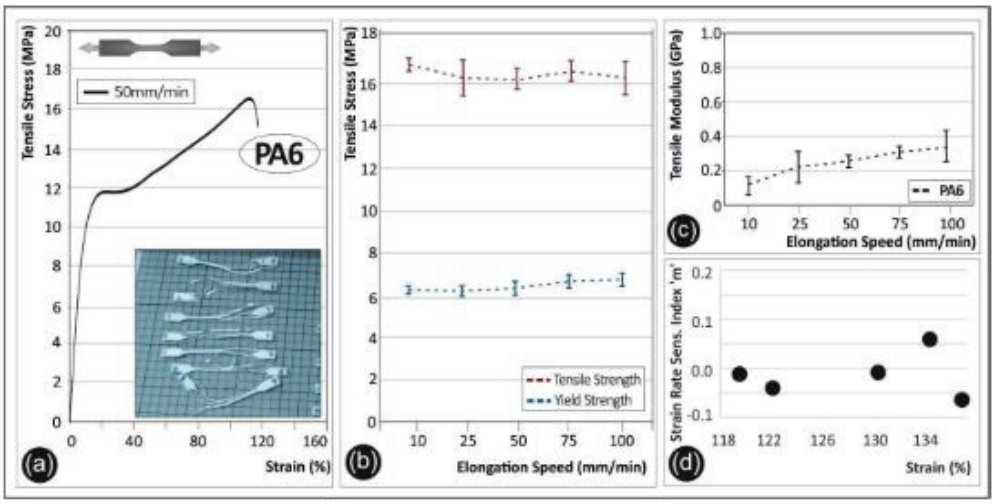

Figure 2.49. Tensile test results of PA6 (a) Strain versus stress graph, (b) Change of tensile and yield strength, (c) Tensile modulus with different elongation speeds, (d) Strain rate sensitivity index of PA6 (Source: Vidakis et al., 2020)

Pankow et. al. investigated the effect of specimen size and shape on the dynamic compression of PA in a SHPB. As the L/D (length to diameter ratio) increased both the flow stress and elongation rate decreased (Figure 2.50 (a) and (b), respectively) (Pankow, Attard, and Waas 2009). On the other side, a negligible effect of circular and square cross-section specimen shape on the flow stress and elongations were shown (Figure 2.50 (c) and (d), respectively).

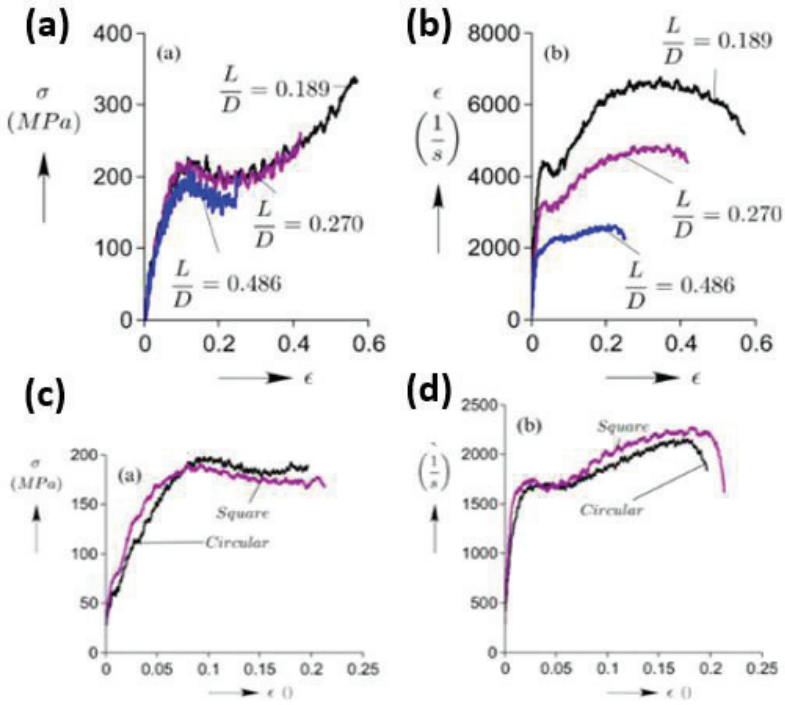

Figure 2.50. Effect of L/D ratio on (a) stress versus strain, (b) strain rate versus strain, Comparison of square and circular specimen shape (c) stress versus strain, (d) strain rate versus strain (Source: Pankow et al., 2009)

2.8. Thesis Objective

In the automotive and aviation industry, producing lightweight parts is always the major priority. The low weights reduce energy consumption. The contribution of composite materials with outstanding strength to weight ratios has enabled the production of such lightweight items. Especially the polymer matrix composites are commonly used in the automotive and aviation industry last decades. The structural components which are exposed to a collision or impact were manufactured from thermoplastic matrix composites such as bumpers in the automobile body because of their ductile behavior. Such structures work under dynamic loads or impact and it is well known that the polymers are strain-rate dependent materials. Therefore, before producing such components from thermoplastics the mechanical characteristics and strain rate sensitivity should be examined.

The scope of this study is the determine the effect of strain rate on the deformation behavior of additively manufactured composites. Composites are a mixture of a minimum

of two different materials and behave as one piece. The addition of fibers changes the behavior of material positively as desired. In this thesis, the compressive behavior is focused and the effect of the addition of fibers into a matrix is examined. The composite specimens and pristine polymer specimens were produced by using the Fused Deposition Modeling technique. The reinforcement element is short carbon fibers and the matrix element is Polyamide 6 (Nylon 6). The manufacturing of products with composite material by using FDM brings about a highly anisotropic behavior. For example, the fibers' dimensions, orientation, volume fraction, fiber material, matrix material are the effect of composites on anisotropy and process parameters are the effect of the FDM technique on anisotropy.

In order to obtain the strain rate sensitivity of the materials, quasi-static and high velocity compression tests were performed. The quasi-static compression tests were obtained by using universal testing machine and high velocity compression tests were obtained by using the Split Hopkinson Pressure Bar test technique.

Even if the filament itself is isotropic, the manufactured parts via the FDM process are anisotropic because of the manufacturing method. Using this anisotropy and designing parts accordingly is important for the part's function. Manufacturing parameters affect the anisotropy of manufactured parts and therefore it is important to examine the production parameters when characterizing parts. Additionally, in this thesis, the most affecting process parameters are investigated which are layer height, build direction, the addition of short fibers into matrix, shape and size effect of specimens and contour number.

CHAPTER 3

MATERIALS AND TESTING

The specimen preparation methods and the details of the applied tests are explained in this part. Note that the final properties of the AM products depend on the printing parameters. All AM samples studied in the thesis were therefore prepared using the same printing parameters.

The test specimens were manufactured by using a Markforged Mark-Two 3D FDM printer. A picture of the used printer is shown in Figure 3.1 (KONICA MINOLTA n.d.). Mark-Two 3D printer uses a dual extruder nozzle system which is capable of manufacturing continuous fiber-reinforced polymer composites. One of these nozzles is used for printing matrix material and the other one is used for printing pre-impregnated continuous fiber reinforced polymers. The device uses Nylon 6 (Polyamide 6), Onyx (a short carbon fiber reinforced Nylon 6), carbon, kevlar, glass and high strength high temperature glass fibers for continuous reinforcement. The Nylon and Onyx filaments had a diameter of 1.75 mm. Both are stored in a sealed dry box before use in order to protect them from moisture. Parts' geometries were prepared in the CAD software and were transferred into Eiger slicer software in an STL file format. The Eiger slicer software is a tool used to select the infill percentage, infill type (rectangular, triangular, honeycomb and gyroid), material, continuous fiber content and orientation, raster orientation, build angle, number of contour layers and layer height and position on the build plate (Figure 3.2). In the sample preparation, the build plate was not heated during processing, so the specimens were printed at room temperature. While printing the filament either Nylon or Onyx, the raster angle cannot be adjustable in Eiger slicer software. The printer can print the structures only at a crisscross raster angle of [-45/+45]. But, by rotating the specimens in the program on the Z axis at 45 degrees, a cross-raster angle of [0/90] can be achieved as shown in Figure 3.3 (Hill and Haghi 2014). In any case, the Eiger slicer software can print successive layers by changing the printing angle on each layer up to 90 degrees from the previous layer. The comparison of mechanical properties of Nylon and Onyx filaments are tabulated in Table 3.1 (Group n.d.).

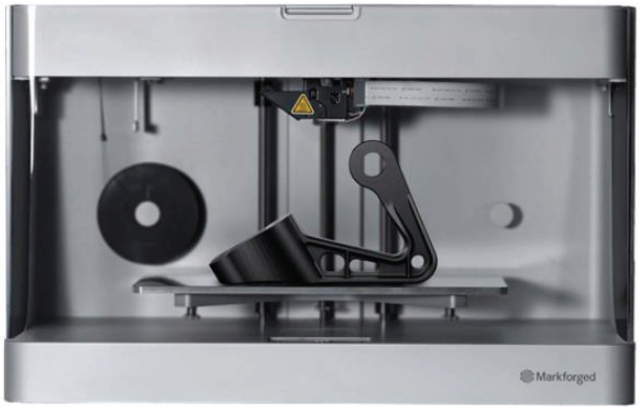

Figure 3.1. Markforged Mark-Two Printer
(Source: https://www.konicaminolta.com.au/products/3d-printers/composite-printing/mark-two)

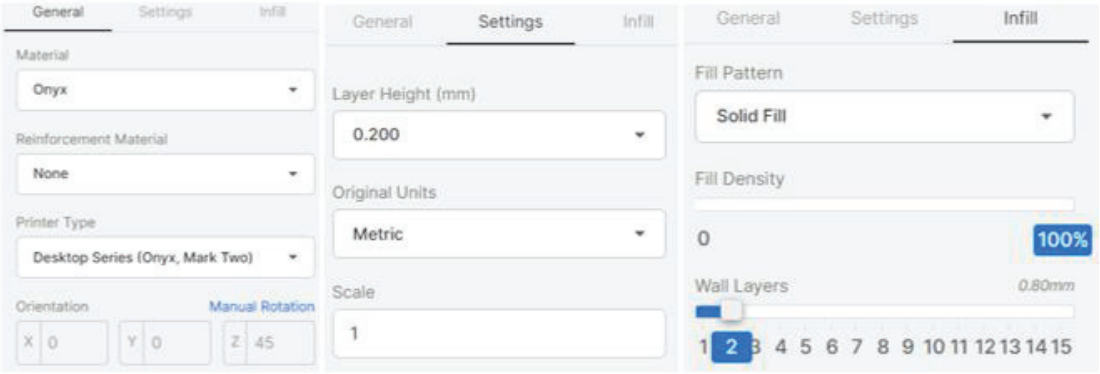

Figure 3.2. Eiger slicer sofware printing settings

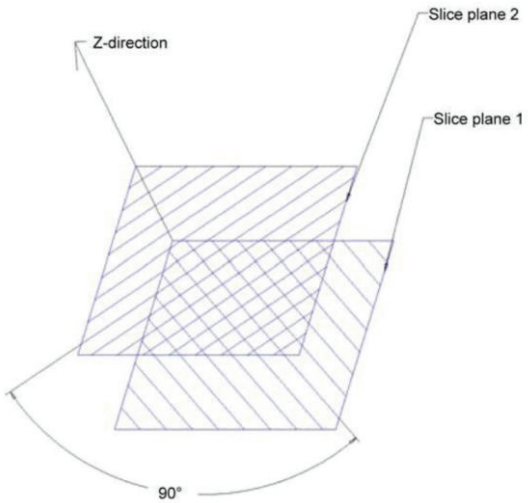

Figure 3.3. Perpendicular adjacent layers build orientation
(Source: Hill and Haghi et. al, 2014)

Table 3.1 The comparison on Onyx and Nylon materials
(Source: https://plmgroup.eu/articles/material-guide-markforged-onyx/)

Property	Onyx	Nylon
Tensile Strength (MPa)	36	54
Tensile Modulus (GPa)	1.4	0.94
Tensile Strain at Break (%)	58	260
Flexural Strength (MPa)	81	32
Flexural Modulus (GPa)	2.9	0.84
Heat Deflection (Celsius)	145	44-50
Density (g/cm^3)	1.18	1.10

3.1. Specimen Preparation for Mechanical Testing

Both nylon and onyx FDM specimens were produced using the process parameters. The list of the investigated specimen geometries is as follows (Figure 3.4).

1. The quasi-static and high strain rate compression Nylon test specimens were 10 mm in diameter and 13 mm in length (D10L13).
2. The quasistatic and high strain rate compression Onyx test specimens were 10 mm in diameter and 7 mm (D10L7), 10 mm (D10L10) and 13 mm (D10L13) in length.
3. The quasistatic and high strain rate compression cubic Onyx test specimens were 5mm (CUBE 5), 7 mm (CUBE 7) and 10 mm (CUBE10) in length.
4. 10 mm diameter and 10 mm long (D10L10) Onyx specimens were prepared with 0.1 mm and 0.2 mm layer height.
5. 10 mm in length cube (CUBE10) Onyx specimens were built in the orientations of 0, 30, 45, 60, 90 degrees (build angles) (Figure 3.5).
6. 10 mm in length cube (CUBE10) Onyx specimens were prepared in two different infill styles: [0/90] and concentric (Figure 3.6).

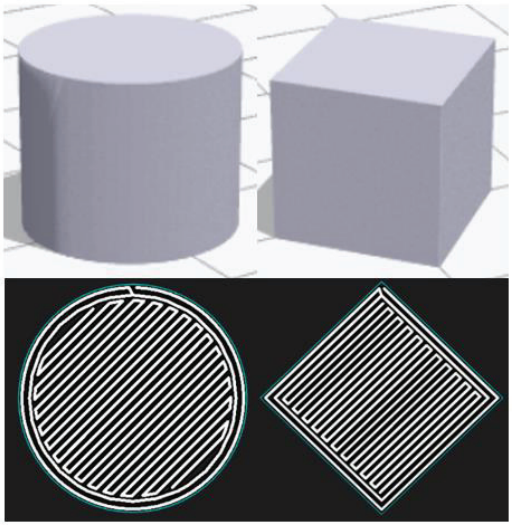

Figure 3.4. Cylinder (D10L10) and Cube (CUBE10) compression test specimens

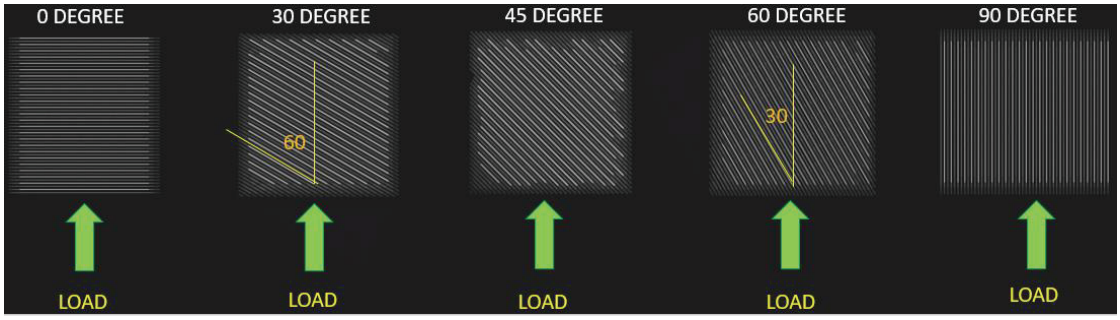

Figure 3.5. The build orientations in Onyx CUBE10 specimens

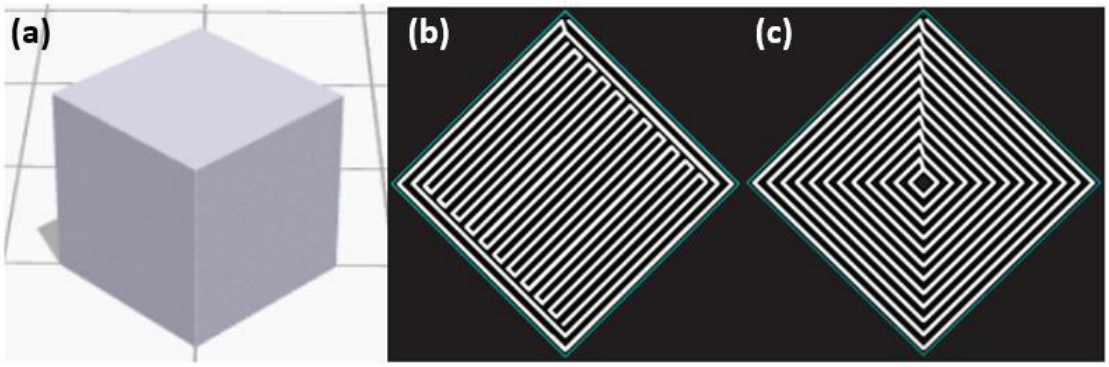

Figure 3.6. The view of each dimensions are 10 mm in length (CUBE10) compression test specimens (a) Perspective view, (b) [0/90] lay-up inside view, (c) Concentric lay-up inside view

3.1.1. Quasi-Static Compression Testing

The quasi-static compression tests were conducted in a 300 kN Shimadzu AG-X universal tension and compression test machine as shown in Figure 3.7. Quasi-static tests were performed at 10^{-3}, 10^{-2} and 10^{-1} 1/s. The engineering stress (σ_{eng}) and strain rate ($\dot{\varepsilon}_{eng}$) were calculated using the following relations

$$\sigma_s = \frac{P}{A_s} \tag{3.1}$$

$$\dot{\varepsilon}_{eng} = \frac{V_h}{L_s} \tag{3.2}$$

where P is the load and V_h is the cross-head speed of testing machine and A_s is the cross-section area and L_s is the length of the specimen.

Figure 3.7. The universal testing machine

The displacements of the specimen deformation were measured by using a video extensometer which calculated the distance between the gauge markers using a camera as shown in Figure 3.8 and by using the test machine stroke values.

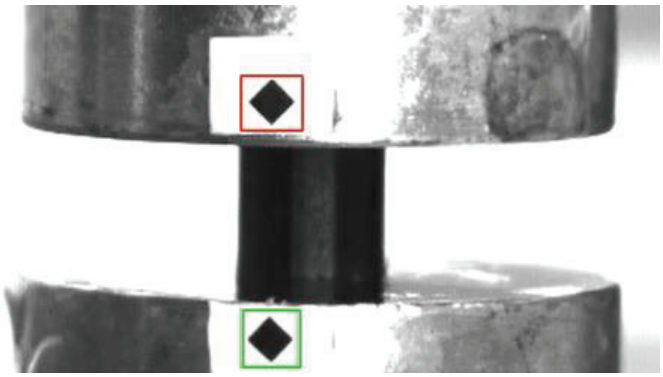

Figure 3.8. Quasi-static compression test of Onyx cylinder specimen

The compression test specimens were compressed until about 80% of their length. Additionally, jumping tests were applied to obtain strain rate sensitivity at the quasi-static strain rate regime. In these tests, the specimens were compressed at 10^{-3} 1/s until 15% strain and then compressed at 10^{-2} 1/s until 30% strain and finally compressed at 10^{-1} 1/s until larger strains. The tests were repeated three times for each group of specimens and the compression test platens were lubricated with a thin layer of grease to prevent friction between specimen and platens. The engineering stress and strain (ε_{eng}) were converted into true stress (σ_{tr}) and true strain (ε_{tr}) using the following relations,

$$\sigma_{tr} = \sigma_{eng}(1 - \varepsilon_{eng}) \tag{3.3}$$

$$\varepsilon_{tr} = -\ln(1 - \varepsilon_{eng}) \tag{3.4}$$

3.1.2. Dynamic Compression Testing

Dynamic tests were performed using a compression SHPB apparatus. The schematic representation of the SHPB testing method is shown in Figure 3.9. In the SHPB testing method, the specimen is sandwiched between the incident and transmitter bars.

The gas gun is filled with nitrogen. The striker bar is placed in front of the gas gun. By opening the output valve of the gas gun, the pressurized gas releases and pushes the striker bar. The striker bar is surrounded by a housing namely barrel to provide the pushed striker bar to move only in one direction. The barrel has small holes around it to release pressurized gas. The incident bar placed at the end of the barrel and pushed striker bar hits the incident bar which initiated compressive stress on the incident bar. The compressive stress wave at specimen and bar interfaces is reflected back in the incident bar as tension, and the part is transmitted through the transmitter bar as compression. The strain gages placed on the incident and reflected bar measure the strains on the bars. The used SHPB had Inconel 718 striker, incident and transmitter bar. The properties of bar material are as follows: elastic modulus=204 GPa, density=8200 kg/m^3 and yield strength= ~700 MPa. The striker, incident bar and transmitter bar had equal diameter, 19.4 mm. The lengths of the striker, incident and transmitted bars were 500, 2000 mm and 1800 mm, respectively. The gas gun was pressurized until 8 bar.

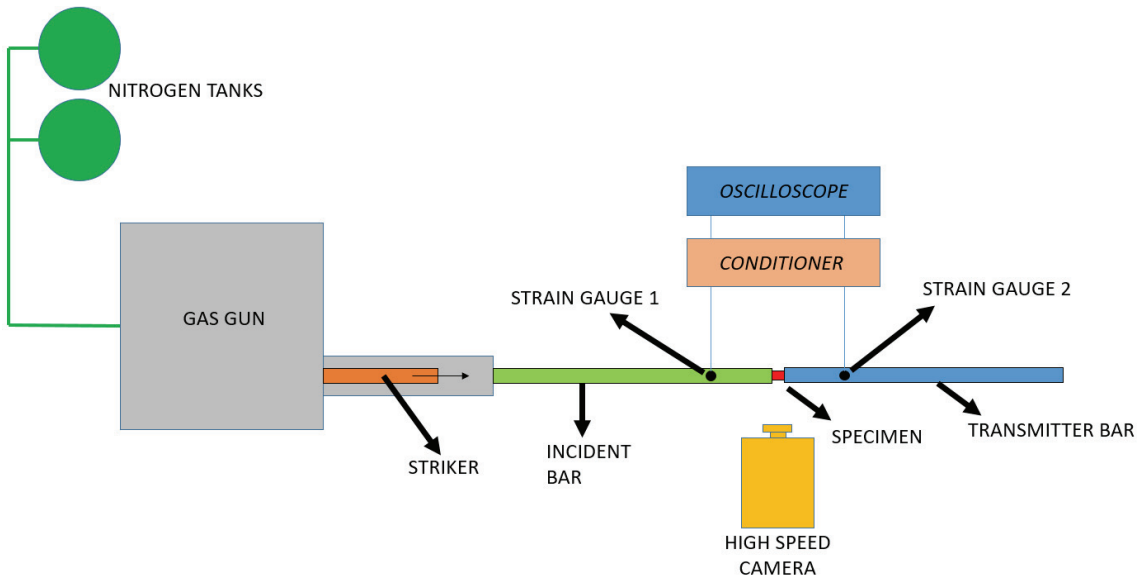

Figure 3.9. The Split Hopkinson Pressure Bar compression test setup

The strain (ε_s), stress (σ_s) and strain rate ($\dot{\varepsilon}_s$) of the specimen were obtained sequentially from Equations 3.5, 3.6 and 3.7.

$$\varepsilon_s(t) = -\frac{2C_b}{L_s}\int_0^t \varepsilon_R(t)dt \tag{3.5}$$

$$\sigma_s(t) = \frac{A_b}{A_s} E_b \varepsilon_T(t) \tag{3.6}$$

$$\dot{\varepsilon}_s(t) = -\frac{2C_b}{L_s} \varepsilon_R(t) \tag{3.7}$$

where L_s, A_b, A_s, E_b, C_b and t are the length of the specimen, the cross-sectional area of bar and specimen, elastic modulus and wave velocity of bar and time, respectively. ε_R and ε_T are sequentially the reflected and transmitted strains. A thin layer of grease is applied as a lubricant between specimen and bar interfaces to reduce friction. A raw datum of a test is shown in Figure 3.10. The blue line is obtained from strain gauge 1 which is mounted on the incident bar and the red line is obtained from strain gauge 2 which is mounted on the transmitter bar.

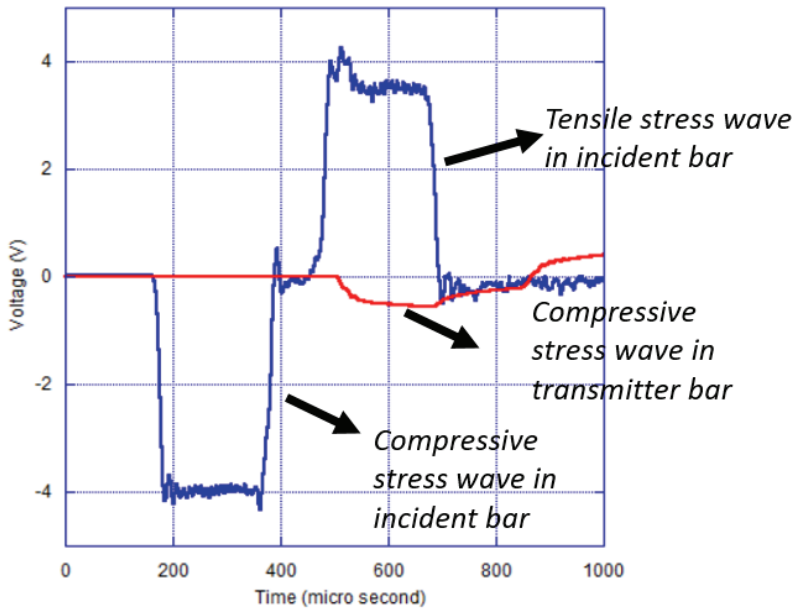

Figure 3.10. The raw data of Onyx-D10L10 obtained from SHPB test

The strain rate sensitivity (m) in strain rate jump tests was calculated as

$$m = \frac{\log\left(\frac{\sigma_2}{\sigma_1}\right)}{\log\left(\frac{\dot{\varepsilon}_2}{\dot{\varepsilon}_1}\right)} \tag{3.8}$$

The subscript 1 defines the stress and strain rate before jump and 2 defines the after jump.

3.1.3. Density Tests

The density of specimens was determined by following the ASTM-D792-20 Standard Test Methods for Density and Specific Gravity (Relative Density) of Plastics by Displacement. The density of specimens was calculated using the following equations,

$$V_{coupon} = \frac{W_{coupon} - W_{submerged}}{\rho_{water}} \tag{3.9}$$

$$\rho_{coupon} = \frac{W_{coupon}}{V_{coupon}} \tag{3.10}$$

Where V_{coupon} is the volume of the specimen, W_{coupon} is the specimen weight in air and $W_{submerged}$ is the weight in distilled water. The density measurements of specimens were further compared with the density of filaments in order to find the void volume fraction.

3.1.4. Pyrolysis Test

In order to determine the percentage of short carbon fibers inside the nylon matrix, a pyrolysis test was performed on the Onyx D10L10 compression test samples. The pyrolysis test was applied in accordance with ASTM-D3171-99 Standard Test Methods for Constituent Content of Composite Materials Procedure G. The test samples were dried in a muffle furnace at 100°C in order to remove the moisture. Then the specimens were weighted. The weight of fibers was then determined after removing the matrix material by burning it in a muffle furnace at 550°C for 1.5 hours.

3.1.5. Microscope Analysis

The fiber fraction, distribution and alignment were also microscopically investigated. For that, the compression test specimens were cut through vertically and horizontally as shown Figure 3.11 (a) and (b). The microscopic observations were made in a stereomicroscope at 1x, 3x and 5x and in an optical microscope at 50x magnifications.

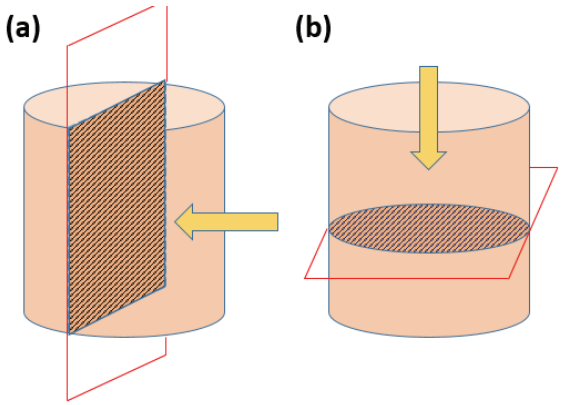

Figure 3.11. The cutting planes of specimens (a) vertically and (b) horizontally cutted specimens

In this study, the number of contours were selected two, because the first contour on the inside ensured good compatibility with raster ends, and the second contour on the outside ensured good bonding with the first contour and a good surface quality of the part. Also, the number of contours was tried to be minimum as this research focused on the infill, raster and build direction's effect. The cross raster angle of [0/90] pre-print and produced part images are shown in Figure 3.12 (a) and (b), respectively.

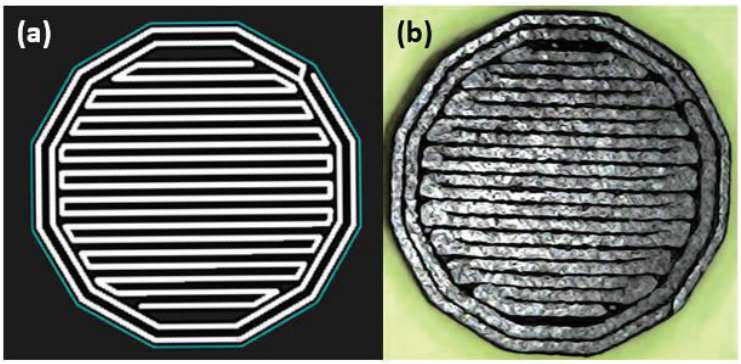

Figure 3.12. Short carbon fiber reinforced nylon (a) Pre-print image in slicer software and (b) Produced part's image

CHAPTER 4

RESULTS AND DISCUSSION

4.1. Microscope Analysis Results

The isotropic infill section in the middle of a specimen (1) and the concentric rings at the outer surface of the specimen (2) are shown in Figure 4.1. The printing is started at the concentric rings, after two concentric rings are printed, the isotropic infill is printed. The start and end points of the deposition are marked with yellow circles at the rings and the interface between the isotropic infill and concentric rings is marked with a red dashed line in Figure 4.1.

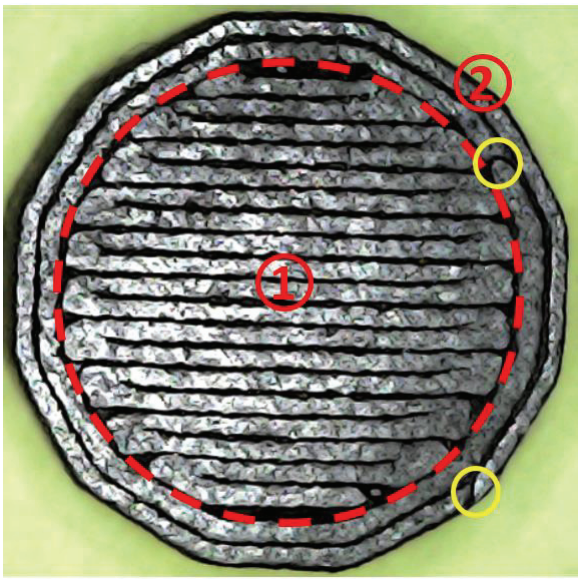

Figure 4.1. The picture of an Onyx cylinder specimen (D10L10): (1) isotropic infill region and (2) concentric rings at the outer surface

The stereo microscope images of a horizontally-cut Onyx cylinder specimen (D10L10) from different locations are shown in Figure 4.2(a-d). The images are taken at different regions of the horizontally-cut specimen shown in Figure 4.2(a). Because of two different deposition strategies, the fiber orientation becomes random at the interface

between isotropic infill and concentric rings as seen in Figure 4.2(b). The fibers are oriented radially in the concentric ring section at the outer surface (Figure 4.2(c)), while the fibers are mostly oriented in the deposition direction in the isotropic infill section (Figure 4.2(d)). It is also seen in the same figures that the interlayer bonding between the layers is weaker in the middle as compared with that at the edge of the specimen.

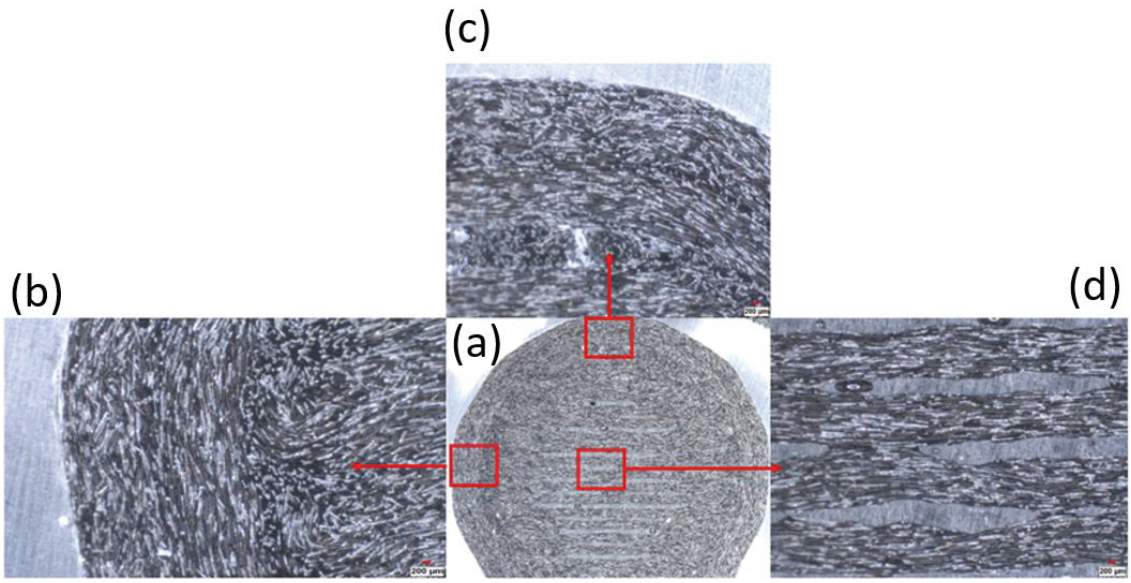

Figure 4.2. The stereo microscope images of horizontally cut Onyx cylinder specimen (D10L10), (a) specimen, (b) isotropic infill and concentric rings, (c) concentric ring section at the outer surface and (d) the isotropic infill section

The stereo microscope images of a vertically-cut Onyx cylindrical (D10L10) specimen deposited with 0.1 mm layer height are shown in Figure 4.3(a-c). The stereo microscopy image shows with 1X magnification in Figure 4.3(a) and 5X magnification at the middle of the specimen in Figure 4.3(b) and near the outer surface in Figure 4.3(c). The cutting plane in this image is parallel to the first layer deposition direction. Because the infill pattern of the specimen is cross raster angle of [0/90] orientation and the cutting plane is parallel to 0 direction, the fibers are seen as lines in one layer and as dots in another layer.

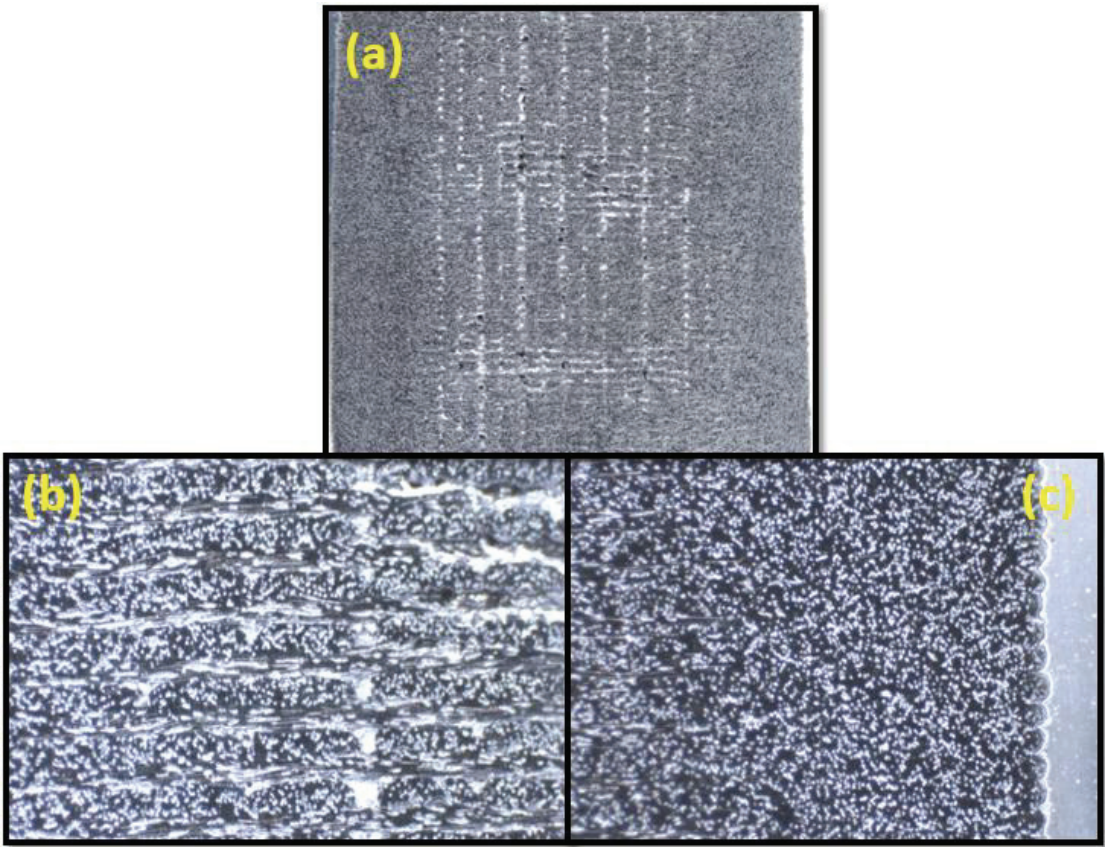

Figure 4.3. Stereo microscopy images of Onyx-D10L10-0.1LH with (a) 1X magnification and 5X magnification of (b) middle of specimen and (c) outer surface of specimen.

Figure 4.4(a-c) show the stereo and optical microscope micrographs of a vertically cut 0.2 mm layer height Onyx cylinder (D10L10) specimen at different magnifications. In these microscopy images, the layers and fiber orientations can be easily differentiated. At the lowest magnification, the voids are concentrated at the middle region of the specimen as seen in Figure 4.4(a). The 0^o and 90^o infill pattern layers are clearly seen in Figures 4.4(b) and 4.4(c). The layers with 0 orientation are parallel to the plane and observed as lines and the layers with a 90 orientation are perpendicular to the cutting plane and observed as points. The stereo microscope images of vertically cut 0.1 mm and 0.2 mm layer height specimens shown in Figure 4.3(a) and Figure 4.4(a) indicate that the voids inside the geometry are not homogeneously distributed; they are collected in the middle regions of specimens. By comparison, the void size and amount are greater in the 0.2 mm layer height specimen than in the 0.1 mm layer height specimen.

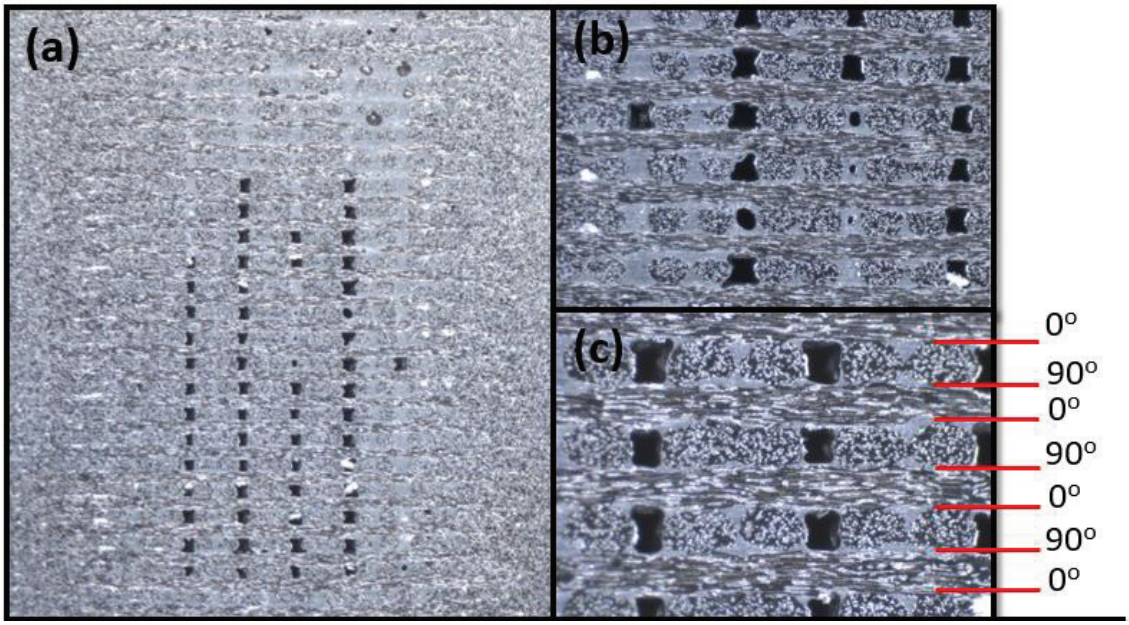

Figure 4.4. The stereo microscope images of vertically cut Onyx D10L10 – 0.2 Layer height specimen at (a) 1x, (b) 3x and (c) 5x magnifications

The post-test images of the 10 mm cube Onyx specimen (CUBE10), which was tested at dynamic strain rates in the Split-Hopkinson Pressure Bar test equipment and produced at a 90-degree angle, are shown in Figure 4.5. The specimen is embedded into a resin (a) and images are taken in an optical microscope with 50x (b, d, e) and 200x (c) magnifications. According to the figure the delamination between layers can be seen in Figure 4.5 (b, d) easily. Additionally, in Figure 4.5 (c) it is observed that some of the fibers were fractured. And in Figure 4.5 (e) the failure was evaluated as ductile behavior which leads to a matrix failure.

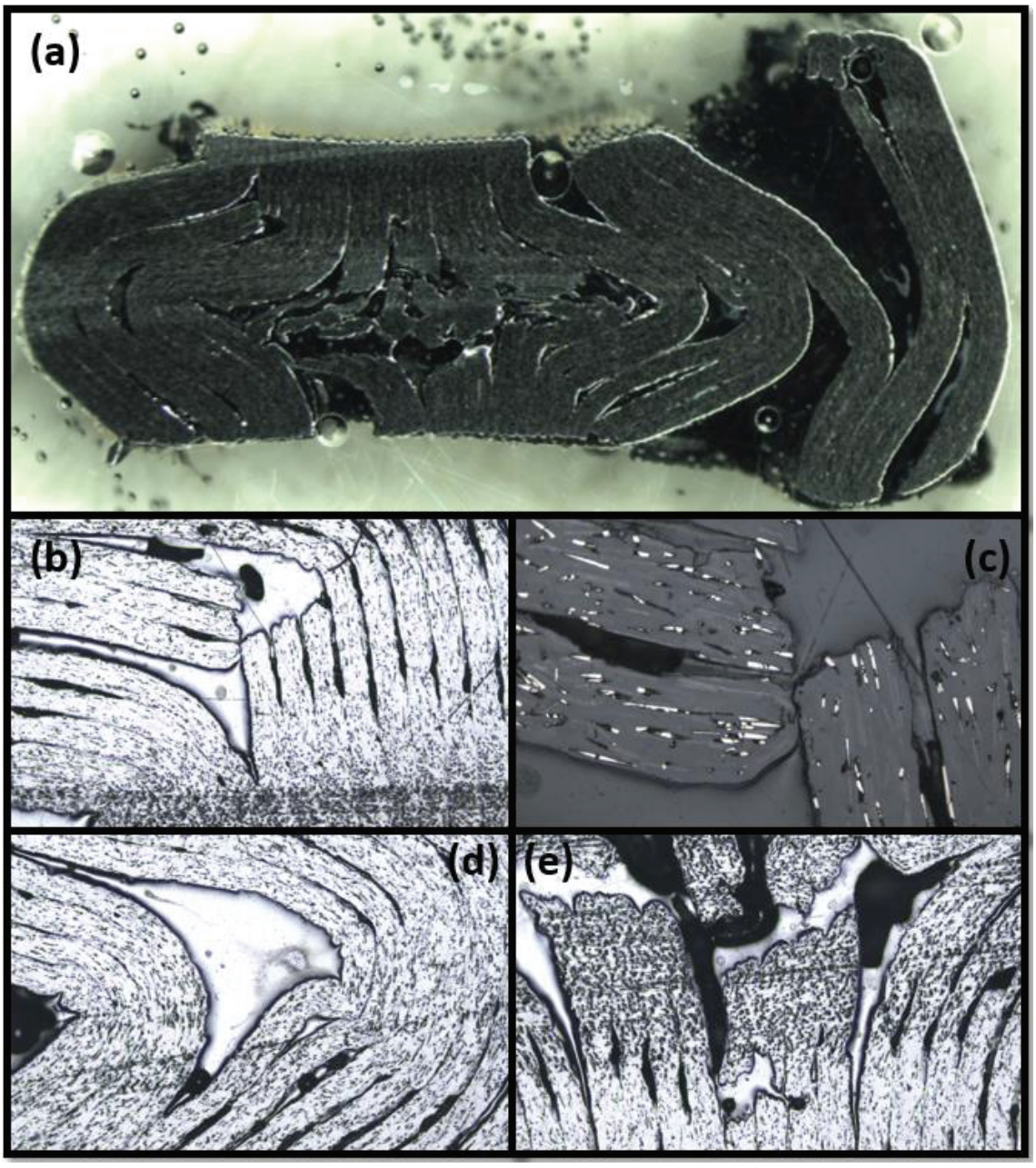

Figure 4.5. The Onyx CUBE10-90 Degree specimen tested at dynamic strain rate, (a) the embedded specimen in resin, optical microscope images (b) delamination and rupture, (c) fiber fracture, (d) delamination and (e) matrix failure

4.2. Pyrolysis Test Results

The pyrolysis test results are tabulated in Table 4.1. From these tests, the average weight percentage of short carbon was determined 12.46 %, which is in accord with other studies in the literature which is summarized in Table 2.4.

Table 4.1. The pyrolysis test results

ONYX	Total Weight (g)	Carbon Fiber Weight (g)	Matrix Weight (g)	Carbon Fiber Weight Percentage (%)
D10L10-0.1 LH-T1	0.8238	0.1082	0.7156	13.134
D10L10-0.1 LH-T2	0.8324	0.1053	0.7271	12.650
D10L10-0.1 LH-T3	0.8261	0.1009	0.7252	12.214
D10L10-0.2 LH-T1	0.7831	0.0976	0.6855	12.463
D10L10-0.2 LH-T2	0.7893	0.0915	0.6978	11.593
D10L10-0.2 LH-T3	0.7902	0.1003	0.6899	12.693

4.3. Compression Test Results

The true compression stress-strain curves of PA6 and Onyx D10L13-0.1 LH specimens at 0.001, 0.01, 0.1 and 1100 1/s are sequentially shown in Figure 4.6 (a-d). Three tests performed at each strain rate are seen in the same curves and are nearly repeatable. Also, increasing strain rate increases the flow stress of both PA6 and Onyx specimens. The inclusion of short carbon fibers increases both the flow stress and elastic modulus of Polyamide 6. The yield stress and elastic modulus were determined by 0.2% of offset methods and linear fit to the initial region of stress-strain curves as shown in Figure 4.6(e). The elastic modulus and yield stress values are compared in Figure 4.6(f) with respect to strain rate. It is seen that the short carbon fiber addition increases the elastic modulus of neat Polyamide 6 around 4-5 times and yield stress around 3-4 times.

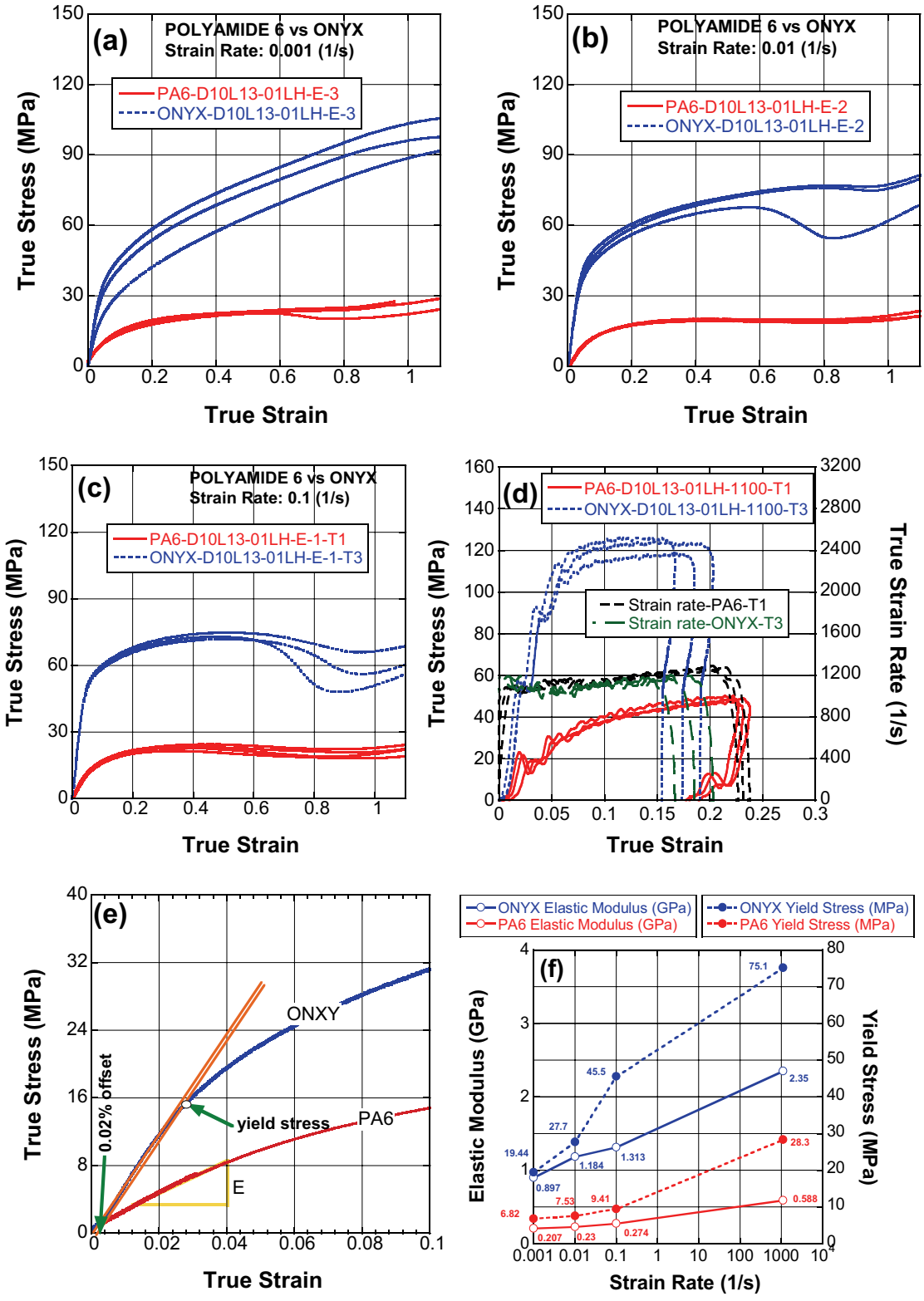

Figure 4.6. The stress and strain curves of PA6 and Onyx D10L13-0.1 LH at (a) 0.001 1/s, (b) 0.01 1/s, (c) 0.1 1/s and (d) 1100 1/s, (e) determination of yield stress and elastic modulus and (f) Elastic modulus and yield stress with respect to strain rate

Although the addition of short carbon fibers inside the Polyamide 6 matrix increases the elastic modulus and yield stress of the specimen, it induces a more brittle behavior. The undeformed and compressed specimens of Polyamide 6 and Onyx are shown in Figure 4.7(a-b), respectively. As is seen in the same figures, the recovery of Polyamide 6 after the test is larger and Onyx specimens exhibit shear types cracks after the tests.

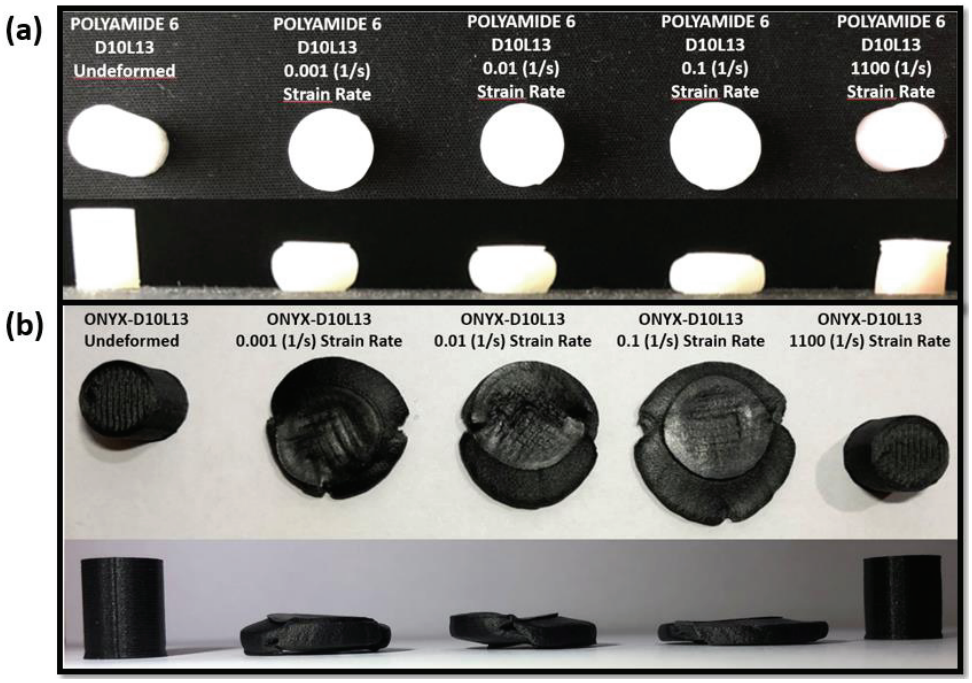

Figure 4.7. The undeformed and compressed specimens of (a) Polyamide 6 D10L13 and (b) Onyx D10L13 specimens

The true stress-strain curves of PA6 and Onyx specimens produced with 0.1 mm and 0.2 mm layer heights at different strain rates are shown in Figure 4.8(a-d) and Figure 4.9(a-d), respectively. PA6 specimens were 10 mm in diameter and 13 mm in length, and Onyx specimens were 10 mm in diameter and 10 mm in length. At all strain rates, PA6 specimens with 0.2 mm height exhibit higher flow stresses than those of 0.1 mm height specimens as seen in Figure 4.8(a-d). The main reason for this difference is that a better layer diffusion is obtained in 0.2 mm layer height than in 0.1 mm layer height. A decrease in layer height increases the number of layers which can result in more void formation between each layer. Just an opposite effect of layer height on the flow stresses is seen in Onyx specimens. The specimens with 0.2 mm height show lower flow stresses than those of 0.1 mm height specimens at all strain rates (Figure 4.9(a-d)).

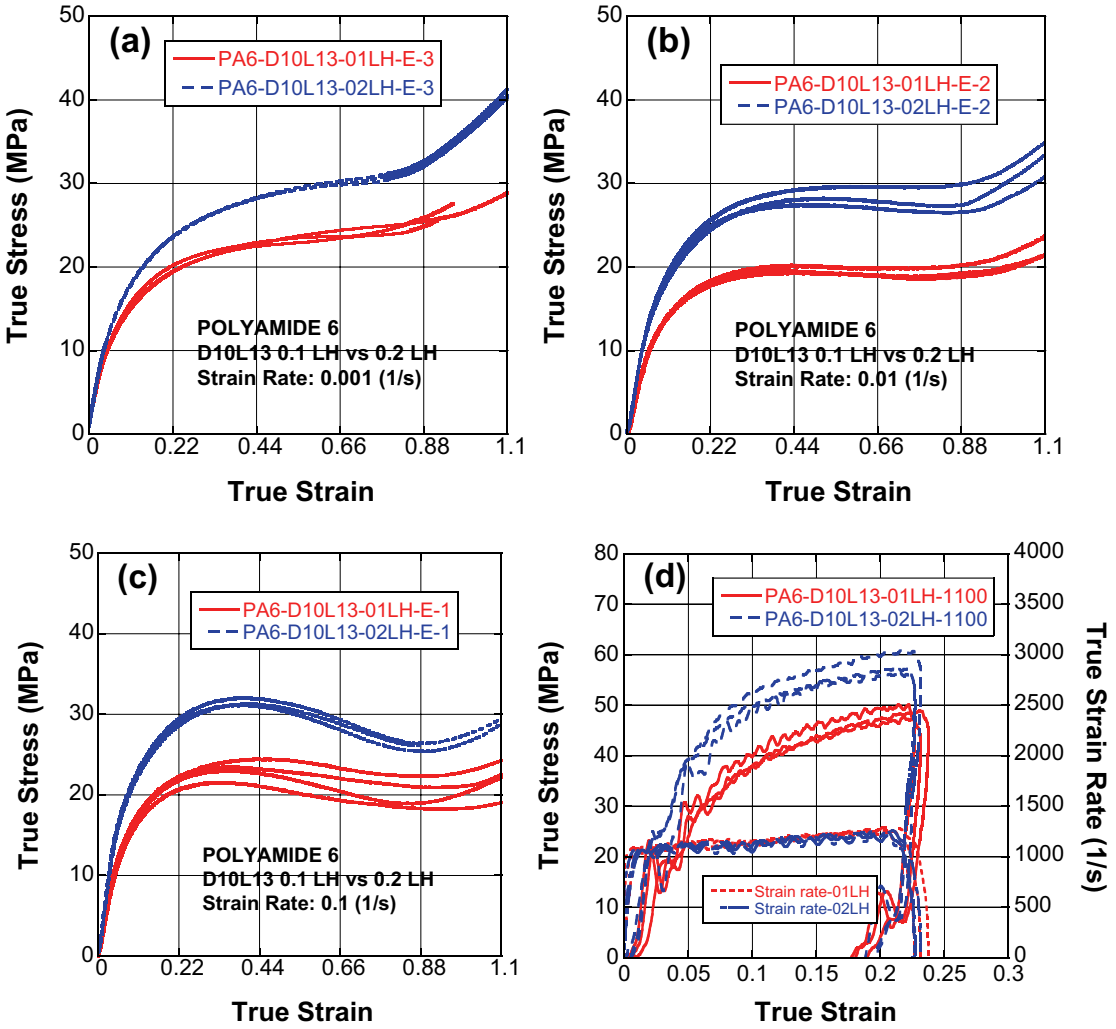

Figure 4.8. The stress and strain curves of PA6 D10L13 produced with 0.1 mm and 0.2 mm layer heights at (a) 0.001 1/s, (b) 0.01 1/s, (c) 0.1 1/s and (d) 1100 1/s

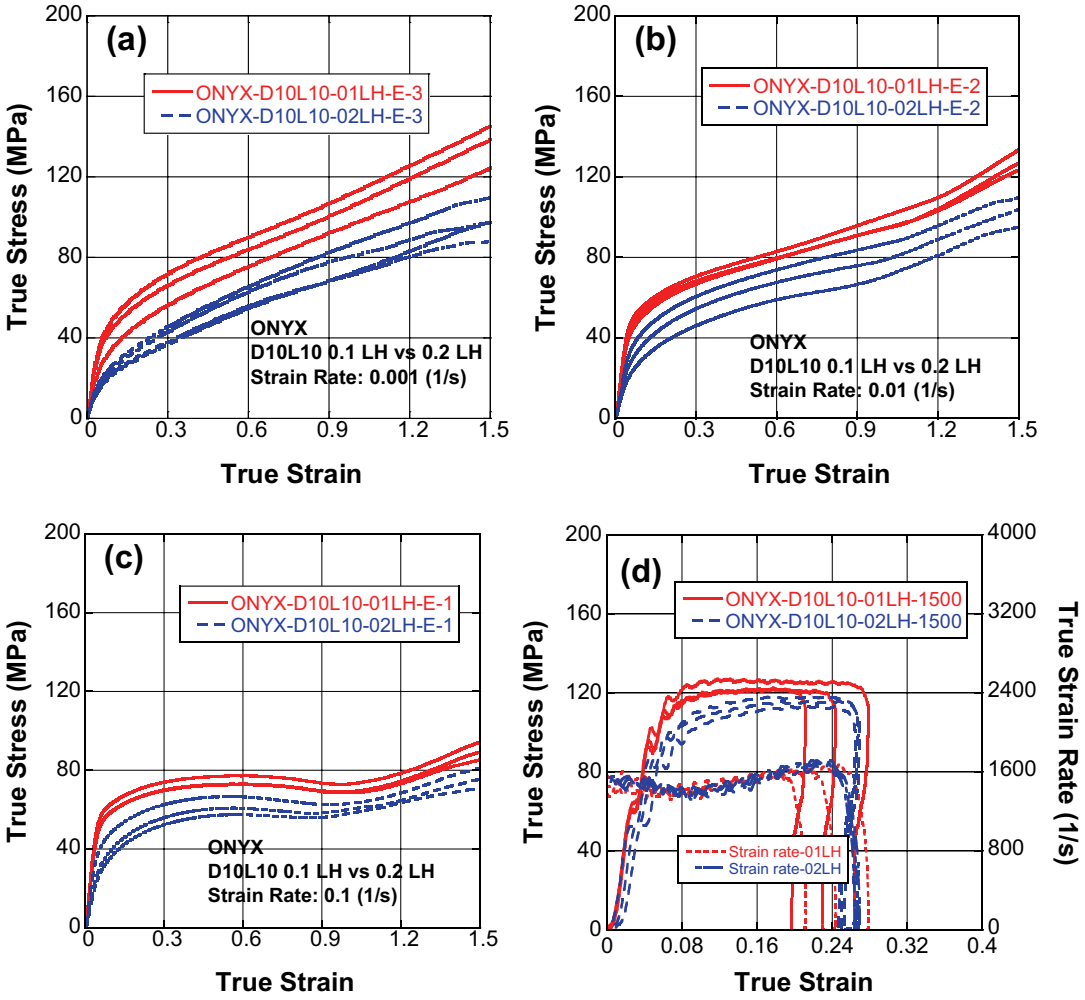

Figure 4.9. The stress and strain curves of Onyx D10L10 produced with 0.1 mm and 0.2 mm layer heights at at (a) 0.001 1/s, (b) 0.01 1/s, (c) 0.1 1/s and (d) 1500 1/s

The representative compression stress-strain curves of 0.1 mm and 0.2 mm height PA6 D10L13 and Onyx D10L10 specimens at quasi-static strain rates and at 1100 and 1500 1/s are shown in Figure 4.10(a-d), respectively. Until about 0.3 strain, the stress values increase as the strain rate increases at the quasi-static strain rate regime as seen in the same figures. Figure 4.10(a) and (b) show the variation of elastic modulus and yield strength with strain rate for 0.1 mm and 0.2 mm height D10L13 specimens, respectively. As the strain rate increases, both elastic modulus and yield strength increase. These figures show how the mechanical properties of each specimen change with increasing strain rates

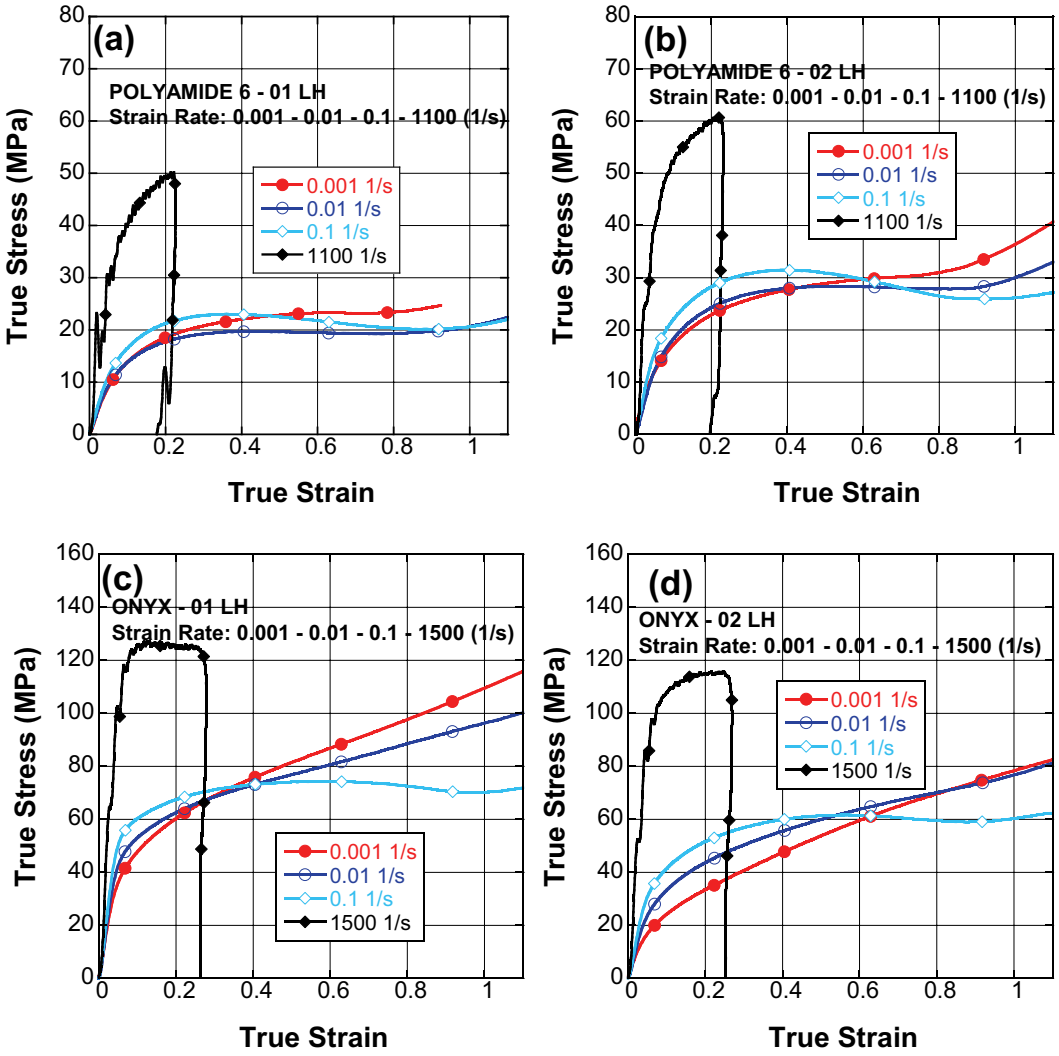

Figure 4.10. The stress and strain curves at different strain rates of (a) PA6 – D10L13 with 0.1 mm layer height, (b) PA6 – D10L13 with 0.2 mm layer height, (c) Onyx D10L10 with 0.1 mm layer height and (d) Onyx D10L10 with 0.2 mm layer height.

Figure 4.11(a) and (b) illustrate the applied strain rate jump test stress-strain curves of D10L13 PA6 0.1 mm height and Onyx 0.2 mm height specimens together with those of monotonic stress-strain curves, respectively. It is seen in the same curves monotonic strain rate and jump tests show a good correlation between each other. From these jump tests, the strain rate sensitivity parameter, m, using Eqn. 3.8 was determined 0.08 for PA6 and 0.125 for Onyx. The strain rate sensitivity of neat PA6 was also investigated by Vidakis et. al. and found nearly zero (Vidakis et al. 2020) (see Figure 2.49). This also confirms that the composite has higher strain rate sensitivity than the neat matrix.

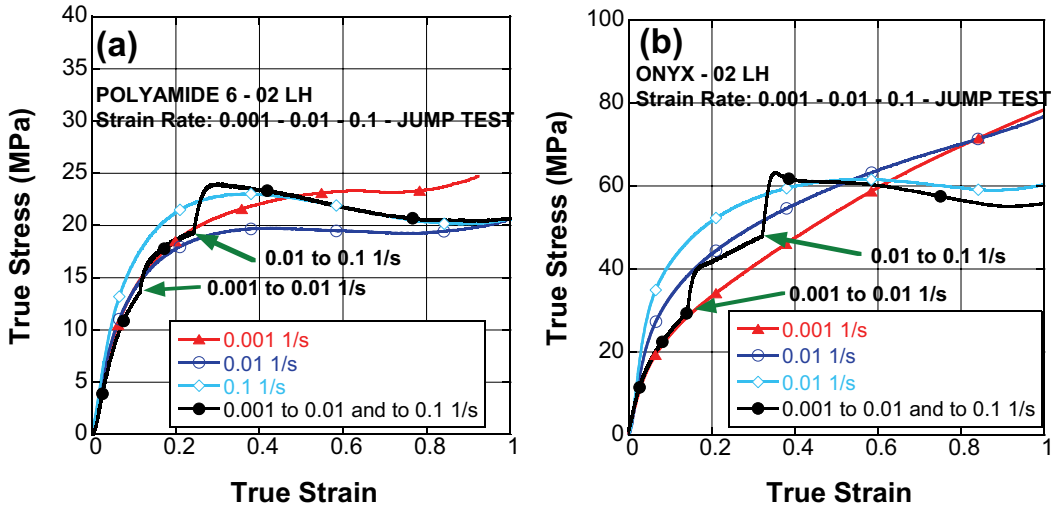

Figure 4.11. The comparison of compression tests different strain rates with jump tests for (a) PA6 – D10L13 – 0.1 mm layer height and (b) Onyx – D10L10 – 0.2 mm layer height.

4.3.1. The Comparison of Different Geometries

Figure 4.12(a-d) shows the representative stress-strain curves of D10L10 and 10x10 mm cubic Onyx specimens processed with 0.2 mm layer height, zero build angle and cross raster angle of [0/90] at 0.001, 0.01, 0.1 and 1500 1/s, respectively. In the uniaxial compression tests at quasi-static strain rates, cylindrical and cubic specimens show similar stress-strain behavior, while at increasing strains the cube samples present lower stress values except for the tests performed at 0.001 1/s. At dynamic strain rates, the cylindrical specimens show higher stresses at all strains as depicted in Figure 4.12(d).

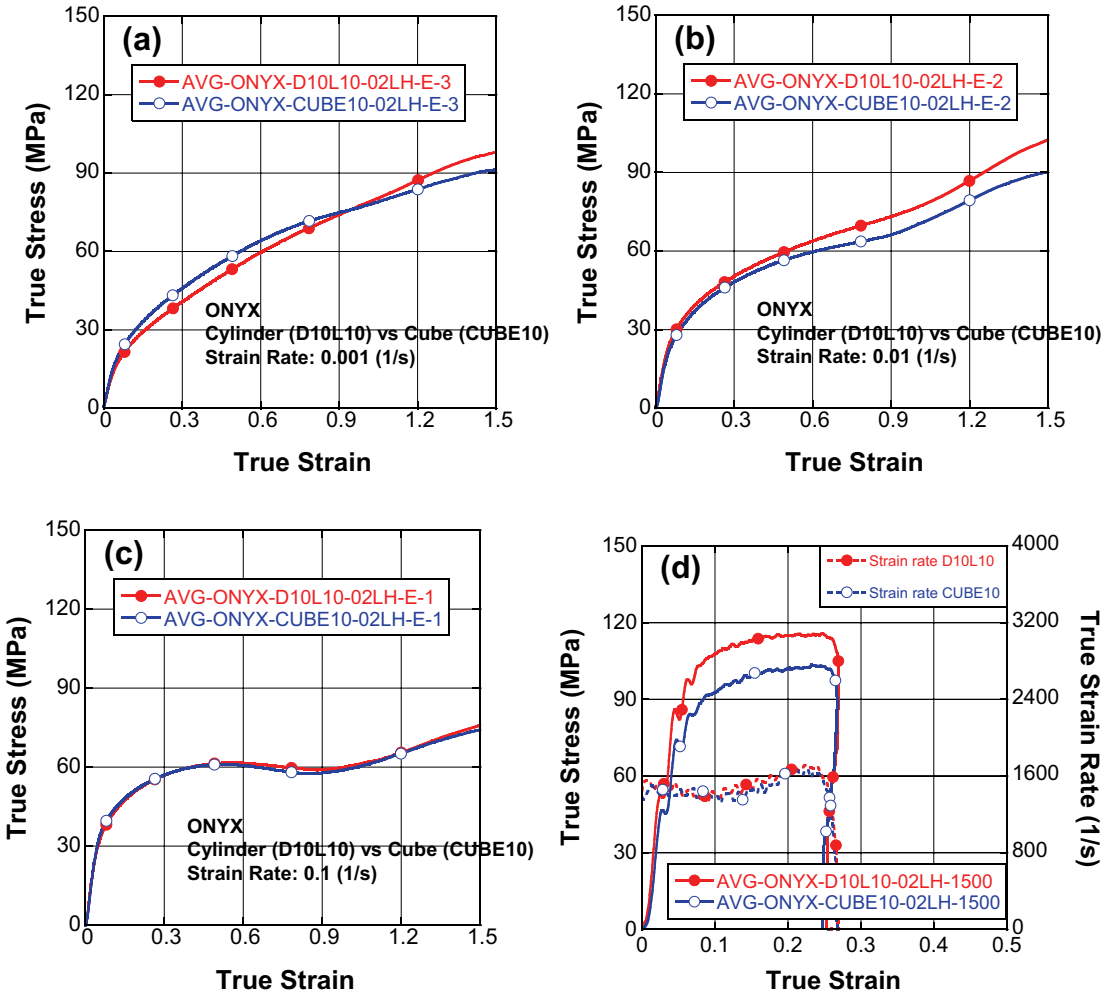

Figure 4.12. The comparison of stress and strain curves of cylinder (D10L10) and cube (CUBE10) geometries under compression tests at different strain rates of (a) 0.001 1/s, (b) 0.01 1/s, (c) 0.1 1/s and (d) 1500 1/s.

4.3.2. The Specimen Shape and Dimensions Effect On The Compressive Behavior

The average stress-strain curves of 7, 10 and 13 mm-long 10 mm-diameter (D10L7, D10L10, D10L13) cylindrical specimens, all having a 0.1 mm layer height are shown in Figure 4.13(a-d) at 0.001, 0.01 and 0.1 1/s and at a dynamic strain rate, respectively. At 0.001 and 0.01 1/s strain rates (Figure 4.13(a) and (b)), the flow stresses of 10 mm-long specimens are higher than those of 7 and 13 mm-long specimens and 13 mm-long specimens have higher flow stresses than 7 mm-long specimens until about 0.5 strain. At 0.1 1/s, as seen in Figure 4.13(c), the stresses of 10 and 13 mm-long specimens

however become very much similar until about 0.5 strain. At increasing strains above 0.5 strain, the flow stresses of 7 mm-long specimens become higher than those of 10 and 13 mm specimens at the studied quasi-static strain rates. At the dynamic strain rate, as seen in Figure 4.13(d), the flow stresses of 7 mm-long specimens are higher than those of 10 and 13 mm-long specimens, while 13 mm-long specimens have slightly higher flow stresses than 10 mm-long specimens. As noted in Figure 4.13(d), as the length of the specimen decreases, the strain rate increases due to a constant 8 bar SHPB gas pressure was used in the tests. Since the incident stresses are the same in all SHPB, the strain rate increases from 1100 1/s in 13 mm-long specimens to 1500 1/s in 10 mm-long specimens and 2400 1/s in 7 mm-long specimens (Figure 4.13(d)). The higher flow stress of the 7 mm long specimen at the dynamic strain rate is due to the fact that the strain rate in these specimens is higher on average as compared with 10 mm-long and 13 mm-long specimens.

The slenderness ratios (L/D) of the D10L7 specimen is 0.7, the D10L10 specimen is 1 and the D10L13 specimen is 1.3. The effect of slenderness ratios was previously investigated by Pankow et. al. and as the slenderness ratio decreased, the flow stress decreased slightly. A similar result was found in the present study. The pictures of the undeformed and compression tested Onyx D10L7, D10L10 and D10L13 specimens are shown in Figure 4.14(a-c). No damage is observed on D10L10 and D10L13 specimens, as these samples were deformed until about low strains, while cracks are seen on the D10L7 specimen. The weakest points of the parts produced by FDM are the bonding between layers and the failure is mostly observed in these regions as shown in Figure 4.15(a) and (b). The failure occurs at the bonding interface at the start and end points of the two concentric rings on the outer surface as marked with red dashed circles.

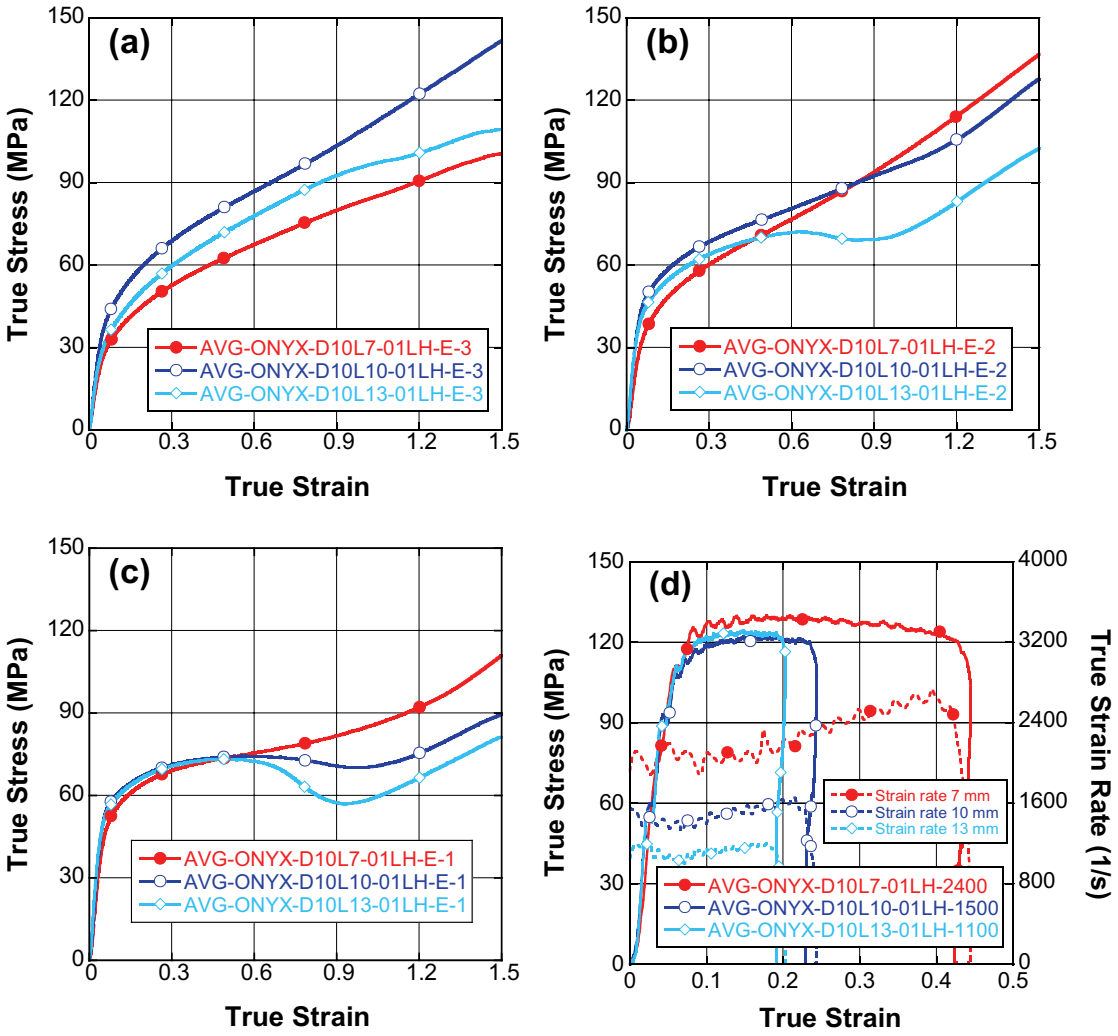

Figure 4.13. The average true stress-strain curves of cylinder D10L7, D10L10 and D10L13 specimens at (a) 0.001 1/s, (b) 0.01 1/s, (b) 0.1 1/s and (d) dynamic strain rate.

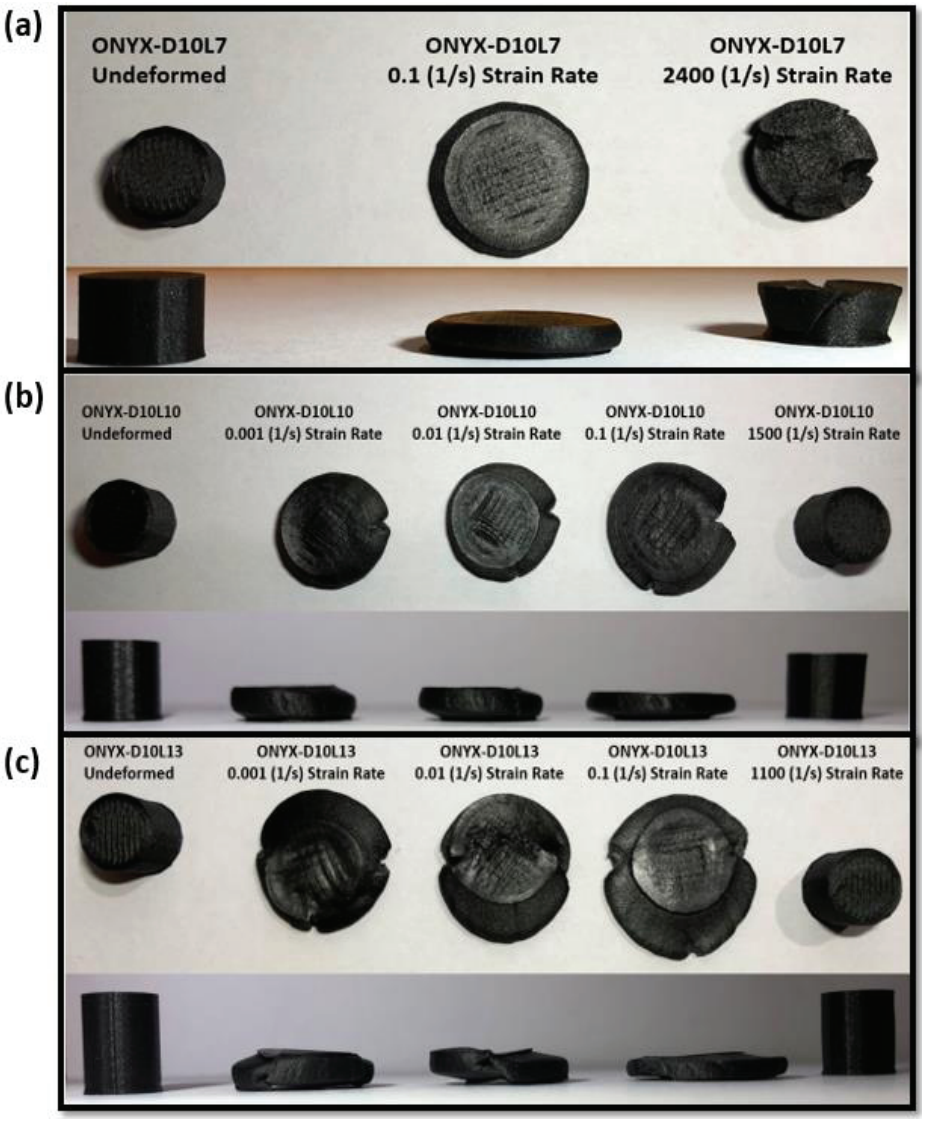

Figure 4.14. Undeformed and compression tested Onyx specimens (a) D10L7, (b) D10L10 and (c) D10L13.

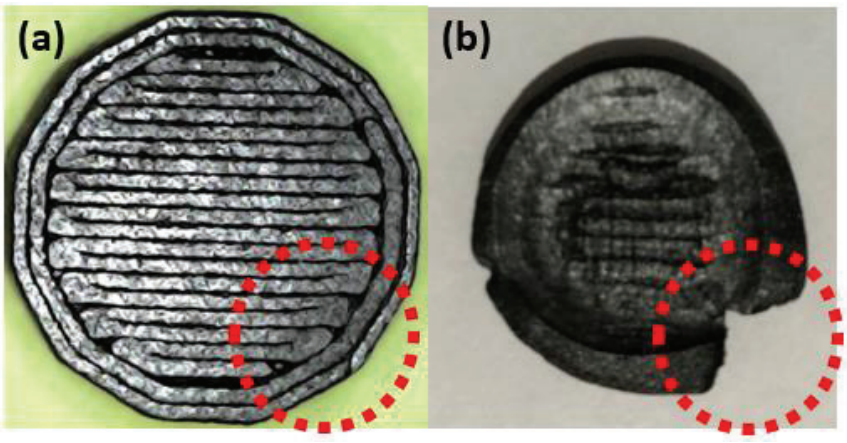

Figure 4.15. The failure region of compressed Onyx cylinder specimen at quasi-static strain rates (a) before test and (b) after test

The average stress-strain curves of 5, 7 and 10 mm (CUBE5, CUBE7, CUBE10) cubic specimens, all having a 0.2 mm layer height are shown in Figure 4.16(a-d) at 0.001, 0.01 and 0.1 1/s and at a dynamic strain rate, respectively. As seen in Figure 4.16(a-d), until about low strains, 0.3, all cubic specimens of 5, 7 and 10 mm-long yield similar flow stresses. After 0.3-0.6 strains, longer specimens exhibit low flow stresses. This may also be due to the deceased frictional forces in longer specimens. At the highest strain rate, in the SHPB tests, 5 mm-long specimens show the highest stresses as the strain rate is highest in these specimens (~4000 1/s). Although the strain rate is higher in the 7 mm-long specimens than in the 10 mm-long specimens, 10 mm-long specimens show higher stresses than 7 mm-long specimens.

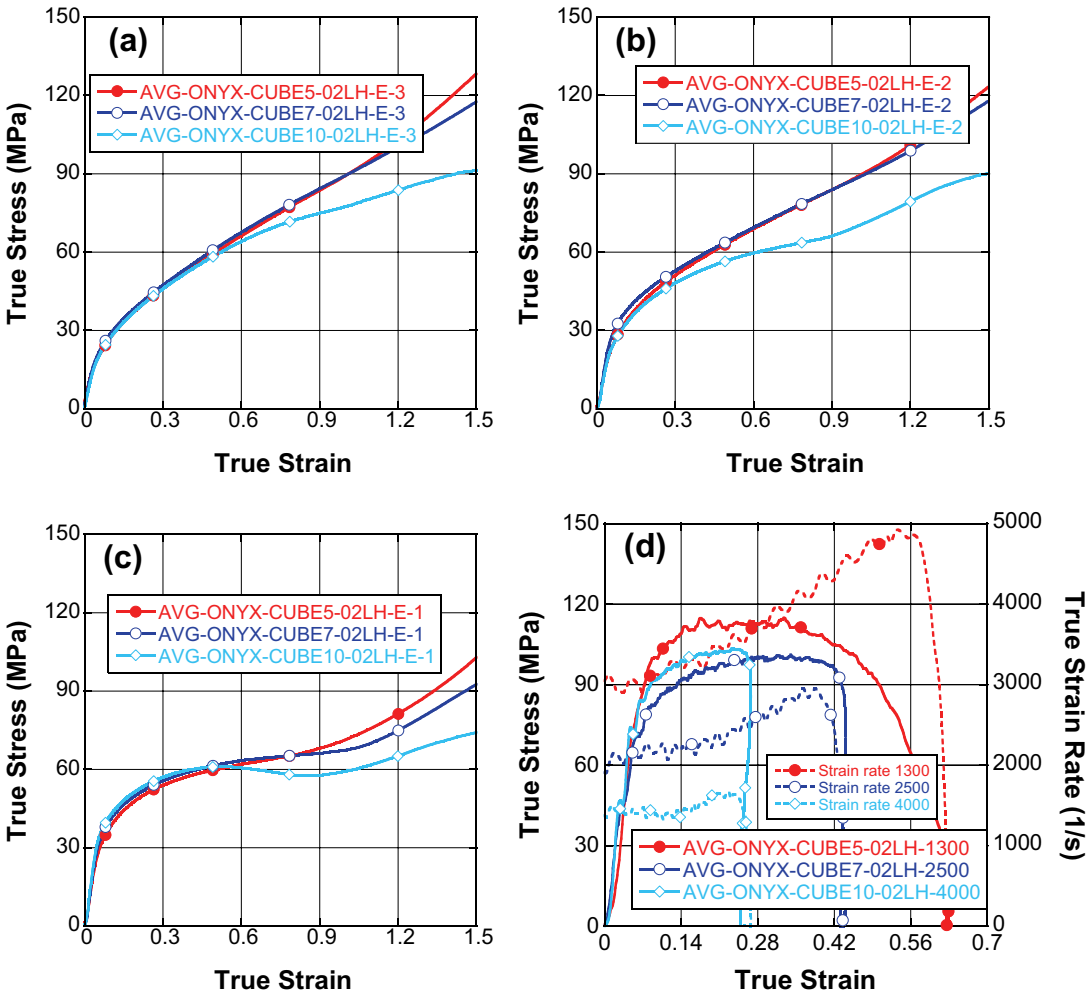

Figure 4.16. The average true stress-strain curves of cubic specimens at (a) 0.001 1/s, (b) 0.01 1/s, and (b) 0.1 1/s and (d) dynamic strain rate.

4.3.2.1. Density Measurements

The void fraction measurement results of PA6 and Onyx specimens with 0.1 and 0.2 mm layer height are tabulated in Table 4.2 and Table 4.3, respectively. PA6 specimens with 0.1 mm height have an average void content of 6%, while 0.2 mm height specimens have 5%. On the other side, Onyx specimens with 0.1 mm height have an average void content of 8.18% and 0.2 mm layer height specimens 13.66%. According to Table 4.2. Pristine PA6 is denser when it is produced with 0.2 mm height than produced with 0.1 mm height and according to Table 4.3, the Onyx specimens produced with 0.1 is denser than 0.2 mm layer height. Therefore, higher density means a lower amount of air voids in the sample, hence better mechanical performances.

Additionally, to obtain the void percentage inside the specimen, the Archimedes density test was applied to the Onyx filament itself. The diameter of the filament is 1.75 mm and cut around 50 mm in length. Three tests were done and the results are 1.251 g/cm^3, 1.177 g/cm^3 and 1.178 g/cm^3. The average of these three test results is highly coordinated with the density value of Onyx in the manufacturer's datasheet which is 1.2 g/cm^3.

Table 4.2. PA6 (PA6) D10L10 0.1 mm layer height and 0.2 mm layer height density measurements

PA6	**W_{coupon}**	**$W_{submerged}$**	**Density of Destilled Water**	**Volume of Coupon**	**Density of coupon**	**Void Volume Content (%)**
D10L10 - 0.1 LH-T1	0.760	0.028	0.998	0.734	1.035	5.866
D10L10 - 0.1 LH-T2	0.766	0.027	0.998	0.741	1.034	5.982
D10L10 - 0.1 LH-T3	0.759	0.025	0.998	0.735	1.032	6.153
D10L10 - 0.2 LH-T1	0.757	0.032	0.998	0.727	1.041	5.320
D10L10 - 0.2 LH-T2	0.754	0.036	0.998	0.719	1.048	4.747
D10L10 - 0.2 LH-T3	0.744	0.034	0.998	0.711	1.046	4.923

Table 4.3. Onyx D10L10 0.1 mm layer height and 0.2 mm layer height density measurements

ONYX	W_{coupon}	$W_{submerged}$	Density of Destilled Water	Volume of Coupon	Density of coupon	Void Volume Content (%)
D10L10 - 0.1 LH-T1	0.814	0.067	0.998	0.748	1.088	9.357
D10L10 - 0.1 LH-T2	0.846	0.086	0.998	0.761	1.111	7.387
D10L10 - 0.1 LH-T3	0.839	0.082	0.998	0.758	1.106	7.805
D10L10 - 0.2 LH-T1	0.792	0.041	0.998	0.753	1.052	12.338
D10L10 - 0.2 LH-T2	0.787	0.024	0.998	0.765	1.030	14.195
D10L10 - 0.2 LH-T3	0.777	0.022	0.998	0.757	1.027	14.455

4.3.3. The Effect of Different Build Directions on Compressive Behavior

The true stress-strain curves of the specimens with 0°, 30°, 45°, 60° and 90° build angles at 0.001, 0.01, 0.1 and 1500 1/s are shown in Figures 4.17(a-d), respectively. The flow stress and stress-strain behavior show a strong dependence on the building direction. The highest flow stress is seen in the 0° direction and as the angle increases the flow stress tends to decrease except for 90° specimens. The lowest stress is found in 60° specimens. The 90° specimens however show comparable flow stress with 30° specimens. Furthermore, the stress of 0°, 30°, 45° and 60° specimens continuously increase with increasing strain, 90° specimens show an upper yield point and a plateau region after the upper yield point. The elastic modulus of 90° specimens is also higher than those of 0°, 30°, 45° and 60° specimens. The variations of the elastic modulus and yield strength with build direction are shown in Figure 4.18 (a) and (b) at the quasi-static strain rates. As stated earlier, 90° specimens show the highest modulus and yield strength, followed by 0° specimens, and the lowest modulus and yield strength are seen in 30° and 60° specimens. The results agree with the study of Boghozian et. al. The pictures of the quasi-statically and dynamically tested specimens are shown in Figure 4.19 and Figure 4.20(a-e), respectively. Although quasi-statically tested samples were compressed until about

large strains, the SHPB tested samples show shear type failure as depicted in Figure 4.20(a-e). Opposite to the quasi-static test, 60° and 45° specimens fail by forming shear banding at an earlier strain.

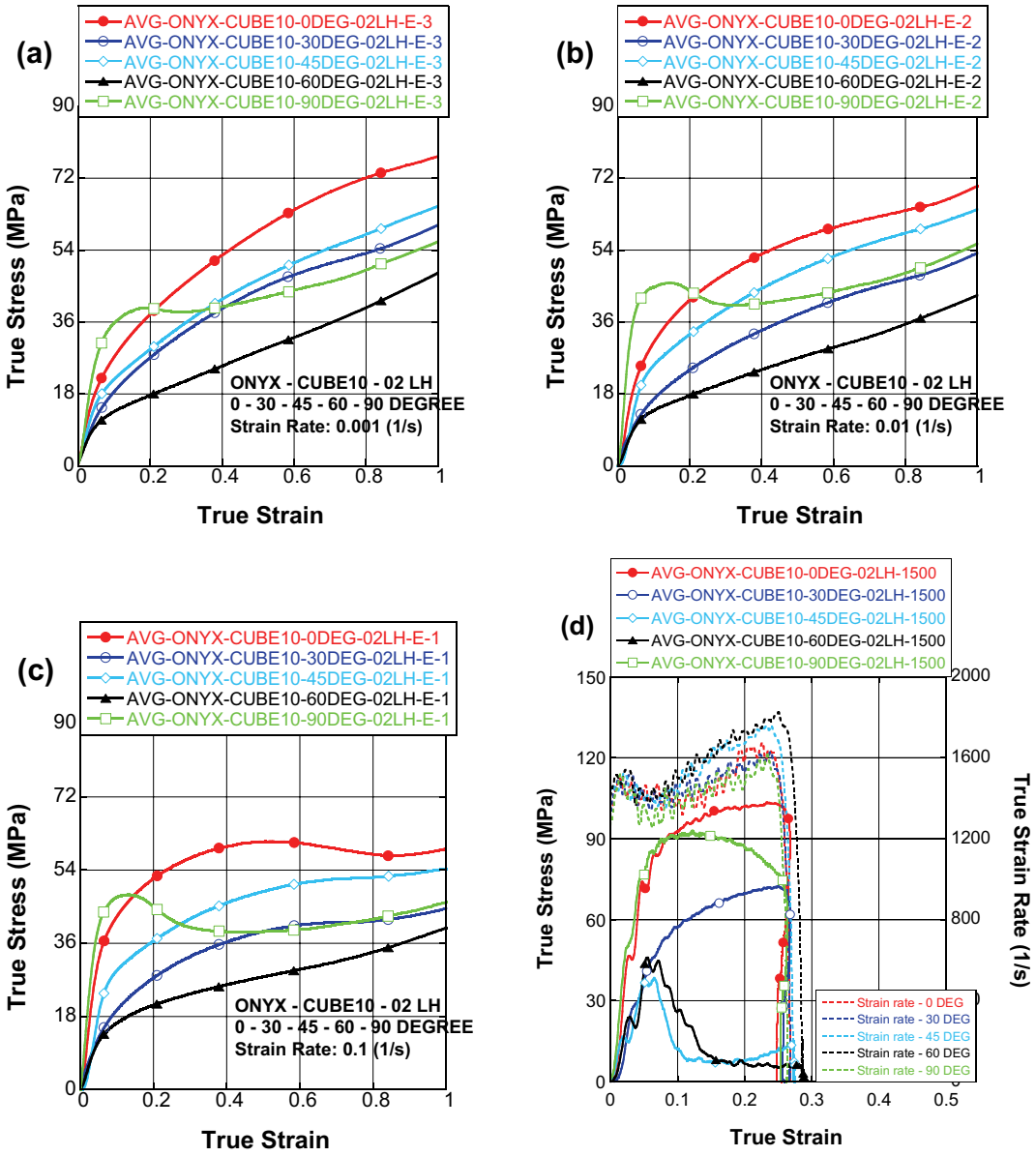

Figure 4.17. The stress and strain curves of Onyx CUBE10 produced with 0.2 mm layer height with at (a) 0.001 1/s, (b) 0.01 1/s, (c) 0.1 1/s and (d) 1500 1/s strain rates

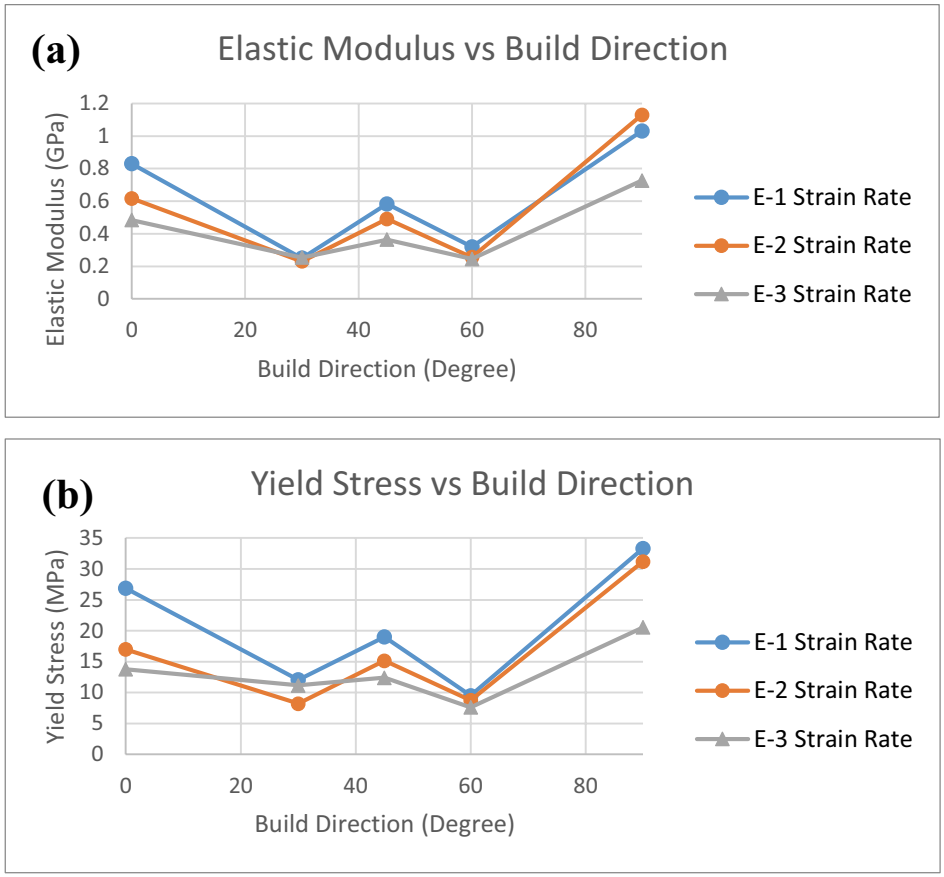

Figure 4.18. The summary of (a) Elastic modulus vs build direction at different strain rates, (b) Yield stress vs build direction at different strain rates.

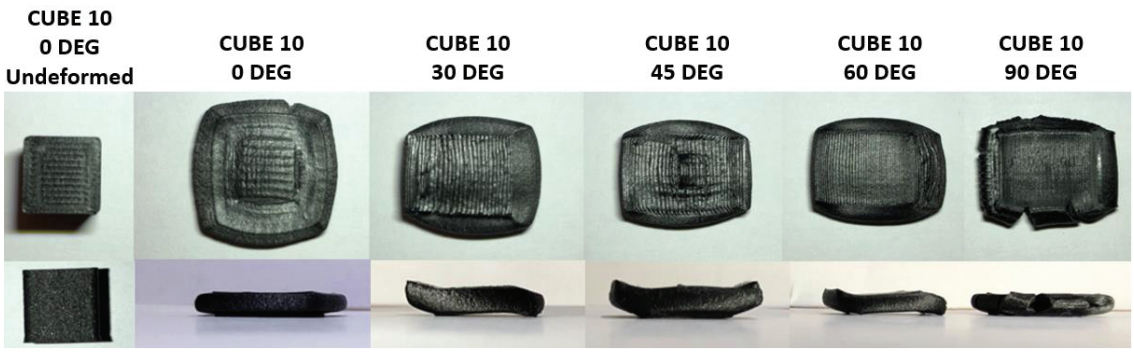

Figure 4.19. Quasi-static compression test images of Onyx 10 mm cubic samples produced with different build directions.

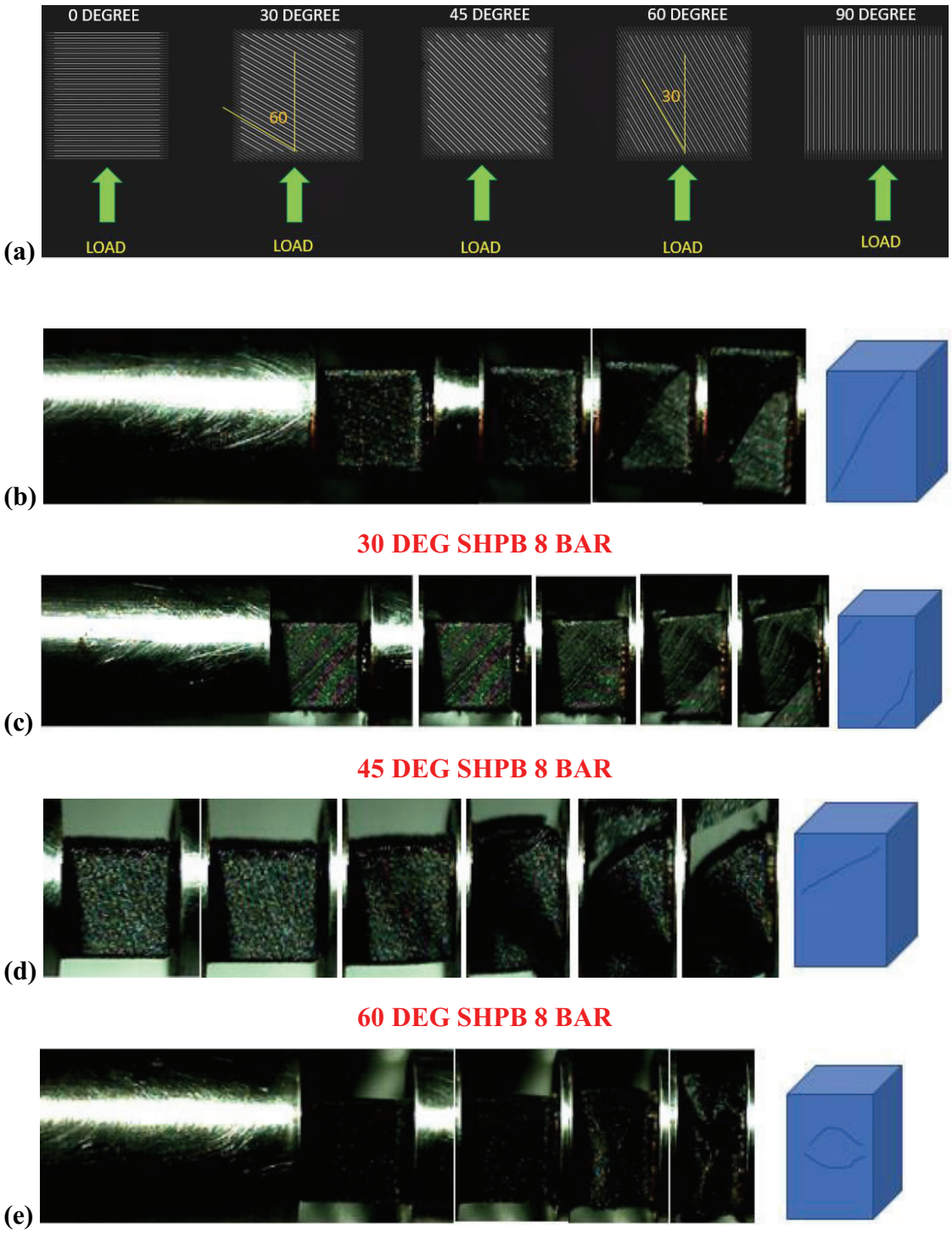

Figure 4.20. The pictures of cubic SHPB test (a) the building directions and angles between acting load, (b) 30° build direction, (c) 45° build direction, (d) 60° build direction and (e) 90° build direction

4.3.4. The Comparison of Infill Patterns on Compressive Behavior

The compression stress-strain curves of cross raster and concentric infill specimens are shown in Figure 4.21 (a-d) at 0.00, 0.01, 0.1 and 1500 1/s, respectively. Cross raster infill specimens exhibit lower elastic modulus values and flow stresses than concentric infill specimens at all strain rates. This may be because the interlocking rings in concentric raster prevent the rasters from moving outward under the effect of compression load. The slipping of individual layers in concentric lay-up is harder than cross raster lay-up [0/90]. With compression loading materials tended to expand laterally while their length shortens. In the layers of concentric rings, the outer rings prevent the lateral expansion of inner rings, therefore it is more durable than cross raster [0/90] lay up. The infill pattern comparison is investigated by Akhoundi et. al. with different infill percentages at the tensile and bending type of loading (Akhoundi and Behravesh 2019) and also continuous fiber reinforcement with concentric and isotropic infill styles compared by Araya-Calvo et.al. applying compression and bending tests (Araya-Calvo et al. 2018b). It was observed that the concentric infill pattern exhibited better mechanical properties than the rectilinear (cross raster) and isotropic infill patterns same as obtained results of this study.

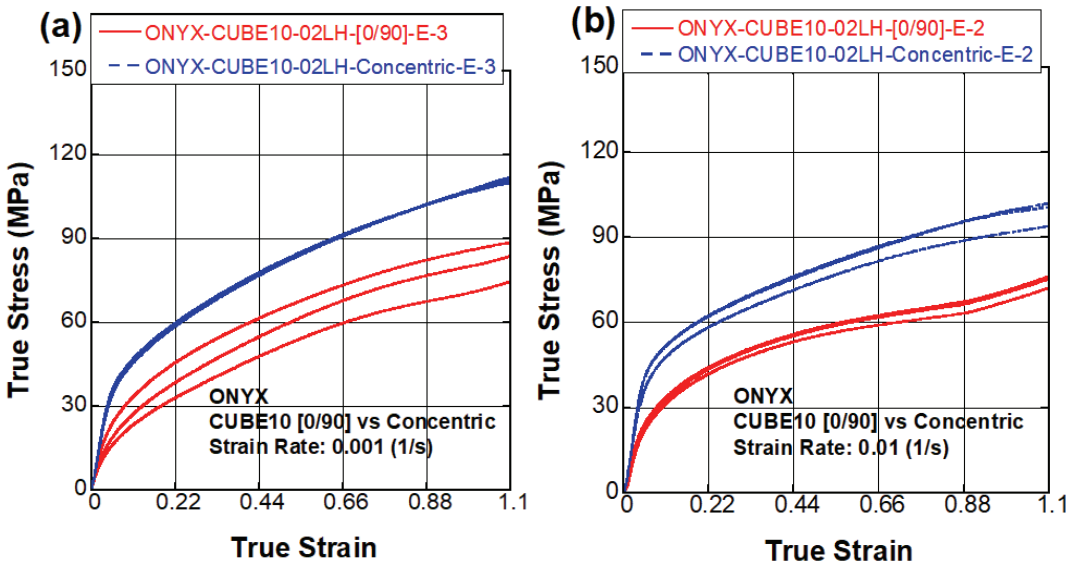

(cont. on next page)

Figure 4.21. The stress and strain curves of Onyx CUBE10 produced with 0.2 mm layer height cross raster angle of [0/90] and Concentric infills at (a) 0.001 1/s, (b) 0.01 1/s, (c) 0.1 1/s and (d) 1500 1/s strain rates

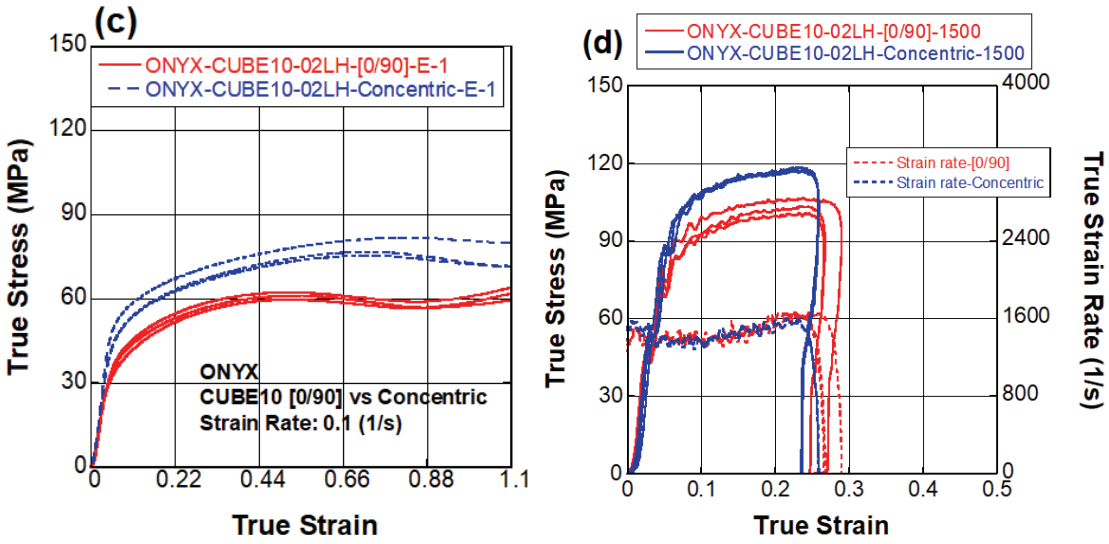

Figure 4.21. (cont.)

4.4. The Strain Rate Sensitivity

Most of the polymers are sensitive to strain rate. It is well known that when the strain rate increases the flow stresses of polymers and their composites increase (Jacob et al. 2004). The rate sensitivities of cylindrical and cubic samples are fitted with the following relation in Equation 4.1

$$\sigma = A\dot{\varepsilon}^m \tag{4.1}$$

where m is the strain rate sensitivity. The rate sensitivity is calculated from the compression tests at 0.001, 0.01, 0.1 1/s quasi-static strain rates and SHPB tests. The 0.1 strain flow stress-ln strain rate curves of 10 mm-diameter, 13 mm-long 0.1 mm layer height PA6 and Onyx specimens are shown in Figure 4.22. The rate sensitivities of PA6 and Onyx specimens are sequentially 0.082 and 0.073. Both PA6 and Onyx show similar rate sensitivities. The strain rate sensitivities of the specimens produced with 0.1 and 0.2 mm layer heights are shown in Figure 4.23. The layer height has almost no effect on the rate sensitivity of PA6, 0.084 and 0.081. But rate sensitivity of 0.2 mm layer height Onyx is higher than 0.1 mm height Onyx and PA6 specimens. Figure 4.24 (a) and (b) show the strain rate sensitivities of cylindrical and cubic specimens. The rate sensitivity of 7, 10 and 13 mm-long 10 mm-diameter (D10L7, D10L10, D10L13) cylindrical specimens

which are produced with 0.1 mm layer height are sequentially 0.085, 0.067 and 0.072 as seen in Figure 4.24 (a). The rate sensitivity of 5, 7 and 10 mm (CUBE5, CUBE7, CUBE10) cubic specimens which are produced with 0.2 mm layer height are sequentially 0.09, 0.072 and 0.088 as shown in Figure 4.24 (b). Additionally, the strain rate sensitivities of Onyx cylinder (D10L10-0.2 LH) and cube (CUBE10-0.2LH) specimens can be compared by looking at Figure 4.23 and Figure 4.24 (b). The strain rate sensitivity of the cylinder (0.1) is higher than the strain rate sensitivity of the cubic specimen (0.088). So it can be concluded the specimen shape effect on strain rate sensitivity is low. The strain rate sensitivities of specimens produced with different build directions were also investigated and the results are presented in Figure 4.25. Because the specimens produced with 45^{o} and 60^{o} build directions fail before 0.1 strain, the strain rate sensitivities were calculated with flow stress at 0.05 strain. According to the figure, 60^{o} specimens have the highest rate sensitivity and the strain rate sensitivities of specimens from the most sensitive build direction to the lowest are 0.116 for 60^{o}, 0.095 for 30^{o}, 0.093 for 0^{o}, 0.067 for 90^{o} and 0.04 for 45^{o}. The lowest rate sensitivity is found for 45^{o} specimens. The effect of the infill pattern on the strain rate sensitivity of additively manufactured composite is presented in Figure 4.26. The strain rate sensitivity of specimens produced with a concentric infill pattern is 0.066 and specimens produced with a [0/90] infill pattern is 0.087. Concentric infill pattern has a lower sensitivity to strain rate sensitivity than [0/90] samples.

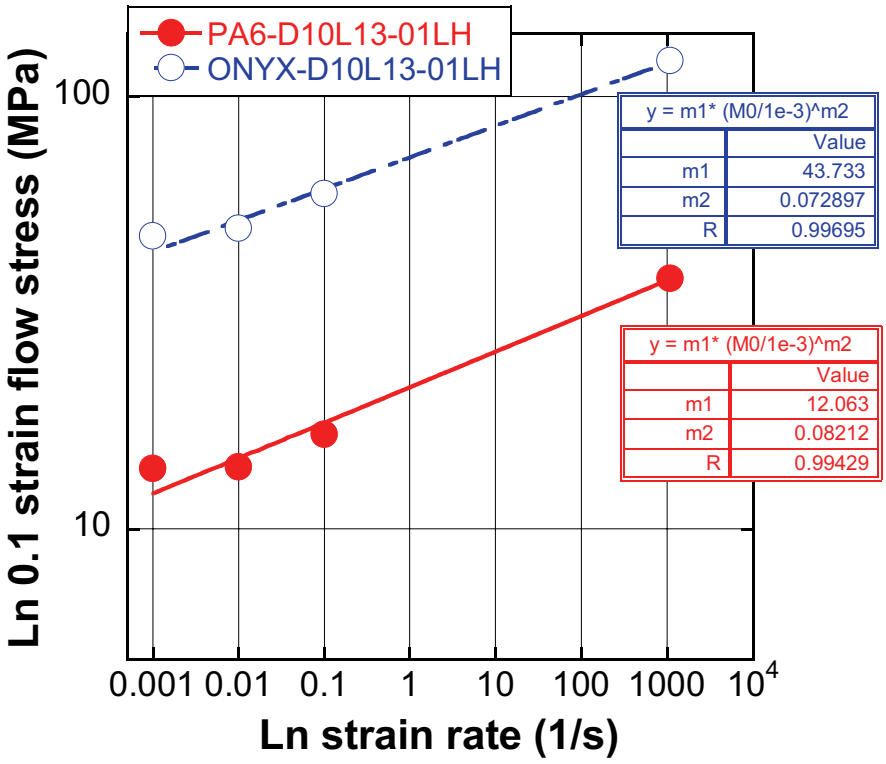

Figure 4.22. Strain rate sensitivities of PA6 and Onyx D10L13-0.1 LH

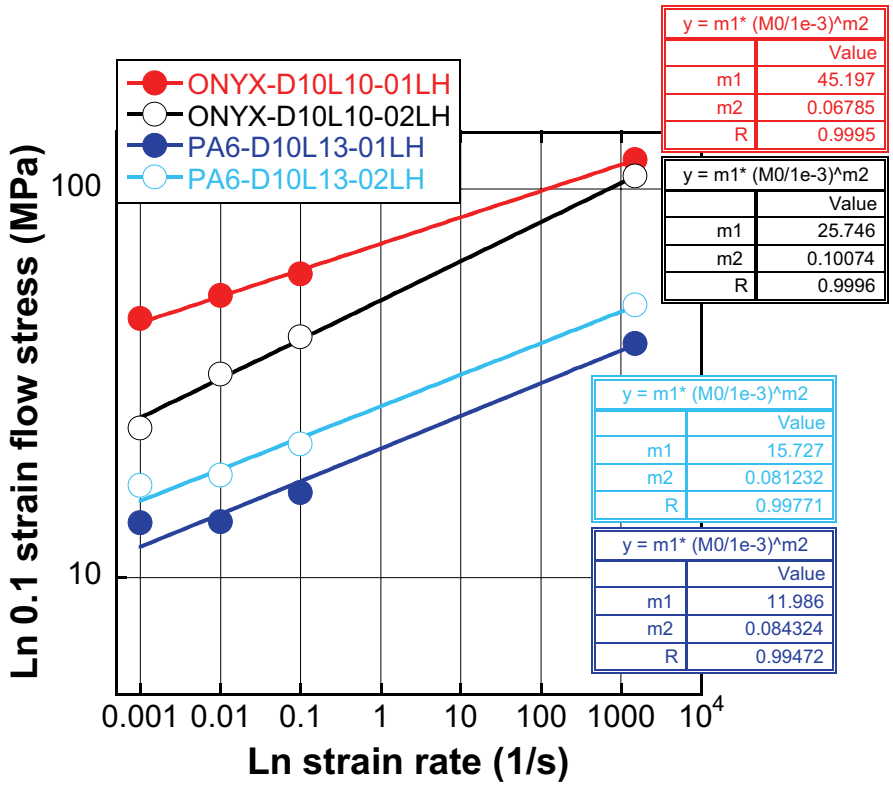

Figure 4.23. Strain rate sensitivities of Onyx D10L10 and PA6 D10L13 produced with 0.1 mm and 0.2 mm layer heights

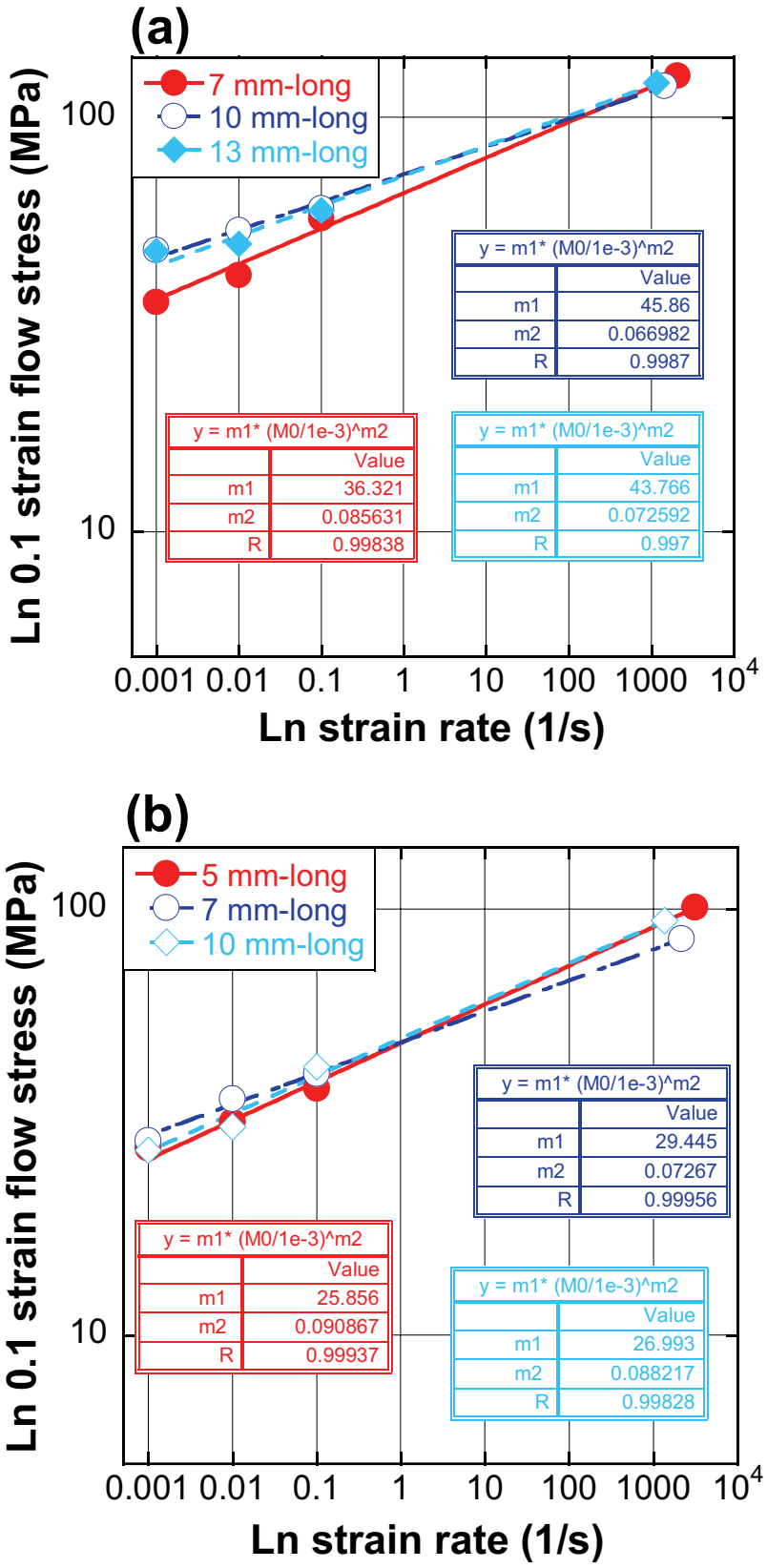

Figure 4.24. Strain rate sensitivities of (a) cylindrical and (b) cubic specimens

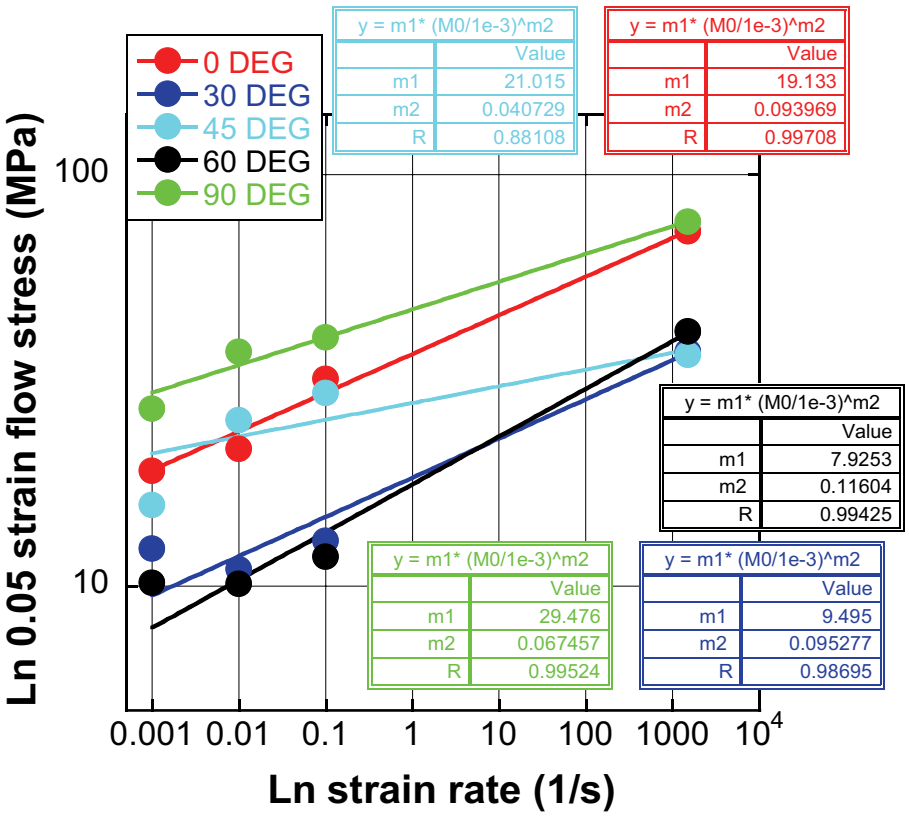

Figure 4.25. Strain rate sensitivities of 10 mm cubic Onyx specimens produced with 0°, 30°, 45°, 60° and 90° build directions

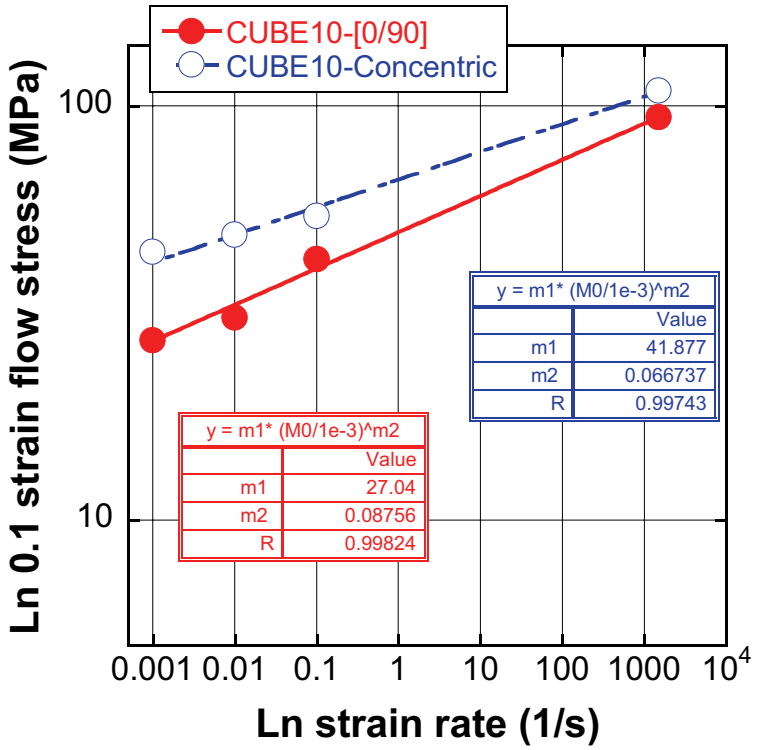

Figure 4.26. Strain rate sensitivities of Onyx CUBE10 samples of [0/90] and Concentric infill patterns

CHAPTER 5

CONCLUSIONS

In this study, the compression behavior of PA6 and short carbon fiber reinforced PA6 (Onyx) produced by the FDM method were investigated experimentally at quasi-static and high strain rates. High strain rate tests were conducted in SHPB test equipment. Additionally, quasi-static strain rate jump tests were carried out by increasing the strain rate at different strain values in the same test by using a single sample in a universal testing machine. The results showed that the addition of short carbon fibers to the PA6 matrix increased the compression strength by 3-4 times. The pyrolysis test results showed that composites contain approximately 13% by weight of short carbon fibers. The microscopic observations showed that the majority of the short carbon fibers were oriented in the printing direction and homogeneously distributed in each yarn.

The compression test results showed that cylindrical specimens had slightly higher flow stress than the cubic specimens. The compression tests on the cylindrical specimens produced in the same diameter but different lengths the cubic specimens with different lengths showed almost no difference regarding stress-strain behavior. PA6 specimens with a layer thickness of 0.2 mm showed higher flow stresses than the specimens with a layer thickness of 0.1 mm, and Onyx specimens showed a vice versa behavior. The density measurements showed a correlation between the compression strength and porosity level. Low compression strength specimens had higher porosities and high compression strength specimens had lower porosity levels. Furthermore, the specimens produced with 90 degrees showed the highest elastic modulus and yield strength and the specimens produced with 30 and 60 degrees had the lowest modulus and yield strength. Concentric infill specimens exhibited lower elastic modulus values and flow stresses than Cross raster infill specimens at all strain rates. In the layers of concentric rings, the outer rings prevented the lateral expansion of inner rings, leading to higher flow stresses than the cross raster [0/90] lay-up. The flow stress of both PA6 and Onyx specimens increased with increasing strain rate. The rate sensitivities of PA6 and Onyx specimens were shown to be similar to each other.

REFERENCES

3d Matter. n.d. “FDM 3D Printing Materials Compared.” Accessed May 5, 2022. https://www.hubs.com/knowledge-base/fdm-3d-printing-materials-compared/.

Ahn, Sung Hoon, Michael Montero, Dan Odell, Shad Roundy, and Paul K. Wright. 2002. *Anisotropic Material Properties of Fused Deposition Modeling ABS*. *Rapid Prototyping Journal*. Vol. 8. https://doi.org/10.1108/13552540210441166.

Akhoundi, B., and A. H. Behravesh. 2019. “Effect of Filling Pattern on the Tensile and Flexural Mechanical Properties of FDM 3D Printed Products.” *Experimental Mechanics* 59 (6): 883–97. https://doi.org/10.1007/s11340-018-00467-y.

Antony Samy, Anto, Atefeh Golbang, Eileen Harkin-Jones, Edward Archer, and Alistair McIlhagger. 2021. “Prediction of Part Distortion in Fused Deposition Modelling (FDM) of Semi-Crystalline Polymers via COMSOL: Effect of Printing Conditions.” *CIRP Journal of Manufacturing Science and Technology* 33: 443–53. https://doi.org/10.1016/j.cirpj.2021.04.012.

Appelsved, Peter. 2012. “Investigation of Mechanical Properties of Thermoplastics with Implementations of LS-DYNA Material Models.” *Degree Project in Solid Mechanics*, 48.

Araya-Calvo, Miguel, Ignacio López-Gómez, Nicolette Chamberlain-Simon, José Luis León-Salazar, Teodolito Guillén-Girón, Juan Sebastián Corrales-Cordero, and Olga Sánchez-Brenes. 2018a. “Evaluation of Compressive and Flexural Properties of Continuous Fiber Fabrication Additive Manufacturing Technology.” *Additive Manufacturing* 22 (February): 157–64. https://doi.org/10.1016/j.addma.2018.05.007.

Attaran, Mohsen. 2017. “The Rise of 3-D Printing: The Advantages of Additive Manufacturing over Traditional Manufacturing.” *Business Horizons* 60 (5): 677–88. https://doi.org/10.1016/j.bushor.2017.05.011.

Auerbach, Alejandro. n.d. “Thermoplastics for AM: Semi-Crystalline vs Amorphous.” Accessed June 8, 2022. https://www.aniwaa.com/insight/am-materials/am-thermoplastics-semi-crystalline-vs-amorphous/.

Bárnik, František, Milan Vaško, Milan Sága, Marián Handrik, and Alžbeta Sapietová. 2019. "Mechanical Properties of Structures Produced by 3D Printing from Composite Materials." *MATEC Web of Conferences* 254: 01018. https://doi.org/10.1051/matecconf/201925401018.

Bazzi, Ali, and Andreas Angelou. 2018. "Simulation of the Anisotropic Material Properties in Polymers Obtained in Thermal Forming Process," no. May: 59.

Benfriha, Khaled, Mohammad Ahmadifar, Mohammadali Shirinbayan, and Abbas Tcharkhtchi. 2021. "Effect of Process Parameters on Thermal and Mechanical Properties of Polymer-Based Composites Using Fused Filament Fabrication." *Polymer Composites* 42 (11): 6025–37. https://doi.org/10.1002/pc.26282.

Bikas, H., P. Stavropoulos, and G. Chryssolouris. 2016. "Additive Manufacturing Methods and Modeling Approaches: A Critical Review." *International Journal of Advanced Manufacturing Technology* 83 (1–4): 389–405. https://doi.org/10.1007/s00170-015-7576-2.

Blok, Lourens Gerrit, Marco Luigi Longana, and Benjamin King Sutton Woods. 2020. "Fabrication and Characterisation of Aligned Discontinuous Carbon Fibre Reinforced Thermoplastics as Feedstock Material for Fused Filament Fabrication." *Materials* 13 (20): 1–26. https://doi.org/10.3390/ma13204671.

Boghozian, Araz. n.d. "Deposition Direction Dependent Failure Criteria for FDM ABS." *California State Polytechnic University Ronald E. McNAIR Scholar Program*.

Camacho, Daniel Delgado, Patricia Clayton, William O'Brien, Raissa Ferron, Maria Juenger, Salvatore Salamone, and Carolyn Seepersad. 2017. "Applications of Additive Manufacturing in the Construction Industry - A Prospective Review." *ISARC 2017 - Proceedings of the 34th International Symposium on Automation and Robotics in Construction*, no. February 2018: 246–53. https://doi.org/10.22260/isarc2017/0033.

Caminero, M. A., J. M. Chacón, I. García-Moreno, and G. P. Rodríguez. 2018. "Impact Damage Resistance of 3D Printed Continuous Fibre Reinforced Thermoplastic Composites Using Fused Deposition Modelling." *Composites Part B: Engineering* 148 (March): 93–103. https://doi.org/10.1016/j.compositesb.2018.04.054.

DePaul, Gary Andrew, Fithawi Ghebretinsae, and F van DerKlift. 2017. "3D Printed Unidirectional Carbon Fibre Reinforced Polymers for Aerospace Applications." *Material Science and Engineering* Master of (March): 61.

http://search.proquest.com/docview/304445758?accountid=174150.

Dickson, Andrew N., James N. Barry, Kevin A. McDonnell, and Denis P. Dowling. 2017. “Fabrication of Continuous Carbon, Glass and Kevlar Fibre Reinforced Polymer Composites Using Additive Manufacturing.” *Additive Manufacturing* 16: 146–52. https://doi.org/10.1016/j.addma.2017.06.004.

Ding, Qingjun, Xinyu Li, Denghui Zhang, Gai Zhao, and Zhijun Sun. 2020. “Anisotropy of Poly(Lactic Acid)/Carbon Fiber Composites Prepared by Fused Deposition Modeling.” *Journal of Applied Polymer Science* 137 (23): 1–11. https://doi.org/10.1002/app.48786.

Durga Prasada Rao, V., P. Rajiv, and V. Navya Geethika. 2019. “Effect of Fused Deposition Modelling (FDM) Process Parameters on Tensile Strength of Carbon Fibre PLA.” *Materials Today: Proceedings* 18: 2012–18. https://doi.org/10.1016/j.matpr.2019.06.009.

Fico, Daniela, Daniela Rizzo, Raffaele Casciaro, and Carola Esposito Corcione. 2022. “A Review of Polymer-Based Materials for Fused Filament Fabrication (FFF): Focus on Sustainability and Recycled Materials.” *Polymers* 14 (3). https://doi.org/10.3390/polym14030465.

Group, PLM. n.d. “Material Guide to Markforged Onyx.” Accessed August 12, 2021. https://plmgroup.eu/articles/material-guide-markforged-onyx/.

Hill, Nevin, and Mehrdad Haghi. 2014. “Deposition Direction-Dependent Failure Criteria for Fused Deposition Modeling Polycarbonate.” *Rapid Prototyping Journal* 20 (3): 221–27. https://doi.org/10.1108/RPJ-04-2013-0039.

Holmström, Petter Henrik, Odd Sture Hopperstad, and Arild Holm Clausen. 2020. “Anisotropic Tensile Behaviour of Short Glass-Fibre Reinforced Polyamide-6.” *Composites Part C: Open Access* 2 (June). https://doi.org/10.1016/j.jcomc.2020.100019.

Horn, Timothy J., and Ola L.A. Harrysson. 2012. “Overview of Current Additive Manufacturing Technologies and Selected Applications.” *Science Progress* 95 (3): 255–82. https://doi.org/10.3184/003685012X13420984463047.

Jacob, George C., J. Michael Starbuck, John F. Fellers, Srdan Simunovic, and Raymond G. Boeman. 2004. “Strain Rate Effects on the Mechanical Properties of Polymer Composite Materials.” *Journal of Applied Polymer Science* 94 (1): 296–301.

https://doi.org/10.1002/app.20901.

Javaid, Mohd, and Abid Haleem. 2019. “Current Status and Applications of Additive Manufacturing in Dentistry: A Literature-Based Review.” *Journal of Oral Biology and Craniofacial Research* 9 (3): 179–85. https://doi.org/10.1016/j.jobcr.2019.04.004.

Jiang, Delin, and Douglas E. Smith. 2017. “Anisotropic Mechanical Properties of Oriented Carbon Fiber Filled Polymer Composites Produced with Fused Filament Fabrication.” *Additive Manufacturing* 18 (August 2017): 84–94. https://doi.org/10.1016/j.addma.2017.08.006.

Karuppiah, Anandvijay. 2016. “Predicting the Influence of Weave Architecture on the Stress Relaxation Behavior of Woven Composite Using Finite Element Based Micromechanics,” no. December 2016. https://doi.org/10.13140/RG.2.2.17881.16482.

KONICA MINOLTA. n.d. “Markforged Mark Two.” Accessed September 11, 2021. https://www.konicaminolta.com.au/products/3d-printers/composite-printing/mark-two.

Krajangsawasdi, Narongkorn, Lourens G. Blok, Ian Hamerton, Marco L. Longana, Benjamin K.S. Woods, and Dmitry S. Ivanov. 2021. “Fused Deposition Modelling of Fibre Reinforced Polymer Composites: A Parametric Review.” *Journal of Composites Science* 5 (1). https://doi.org/10.3390/jcs5010029.

Kreider, P. B., A. Cardew-Hall, S. Sommacal, A. Chadwick, S. Hümbert, S. Nowotny, D. Nisbet, A. Tricoli, and P. Compston. 2021. “The Effect of a Superhydrophobic Coating on Moisture Absorption and Tensile Strength of 3D-Printed Carbon-Fibre/Polyamide.” *Composites Part A: Applied Science and Manufacturing* 145 (March): 106380. https://doi.org/10.1016/j.compositesa.2021.106380.

Kumar, Narendra, Prashant K. Jain, Puneet Tandon, and Pulak Mohan Pandey. 2018. “The Effect of Process Parameters on Tensile Behavior of 3D Printed Flexible Parts of Ethylene Vinyl Acetate (EVA).” *Journal of Manufacturing Processes* 35 (June 2017): 317–26. https://doi.org/10.1016/j.jmapro.2018.08.013.

Kumar, Rakesh, Manoj Kumar, and Jasgurpreet Singh Chohan. 2021. “Material-Specific Properties and Applications of Additive Manufacturing Techniques: A Comprehensive Review.” *Bulletin of Materials Science* 44 (3). https://doi.org/10.1007/s12034-021-02364-y.

Lang, Armand, Claude Gazo, Frédéric Segonds, Fabrice Mantelet, Camille Jean, Jerôme Guegan, and Stéphanie Buisine. 2019. "A Proposal for a Methodology of Technical Creativity Mixing TRIZ and Additive Manufacturing." *IFIP Advances in Information and Communication Technology* 572 (October): 106–16. https://doi.org/10.1007/978-3-030-32497-1_10.

Lanzotti, Antonio, Marzio Grasso, Gabriele Staiano, and Massimo Martorelli. 2015. "The Impact of Process Parameters on Mechanical Properties of Parts Fabricated in PLA with an Open-Source 3-D Printer." *Rapid Prototyping Journal* 21 (5): 604–17. https://doi.org/10.1108/RPJ-09-2014-0135.

Li, Jiahui, Yvonne Durandet, Xiaodong Huang, Guangyong Sun, and Dong Ruan. 2022. "Additively Manufactured Fiber-Reinforced Composites: A Review of Mechanical Behavior and Opportunities." *Journal of Materials Science & Technology* 119: 219–44. https://doi.org/10.1016/j.jmst.2021.11.063.

Liao, Guangxin, Zhixiang Li, Yuchuan Cheng, Dingding Xu, Dingchun Zhu, Shenglong Jiang, Jianjun Guo, Xinde Chen, Gaojie Xu, and Yuejin Zhu. 2018. "Properties of Oriented Carbon Fiber/Polyamide 12 Composite Parts Fabricated by Fused Deposition Modeling." *Materials and Design* 139: 283–92. https://doi.org/10.1016/j.matdes.2017.11.027.

Love, Lonnie J., Vlastamil Kunc, Orlando Rios, Chad E. Duty, Amelia M. Elliott, Brian K. Post, Rachel J. Smith, and Craig A. Blue. 2014. "The Importance of Carbon Fiber to Polymer Additive Manufacturing." *Journal of Materials Research* 29 (17): 1893–98. https://doi.org/10.1557/jmr.2014.212.

Matias, Elizabeth, and Bharat Rao. 2015. "3D Printing: On Its Historical Evolution and the Implications for Business." *Portland International Conference on Management of Engineering and Technology* 2015-Septe: 551–58. https://doi.org/10.1109/PICMET.2015.7273052.

Monticeli, Francisco M., Roberta M. Neves, Heitor L. Ornaghi, and José Humberto S. Almeida. 2021. "A Systematic Review on High-Performance Fiber-Reinforced 3D Printed Thermoset Composites." *Polymer Composites* 42 (8): 3702–15. https://doi.org/10.1002/pc.26133.

Mortazavian, Seyyedvahid, and Ali Fatemi. 2017. "Tensile Behavior and Modeling of Short Fiber-Reinforced Polymer Composites Including Temperature and Strain Rate Effects." *Journal of Thermoplastic Composite Materials* 30 (10): 1414–37. https://doi.org/10.1177/0892705716632863.

Mulholland, T., S. Goris, J. Boxleitner, T. A. Osswald, and N. Rudolph. 2018. “Fiber Orientation Effects in Fused Filament Fabrication of Air-Cooled Heat Exchangers.” *Jom* 70 (3): 298–302. https://doi.org/10.1007/s11837-017-2733-8.

Nawafleh, Nashat, and Emrah Celik. 2020. “Additive Manufacturing of Short Fiber Reinforced Thermoset Composites with Unprecedented Mechanical Performance.” *Additive Manufacturing* 33 (February): 101109. https://doi.org/10.1016/j.addma.2020.101109.

Nazir, Aamer, Kalayu Mekonen Abate, Ajeet Kumar, and Jeng Ywan Jeng. 2019. “A State-of-the-Art Review on Types, Design, Optimization, and Additive Manufacturing of Cellular Structures.” *International Journal of Advanced Manufacturing Technology* 104 (9–12): 3489–3510. https://doi.org/10.1007/s00170-019-04085-3.

Ngo, Tuan D., Alireza Kashani, Gabriele Imbalzano, Kate T.Q. Nguyen, and David Hui. 2018. “Additive Manufacturing (3D Printing): A Review of Materials, Methods, Applications and Challenges.” *Composites Part B: Engineering* 143 (December 2017): 172–96. https://doi.org/10.1016/j.compositesb.2018.02.012.

Niendorf, Karl, and Bart Raeymaekers. 2021. “Additive Manufacturing of Polymer Matrix Composite Materials with Aligned or Organized Filler Material: A Review.” *Advanced Engineering Materials* 23 (4): 1–18. https://doi.org/10.1002/adem.202001002.

Nik Hanyn, N. H., K. Z.Ku Ahmad, Mohd Reusmaazran Yusof, and A. A. Kamarolzaman. 2017. “Investigation of Microstructure and Mechanical Properties of 3D Printed Nylon.” *AIP Conference Proceedings* 1901. https://doi.org/10.1063/1.5010535.

Nomani, Junior, Daniel Wilson, Mariana Paulino, and Mazher Iqbal Mohammed. 2020. “Effect of Layer Thickness and Cross-Section Geometry on the Tensile and Compression Properties of 3D Printed ABS.” *Materials Today Communications* 22: 100626. https://doi.org/10.1016/j.mtcomm.2019.100626.

Pankow, M., C. Attard, and A. M. Waas. 2009. “Specimen Size and Shape Effect in Split Hopkinson Pressure Bar Testing.” *Journal of Strain Analysis for Engineering Design* 44 (8): 689–98. https://doi.org/10.1243/03093247JSA538.

Pascual-González, C., M. Iragi, A. Fernández, J. P. Fernández-Blázquez, L. Aretxabaleta, and C. S. Lopes. 2020. “An Approach to Analyse the Factors behind the Micromechanical Response of 3D-Printed Composites.” *Composites Part B:*

Engineering 186 (January): 107820. https://doi.org/10.1016/j.compositesb.2020.107820.

Peng, Xingshuang, Miaomiao Zhang, Zhengchuan Guo, Lin Sang, and Wenbin Hou. 2020. "Investigation of Processing Parameters on Tensile Performance for FDM-Printed Carbon Fiber Reinforced Polyamide 6 Composites." *Composites Communications* 22 (July): 100478. https://doi.org/10.1016/j.coco.2020.100478.

Peng, Yong, Yiyun Wu, Kui Wang, Guangjun Gao, and Said Ahzi. 2019. "Synergistic Reinforcement of Polyamide-Based Composites by Combination of Short and Continuous Carbon Fibers via Fused Filament Fabrication." *Composite Structures* 207 (September 2018): 232–39. https://doi.org/10.1016/j.compstruct.2018.09.014.

Pereira, Tanisha, John V. Kennedy, and Johan Potgieter. 2019. "A Comparison of Traditional Manufacturing vs Additive Manufacturing, the Best Method for the Job." *Procedia Manufacturing* 30: 11–18. https://doi.org/10.1016/j.promfg.2019.02.003.

Sauer, Max. 2018. "Evaluation of the Mechanical Properties of 3D Printed Carbon Fiber Composites." *Electronic Theses and Dissertations*. https://openprairie.sdstate.edu/etd/2436.

Shanmugam, Vigneshwaran, Deepak Joel Johnson Rajendran, Karthik Babu, Sundarakannan Rajendran, Arumugaprabu Veerasimman, Uthayakumar Marimuthu, Sunpreet Singh, et al. 2021. "The Mechanical Testing and Performance Analysis of Polymer-Fibre Composites Prepared through the Additive Manufacturing." *Polymer Testing* 93 (September 2020): 106925. https://doi.org/10.1016/j.polymertesting.2020.106925.

Tuomi, Jukka, Kaija Stiina Paloheimo, Juho Vehviläinen, Roy Björkstrand, Mika Salmi, Eero Huotilainen, Risto Kontio, Stephen Rouse, Ian Gibson, and Antti A. Mäkitie. 2014. "A Novel Classification and Online Platform for Planning and Documentation of Medical Applications of Additive Manufacturing." *Surgical Innovation* 21 (6): 553–59. https://doi.org/10.1177/1553350614524838.

Utzeri, Mattia, Emanuele Farotti, Mattia Coccia, Edoardo Mancini, and Marco Sasso. 2021. "High Strain Rate Compression Behaviour of 3D Printed Carbon-PA." *Journal of Materials Research* 36 (10): 2083–93. https://doi.org/10.1557/s43578-021-00248-9.

Vidakis, Nectarios, Markos Petousis, Emmanouil Velidakis, Marco Liebscher, Viktor Mechtcherine, and Lazaros Tzounis. 2020. "On the Strain Rate Sensitivity of

Fused Filament Fabrication (Fff) Processed Pla, Abs, Petg, Pa6, and Pp Thermoplastic Polymers." *Polymers* 12 (12): 1–15. https://doi.org/10.3390/polym12122924.

Wang, Kui, Shixian Li, Yanni Rao, Yiyun Wu, Yong Peng, Song Yao, Honghao Zhang, and Said Ahzi. 2019. "Flexure Behaviors of ABS-Based Composites Containing Carbon and Kevlar Fibers by Material Extrusion 3D Printing." *Polymers* 11 (11): 1–12. https://doi.org/10.3390/polym11111878.

Wu, H., W. P. Fahy, S. Kim, H. Kim, N. Zhao, L. Pilato, A. Kafi, S. Bateman, and J. H. Koo. 2020a. "Recent Developments in Polymers/Polymer Nanocomposites for Additive Manufacturing." *Progress in Materials Science* 111 (January). https://doi.org/10.1016/j.pmatsci.2020.100638.

Yang, Dongmin, Haoqi Zhang, Jiang Wu, and Edward D. McCarthy. 2021. "Fibre Flow and Void Formation in 3D Printing of Short-Fibre Reinforced Thermoplastic Composites: An Experimental Benchmark Exercise." *Additive Manufacturing* 37 (October 2020). https://doi.org/10.1016/j.addma.2020.101686.

Zhang, Xu, Wei Fan, and Tianxi Liu. 2020. "Fused Deposition Modeling 3D Printing of Polyamide-Based Composites and Its Applications." *Composites Communications* 21 (July): 100413. https://doi.org/10.1016/j.coco.2020.100413.

Zhao, Yu, Yuansong Chen, and Yongjun Zhou. 2019. "Novel Mechanical Models of Tensile Strength and Elastic Property of FDM AM PLA Materials: Experimental and Theoretical Analyses." *Materials and Design* 181: 108089. https://doi.org/10.1016/j.matdes.2019.108089.

Ziółkowski, Marcin, and Tomasz Dyl. 2020. "Possible Applications of Additive Manufacturing Technologies in Shipbuilding: A Review." *Machines* 8 (4): 1–34. https://doi.org/10.3390/machines8040084.